PZT THIN FILM GROWTH AND CHEMICAL COMPOSITION CONTROL ON FLAT AND NOVEL THREE-DIMENSIONAL MICROMACHINED STRUCTURES FOR MEMS DEVICES

THÈSE N^{O} 3820 (2007)

PRÉSENTÉE LE 6 JUILLET 2007
À LA FACULTÉ DES SCIENCES ET TECHNIQUES DE L'INGÉNIEUR
Laboratoire de céramique
SECTION DE SCIENCE ET GÉNIE DES MATÉRIAUX

ÉCOLE POLYTECHNIQUE FÉDÉRALE DE LAUSANNE

POUR L'OBTENTION DU GRADE DE DOCTEUR ÈS SCIENCES

PAR

Florian CALAME

ingénieur en science des matériaux diplômé EPF
de nationalité suisse et originaire du Locle (NE)

acceptée sur proposition du jury:

Prof. H. J. Mathieu, président du jury
Prof. N. Setter, Prof. P. Muralt, directeurs de thèse
Prof. J. Cross, rapporteur
Dr N. Ledermann, rapporteur
Prof. Ph. Renaud, rapporteur

ÉCOLE POLYTECHNIQUE
FÉDÉRALE DE LAUSANNE
Lausanne, EPFL
2007

for my wife and son…

ABSTRACT

Piezoelectric micro-electro-mechanical systems (MEMS) are finding an increased interest for applications requiring high frequency operation and high mechanical quality. The aim of this work was to improve piezoelectric MEMS along two main research directions. The first one was devoted to the strongest piezoelectric thin film material so far established, namely to the solid solution system lead zirconate titanate (PZT), whose properties are peaking at the morphotropic phase boundary at 53/47 Zr to Ti ratio. Properties of such films were lagging behind the ones of bulk ceramics. In sol-gel deposited films, one of deteriorating factors was earlier identified in the compositional gradient preventing to hit the 53/47 composition throughout the whole film volume. In this work, this gradient could be lowered by the preparation of a new set of solutions, reducing the Zr concentration fluctuations from ±12 to ±2.5at%. In combination with a new sol-gel $PbTiO_3(100)$ seed layer, and an optimized lead excess and heating scheme, the transverse piezoelectric coefficient $|e_{31,f}|$ could be increased from 12 to 17 C/m^2 in 2µm {100}-textured PZT thin films deposited on plane 100mm wafers. In parallel the dielectric constant increased from 1200 to 1600 with a decreasing loss tangent. It could be shown that the dielectric loss must be entirely due to domain wall motions. The second research direction was devoted to the introduction of new piezoelectric shapes by means of deposition into cavities. A free calotte membrane, consisting of a sputtered PZT thin film and its electrodes, has been successfully developed and fabricated as demonstrator of a novel three-dimensional transducer. Calotte profile holes in silicon were prepared by wet etching and were used as micromould for the PZT membrane. The quasi-static vibration amplitude was measured by means of atomic force microscopy (AFM) yielding a responsivity of 3.5 nm/V, i.e. about 20 to 50 times the d_{31} value. The second device was a piezoelectric PZT coated active AFM cantilever. A PZT layer was sputter deposited on patterned (111) platinum bottom electrodes into deep cavities (>300µm) prepared by anisotropic wet chemical etching. The photolithography was made possible using spray coating techniques and correcting masks for aberration errors. The study of the basic properties of such a structure has shown promising results. The maximum deflection at the end of the beam was measured as 5.3 nm/V in quasi-static operation. The so derived $e_{31,f}$ value in the cavity corresponded well to the value obtained on flat wafers. Micro-structural analysis showed that PZT grains grow always perpendicular to the local surface inclination, showing no effect of directional sputter flux. The texturing scheme worked as well on inclined surfaces, i.e. the Pt(111) planes and the PZT {100} planes always stay parallel to the local surface.

Keywords: piezoelectric, thin films, chemical composition control, PZT, micromachining

RÉSUMÉ

Les systèmes micro-électro-mécaniques (MEMS) trouvent un intérêt grandissant pour des applications opérant à hautes fréquences et demandant de hautes qualités mécaniques. Le but de ce travail a été d'améliorer les MEMS piézoélectriques selon deux directions de recherche principales. La première était consacrée au film mince piézoélectrique le plus performant établi jusqu'à présent, c'est-à-dire sur le système de solution solide de zirconate titanate de plomb (PZT), dont on relève un pic des propriétés aux bornes de la phase morphotropique (MPB) à un rapport Zr/Ti de 53/47. Les propriétés de tels films restaient bien loin de celles des céramiques massives. Dans la déposition sol-gel de ces films, un des facteurs dégradant a été identifié dans le gradient compositionnel ne permettant pas d'atteindre une composition homogène de 53/47 dans le volume du film. Dans ce travail, ce gradient a pu être abaissé par la préparation de nouvelles solutions sol-gel, réduisant la fluctuation de la concentration de zircone de ±12 à ± 2.5% atomique. Par la combinaison d'une nouvelle couche sol-gel de nucléation de $PbTiO_3$(100), un excès de plomb et un chauffage optimisés, le coefficient piézoélectrique $|e_{31,f}|$ est passé de 12 à 17 C/m^2 sur des films PZT orientés selon {100} de 2μm d'épaisseur sur plaquettes de 100mm. En parallèle, la constante diélectrique est passée de 1200 à 1600 avec une diminution des pertes. Il a été démontré que ces pertes diélectriques doivent être entièrement dues aux mouvements des domaines de mur. La deuxième amélioration a été d'introduire de nouvelles structures piézoélectriques par le biais de déposition dans des cavités. Une membrane hémisphérique, à base de PZT pulvérisé et de ces électrodes, a été développée et fabriquée comme démonstrateur de nouveaux dispositifs tridimensionnels. Ce profil hémisphérique, préparé par voie humide dans un substrat de silicium, a été utilisé comme moule pour la membrane de PZT. L'amplitude de vibration quasi-statique a été mesurée à l'aide d'un microscope à force atomique (AFM) donnant une réponse de 3.5 nm/V, environ 20 à 50 la valeur du coefficient d_{31}. Le deuxième dispositif fut un levier quantique actif recouvert de PZT pour AFM. Le PZT pulvérisé a été déposé sur une électrode inférieure de Pt(111) structurée à l'intérieur de cavités profondes (>300μm) préparées par gravure humide. La photolithographie a été rendue possible par la déposition par jet et la correction d'aberration sur les masques. L'étude des propriétés de base d'une telle structure a montré des résultats prometteurs comme la déflection maximale en bout de poutre s'élevant à 5.3 nm/V en mode quasi statique. Les valeurs $e_{31,f}$ calculées dans les cavités correspondent aux valeurs mesurée sur plaquettes planes. Une analyse microstructurale a montré que les grains de PZT croissaient perpendiculairement à la surface inclinée localement, démontrant aucun effet directionnel du flux de pulvérisation. Les plans cristallographiques du PZT{100} et du Pt(111) étaient eux aussi parallèles à la surface locale.

Mots-clés : piézoélectrique, films minces, contrôle de la composition chimique, PZT, micro usinage

ACKNOWLEDGEMENTS

I would have been surely unable to finish my PhD without the great help of the numerous people that contributed to this work at the scientific level but also, and especially, at the human level. I then wish to truly thank all these people very much.

My first thought goes to Prof. Nava Setter, who gave me the opportunity and the privilege to realize my PhD in her laboratory. She provided me with all the means necessary to carry out this research in excellent conditions.

My second thought, and warm gratitude, goes naturally to Prof. Paul Muralt, who was my PhD "direct" advisor from the beginning. It was a real pleasure working with such a personality always enthusiasm and available. I truly thank him for his constant support and for the numerous discussions and suggestions as well as the freedom he gave us for the research directions.

I also wish to thank the members of the jury for their participation, expert guidance, and helpful comments. I particularly want to express my gratitude to Prof. Jeff Cross (Fujitsu Laboratories) who made the long trip form Japan to Switzerland for my PhD oral exam, to Prof. Philippe Renaud (EPFL-IMM-LMIS4) who is the director of the Center of MicroNanoTechnology (CMI) where I spent almost half the duration of my PhD, to Dr Nicolas Ledermann (Hach Ultra Analytics SA) who taught me more or less all the lab work that I know, and to Prof. Hans Jörg Mathieu (EPFL-IMX-LMCH) who accepted the presidency of the jury.

I am very grateful to all the people that participated financially and technically to this work, and shared their precious knowledge, but also their very helpful manpower. This work has been partially funded by the Swiss Office for Education and Science (OFES) in the frame of the European FP6 - STREP project MUSTWIN (Contract n° NMP2-CT-2003-505630), the MEMS-pie cooperative research project which was funded by the 6th framework program of the European Commission (Contract n° COOP-CT-2004-508219) and the Swiss Technology-Oriented Program TOP NANO 21 (Project n° 6015.1) under the auspices of the Commission for Technology and Innovation (CTI).

I particular would like to acknowledge some companies for project I was involved in; SINTEF (Norway) with Henrik Reader, Frode Tyholdt, Wilfred Booij, Eric Poppe, and Niels Peter Østbø, Aixacct System AG (Germany) with Klaus Prume and Stefan Tiedke, and NanoWorld AG (Switzerland) with Manfred Detterbeck, Stefan Lutter and Mathieu Burri. All these guys gave me the opportunity to clearly see what was the real work in industry. This was a real enrichment for my further business carrier.

A big “Thank you” goes, of course, to the CMI staff for their continuous help and precious expertise in the clean room. Many thanks are also due to the EPFL CIME staff for the TEM sample preparation and related analysis. I also acknowledge Mr Giancarlo Corradini (EPFL-IPR-LPM2) for the “critical” work on device bonding.

I give a special thank to Dr Sandrine Gentil for sharing all her experience in chemistry. Thank you for the explanation, the discussions as well as the excellent spirit of work and joy of life.

I wish to thank all the people I had the pleasure to know and to share some nice moments during all these years in the ceramics laboratory: Andy, Eugeny, Scott (my officemates), but also, Sam, Janine, Tomo, Maff, Christine, Alvaro, Marco, Guido, Roman, Jacques, Lino, Vladimir, Igor, Enrico, Dragan, Sacha, Julien, Lisa, Guochu, Yongli, Mathieu and the secretaries Eva and Yuko. Thanks for former lab members Brahim, David, Simon, Roman and Jacek.

I would like to express my hearty thanks to my best friends Serge, Fred and Faouzi for all the precious and indispensable moments we shared inside and outside EPFL. We spent a lot of time all together around tables, eating marvelous gastronomic foods and drinks, having some “philosophical” discussions, and some real relaxed periods. A huge thank to the members of my music band Serge, Phil, Mig and Chris for the relaxation time spent in a small room but playing excellent music in a stress-free artistic atmosphere and also Ol for some exceptional musical compositions made during long phone calls and late nights.

I warmly acknowledge my parents Janine and Jean, stepparents Nga and Thien, my brother Nicolas, step-sisters Trinh and Thuy and husband Alexandre as well as their little so cute son, Ludovic, my 2 years old nephew for their invariable presence and support. It’s so important to keep a well close and near family.

And finally, my warmest gratitude goes, of course, to my wife, Trang, and 3 years old son, Hugo. They were always present for me, day and night, during and after work, coming back home sweet home, in a so cozy place, bathing me with so much love and happiness. Without their support, encouragement and constant help, I could never accomplish this work.

LIST OF ABBREVIATIONS

2D	Two Dimensions
3D	Three Dimensions
AC	Alternative Current
AES	Auger Electron Spectroscopy
AFM	Atomic Force Microscope
BHF	Buffered HF
BICMOS	Bipolar-CMOS
BPSG	Boron Phosphor Silicon Glass
CELT	Confined Etchant Layer Technique
CMOS	Complementary Metal Oxide Semi-conductor
CMP	Chemical Mechanical Polishing
CSD	Chemical Solution Deposition
CV	Current Voltage
CVD	Chemical Vapor Deposition
DC	Direct Current
DRAM	Dynamic Random Access Memories
EDM	Electro-Discharge Machining
EDX	Energy Dispersive X-ray Analysis
EFAB	Electrochemical Fabrication
FeRAM	Ferroelectric Random Access Memory
FOM	Figure Of Merit
HNA	Hydrofluoric Nitric Acetic acids
IC	Integrated Circuit
ICP	Inductively Coupled Plasma
IR	Infra Red
JMA	Johnson-Mehl-Avrami
LCR	Inductance Capacitance Resistance
LIGA	German acronym for X-ray lithography: Lithographie Galvanoformung Abformung
LMO	$LaMnO_3$
LPCVD	Low Pressure Chemical Vapor Deposition
LSCO	$La_{2-x}Sr_xCuO_4$
LTO	Low Temperature Oxide

MEMS	Micro Electro Mechanical System
MOCVD	Metalorganic Chemical Vapor Deposition
MOD	Metalorganic Deposition
MPB	Morphotropic Phase Boundary
PLD	Pulsed Laser Deposition
PMN	$Pb(Mg_{1/3}Nb_{2/3})O_3$
PTO	Lead Titanate $PbTiO_3$
PTFE	polytetrafluoroethylene
PYN	$Pb(Yb_{1/2}Nb_{1/2})O_3$
PVD	Physical Vapor Deposition
PZT	Lead Zirconate Titanate $Pb(Zr_x, Ti_{1-x})O_3$
R&D	Research and Development
RIE	Reactive Ion Etching
RTA	Rapid Thermal Annealing
SFM	Scanning Force Microscope
SEM	Scanning Electron Microscope
STM	Scanning Tunneling Microscope
SOI	Silicon On Insulator
TEM	Transmission Electron Microscope
XRD	X-Ray Diffraction

TABLE OF CONTENTS

1

INTRODUCTION

1.1 MEMS, PZT AND THE THIRD DIMENSION

1.2 PIEZOELECTRICITY

1.3 LEAD ZIRCONATE TITANATE SOLID SOLUTION

1.4 DEPOSITION OF PZT THIN FILMS

1.5 AIMS OF THIS WORK

1.6 OUTLINE

1.7 REFERENCES

1.1 MEMS, PZT AND THE THIRD DIMENSION

Micro-Electro-Mechanical Systems (MEMS) is the integration of mechanical elements, sensors, actuators, and electronics on a common silicon substrate through microfabrication technology. While the electronics are fabricated using integrated circuit (IC) process sequences (e.g., CMOS, Bipolar, or BICMOS processes), the micromechanical components are fabricated using compatible "micromachining" processes that selectively etch away parts of the silicon wafer or add new structural layers to form the mechanical and electromechanical devices.

MEMS promises to revolutionize nearly every product category by bringing together silicon-based microelectronics with micromachining technology, making possible the realization of complete systems-on-chip. MEMS is an enabling technology allowing the development of smart products, increasing the computational ability of microelectronics with the perception and control capabilities of microsensors and microactuators, and expanding the space of possible designs and applications.

Microelectronic integrated circuits can be thought of as the "brains" of a system and MEMS increases this decision-making capability with "eyes" and "arms", to allow microsystems to sense and control the environment. Sensors gather information from the environment through measuring mechanical, thermal, biological, chemical, optical, and magnetic phenomena. The electronics then process the information derived from the sensors and, through some decision making capability, direct the actuators to respond by moving, positioning, regulating, pumping, and filtering, thereby controlling the environment for some desired outcome or purpose. Because MEMS devices are manufactured using batch fabrication techniques similar to those used for integrated circuits, unprecedented levels of functionality, reliability, and sophistication can be placed on a small silicon chip at a relatively low cost.

In mainstream MEMS technology, especially in the early years, the used materials were restricted to the ones present in standard silicon processing. The properties of silicon lend themselves well to MEMS, showing good elastic properties, little or no creep and aging due to the high quality of the monocrystalline starting material. In addition, good and fast silicon etching processes are available to achieve structures on a microscopic scale. Together with standard films of silicon technology, such as SiO_2, Si_3N_4, Al, etc., many devices based on electrostatic interaction, piezoresistive effects and thermal effects were realized. However, for many applications, functional materials would still offer better performance. Among these, piezoelectric materials are of primary interest due to the large elastic energy density per unit volume they can generate, their low electrical impedance and low power requirements.

The micromachining of materials is considered to be a key technology in microsystems or MEMS. So far the surface micromachining technology by lithography has been successfully used for the fabrication of microelectronic devices in batch process. The information of the two-dimensional (2D) patterns in the masks can be transferred onto the workpiece as 2D thin film structures, which meet the requirements of the microelectronic device, in the IC technology and in MEMS fabrication at an early stage very well [1]. However, more requirements should be met in microsystems because of the combined functions of microelectronics with micromechanics and/or micro-optics, etc. For example, thicker structure with high aspect ratio or a truly three-dimensional (3D) structure could be more useful for the performance of microsystem and could provide more flexibility on designing microsystems. Therefore, advanced micromachining technologies should be further developed.

Even though evolution of piezoelectric MEMS started with ZnO thin films [2], lead zirconate titanate (PZT) appears to be more promising today because its piezoelectric coefficients are roughly 10 times larger. Indeed, the interest in piezoelectric MEMS based on PZT thin films has markedly increased these last few years. The main advantages of piezoelectric structures lie in immediate response, large available forces, low noise, wide range of operation and simplicity of the transduction mechanism, which is planar [3]. High frequency ultrasonic transducers attract special interest because of suitable performances for airborne ultrasonic applications. Thick PZT films will allow for larger forces, larger voltage outputs and in many case a higher electromechanical coupling factor or larger signal-to-noise ratio.

1.2 PIEZOELECTRICITY

In 1880, Jacques and Pierre Curie discovered an unusual characteristic of certain crystalline minerals: when subjected to a mechanical force, the crystals became electrically polarized. Tension and compression generated voltages of opposite polarity, and in proportion to the applied force. Subsequently, the converse of this relationship was confirmed: if one of these voltage-generating crystals was exposed to an electric field it lengthened or shortened according to the polarity of the field, and in proportion to the strength of the field. These behaviors were labeled the piezoelectric effect [4] and the inverse piezoelectric effect [5], respectively, from the Greek word *piezein*, meaning to press or squeeze.

Although the magnitudes of piezoelectric voltages, movements, or forces are small, and often require amplification (a typical disc of piezoelectric ceramic will increase or decrease in thickness by only a small fraction of a millimeter, for example) piezoelectric materials have been adapted to an impressive range of applications. The piezoelectric effect is used in sensing applications, such as in force or displacement sensors. The inverse piezoelectric effect is used in actuation applications, such as in motors and devices that precisely control positioning, and in generating sonic and ultrasonic signals.

In the 20th century metal oxide-based piezoelectric ceramics and other man-made materials enabled designers to use the piezoelectric effect and the inverse piezoelectric effect in many new applications. These materials are generally physically strong and chemically inert, and they are relatively inexpensive to manufacture. The composition, shape, and dimensions of a piezoelectric ceramic element can be built to meet the requirements of a specific purpose.

All crystalline piezoelectric materials belong to a point group which lacks a center of symmetry so that an applied stress or an applied electric field gives rise to an asymmetrical ionic displacement (change of the dipole moment) which causes electrical charges or lattice deformation respectively. Every crystal belonging to non-centrosymmetric groups (20 groups of 32) is thus piezoelectric. A notable exception is the cubic 432 point group because other symmetry characteristics combine and prevent it. Piezoelectricity is described mathematically within a material's constitutive equation, which defines how the piezoelectric material's stress (σ), strain (S), charge-density displacement (D), and electric field (E) interact. The direct piezoelectric effect is defined as the linear relation between the mechanical stress σ_l N/m^2 applied on a piezoelectric material and the resulting density charge D_i. On the opposite, the inverse piezoelectric effect expresses the linear relation between the applied electric field E_i and the generated elastic deformation S_k. Both direct and inverse effect may be represented by the following relations:

$$D_i = d_{ik}\sigma_k + \varepsilon_0\varepsilon_{ij}^T E_j \tag{1.1}$$

$$S_k = s_{kl}^E\sigma_l + d_{ik}E_i \tag{1.2}$$

where the matrix indexation is used: kl = 1..6 and ij = 1..3. d_{ik} can be expressed either in C/N or m/V and represents the piezoelectric coefficient. s_{kl}^E m^2/N is the elastic compliance of the matrix and ε_{ij}^T the dielectric permittivity tensor.

The most important properties to investigate in piezoelectric materials are the longitudinal d_{33} and transverse e_{31} piezoelectric coefficients. d_{33} describes the change of the material thickness or strain S_3 which develops along the vertical 3-axis due to the application of an electric field E_3 in the same direction. d_{33} is very useful to describe most of the devices fabricated from bulk piezoelectric ceramics such as medical ultrasonic transducers or piezoelectric thin film resonators and RF filters. However, the coefficient d_{33} is not very often used in piezoelectric MEMS as they are usually based on deflecting structures such as cantilevers or membranes. The relevant piezoelectric constant is thus the transverse coefficients e_{31} or d_{31} that describe the bending of the structure along the 1-axis as a function of a transverse electrical field E_3 or the transverse charges (along 3-axis) generated by the bending of the piezoelectric material.

However, the piezoelectric properties in piezoelectric thin films cannot be directly compared with the ones (d_{33}, e_{31}) of corresponding bulk materials. As the film is clamped on the substrate, it cannot move in the in-plane directions (x, y) but is free to expand in the off-plane direction (z). The piezoelectric properties exhibited in piezoelectric thin films are thus modified by these boundary conditions and new effective coefficients have to be introduced. Those coefficients are the longitudinal $d_{33,f}$ and transverse $e_{31,f}$ where the f subscript denotes effective values of the film.

For a perfect clamping, S_1 and S_2 are equal to zero and S_3 is non-zero. For the same reason, the in-plane stress σ_1 and σ_2 are equal and σ_3 is zero. Starting from the constitutive equations and introducing the particular boundary conditions of perfect clamping, effective values $d_{33,f}$ and $e_{31,f}$ can be calculated [6, 7]:

$$e_{31,f} = \frac{d_{31}}{s_{11}^E + s_{12}^E} = e_{31} - \frac{c_{13}^E}{c_{33}^E} e_{33} \tag{1.3}$$

$$d_{33,f} = d_{33} - \frac{2s_{13}^E}{s_{11}^E + s_{12}^E} d_{31} = d_{33} - 2s_{13}^E e_{31,f} \tag{1.4}$$

$$\varepsilon_{33,f} = \varepsilon_{33}^T - \frac{2d_{31}^2}{\left(s_{11}^E + s_{12}^E\right)\varepsilon_0} = \varepsilon_{33}^T - \frac{2e_{31,f}^2\left(s_{11}^E + s_{12}^E\right)}{\varepsilon_0} \qquad \varepsilon_{33}^T > \varepsilon_{33,f} > \varepsilon_{33}^S \tag{1.5}$$

where c_{ij}^E are the stiffness constants. The effect of the partial clamping is thus to reduce the bulk d_{33} and ε_{33}^T coefficients and to increase the magnitude of the fully clamped e_{31} transverse effect.

1.3 LEAD ZIRCONATE TITANATE SOLID SOLUTION

The ceramic having the better piezoelectric properties at room temperature is a two perovskite mixed alloy: lead titanate $PbTiO_3$ and lead zirconate $PbZrO_3$. These two form a solid solution in all proportions, and give the communally named PZT (Lead Zirconate Titanate). Its crystal structure above the Curie temperature is of course of the perovskite type, which has a cubic unit cell (Figure 1.1).

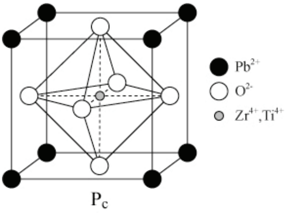

Figure 1.1: Perovskite crystal structure of paraelectric PZT above its Curie temperature.

The structure can be considered as a face-centered cubic derivative structure in which the larger Pb cation and oxygen anion together form a face-centered cubic lattice. The smaller Ti and Zr cations occupy the octahedral sites in the face-centered cubic array and have only oxygen anions as their nearest neighbors.

Figure 1.2: Perovskite crystal structure of rhombohedral (F_R) and tetragonal (F_T) PZT.

When the crystal is cooled down through its Curie temperature, it undergoes a phase transition from the cubic paraelectric (P_C) state to the ferroelectric state. A spontaneous polarization occurs because the oxygen and titanium ions are shifted relatively to the lead ions. The distortion of the lattice is rhombohedral (F_R) for zirconium-rich compositions and tetragonal (F_T) for titanium-rich compositions (Figure 1.2).

In the case of the tetragonal distortion, six equivalent directions for the polarization can occur, whereas eight are possible in the rhombohedral case. At the morphotropic phase boundary (MPB), both phases coexist since they have an equal probability to form. This leads to fourteen different possibilities for the direction of the spontaneous polarization and thus to a peak of the piezoelectric and dielectric properties. At room temperature, the MPB is situated at 53% Zr. This so-called morphotropic phase boundary is not exactly a boundary but rather a phase with monoclinic symmetry. Noheda *et al* [8] reported this new monoclinic phase in 1999, initially establish by Jaffe *et al* [9]. This new phase is intermediate between the tetragonal and rhombohedral PZT phases. Its symmetry relates both phases (Cm being a subgroup of both P4mm and R3m) through the only common symmetry element, the mirror plane. Both, the tetragonal and rhombohedral phases (at least in the proximity of the MPB) have a local structure different from the long-range one and at low temperatures a monoclinic long range order is established by the freezing-out of one of the ”local monoclinic structures” in both the rhombohedral and the tetragonal phases. Under the application of an electric field, one of the locally disordered sites becomes preferred, inducing the monoclinic distortion. This induced monoclinic phase is stable and remains after the field is removed. An orthorhombic antiferroelectric phase (A_0) is formed for very low titanium contents (Figure 1.3).

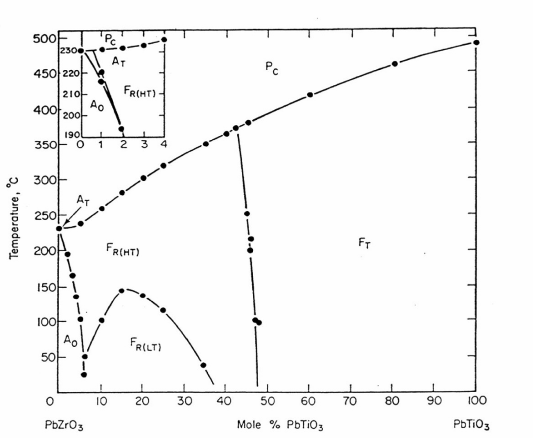

Figure 1.3: Phase diagram of $Pb(Zr_{1-x}Ti_x)O_3$ solid solution [9].

The PZT ceramics have rapidly supplanted all other materials for piezoelectric applications because:

- they have better electromechanical coupling coefficient than barium titanate,
- they have higher Curie temperatures, leading to a wider range of temperature use or a higher processing temperature,
- they can be easily polarized,
- they are easy to produce.

1.4 DEPOSITION OF PZT THIN FILMS

Nowadays, the piezoelectric PZT thin film can be deposited by various methods: Chemical Solution Deposition (CSD) [10], sputtering from ceramic [11] and co-sputtering from metal targets [12] and Chemical Vapor Deposition (CVD) [13] are the major ones. These different deposition methods will be explained more in detail in the state of the art (next chapter).

1.4.1 GEOMETRICAL FEATURES

In the processing of thin films by CSD, the goal is to optimize film properties for specific applications. To effectively meet this goal, a fundamental understanding of substrate, solution chemistry, and thermal processing effects on the *structural evolution* of the as-deposited film to the crystalline ceramic state is required. Through the efforts of a number of research groups worldwide, there has been significant progress in understanding the film processing behavior of materials that has allowed for the preparation of high-quality films.

Chemical solution deposition only works well if the substrate is flat. In case of large three-dimensional (3D) features, the spun on solution is thicker in depressions, thinner on elevations, and unevenly distributed on the walls. The most suited processes are the ones crystallizing the film in-situ, thus CVD, and in-situ sputtering. CVD is certainly superior, because a very good conformality (step coverage) of film thickness is in general obtained. Sputtering works sufficiently well if the features are not too deep and do not exhibit too steep walls. PVD seems to meet the entire requirements for the deposition on a high aspect ratio three-dimensional structure.

1.4.2 QUALITY OF PZT

Talking about quality of PZT is, in most cases, related to its piezoelectric coefficient and, in particular, its transverse piezoelectric coefficient d_{31} or $e_{31,f}$. These coefficients are the relevant values in all microsystems based on deflecting structures such as cantilevers or vibrating membranes. As describe before, the measurement of d_{31} coefficient is subject to important assumptions concerning the elastic properties. The direct measurement of the $e_{31,f}$ coefficient is thus more suitable as it is not necessary to know the elasticity of the film. The determination of this coefficient often relies on the measurement of a transverse deflection of a beam as a function of an applied voltage under quasi-static (off-resonance) conditions.

1.4.3 INTEGRATION OF PZT THIN FILMS

Substrates on which PZT is deposited can vary and are basically inert: silicon wafers, alumina, sapphire, MgO, $SrTiO_3$, etc. Except in cases where preferred orientations are sought or when a dielectric/semiconductor interface should take place, the substrate chosen is principally guided by processing reasons, economical costs or reactive problems linked to temperature. In most cases, silicon wafers are chosen preferably from the others for its remarkable ability of processing. Indeed, Elemental silicon is the principal component of most semiconductor devices. Silicon is widely used in semiconductors because it remains a semiconductor at higher temperatures than the semiconductor germanium and because its native oxide is easily grown in a furnace and forms a better semiconductor/dielectric interface than almost all other material combinations. Some authors [14] deposit a layer (Al_2O_3, MgO, ZrO_2, TiO_2) on the substrate before the PZT film.

For mixed sol-gel/powder systems, very few studies integer ceramic film influence on substrate and electrode nature. However, the electrode deposition is of primary importance: it must keep its electrical properties even after heavy thermal treatment under oxidizing atmosphere applied on the substrate and on the ferroelectric film. In the case of PZT film deposit on silicon and used for memories applications, the most commonly used material is platinum, normally associated with a thin layer of titanium to improve adhesion.

1.5 AIMS OF THIS WORK

The aim of this work is to improve piezoelectric MEMS along two main research directions:

1. Improvement of sol-gel PZT thin films,
2. Introduce new piezoelectric shapes through deposition into cavities.

We will explore the fabrication of optimized PZT sol-gel film on wafers and study in-situ sputter deposition for the fabrication of three-dimensional structures, investigate structuration techniques for obtaining new shapes on the micron scale and assess properties for ultrasonic transduction. This work will imply the study of sol-gel deposition from seed layer to full thin film characterization, growth modes on oblique surfaces, the study of patterning processes yielding large heights in the third dimension and the study of suitable shapes for transducer applications.

The thesis will cover the following topics:

- The deposition and growth of optimized, high quality lead titanate seed layer and PZT sol-gel film on whole 4 inch wafers,
- The deposition and growth mode on oblique surfaces using sputter deposition process of PZT,
- The fabrication of three-dimensional structures based on in-situ PZT sputter deposition to advance the piezoelectric MEMS field in thin film processing and microstructuration.

1.6 OUTLINE

Apart from this first introducing chapter dedicated to history, theoretical background, definitions of piezoelectricity, PZT and deposition issues, the thesis has been structured as follow:

Chapter 2 covers the state of the art. The different deposition methods of PZT, the relevant properties, the fabrication methods for three-dimensional structures and the way of patterning into deep cavities are discussed.

Chapter 3 presents the results of the study of sol-gel lead titanate seed layers and optimized highly {100}-textured sol-gel PZT thin films. Structural and compositional analyses, piezoelectric and dielectric properties of the films are the major issues.

Chapter 4 illustrates the fabrication of a free standing PZT membrane and its electrodes in a three-dimensional calotte shape. Structuration issues till the end of the device and growth properties of sputtered PZT on oblique surfaces are exposed as well as basic characterizations.

Chapter 5 explains the feasibility study of a PZT coated active AFM cantilevers. Achievable photolithography and structuration into deep cavities (>300 µm) are explained. Dielectric and piezoelectric responses of the cantilevers are presented.

Chapter 6 is the conclusion and discusses potential opportunities for the future.

1.7 REFERENCES

1. K.A. Jackson, *Processing of semiconductors*, in R.W. Cahn, Editor, Materials Science and Technology: A Comprehensive Treatment 16, VCH, Weinheim (1996)
2. P.L. Chen, R.S. Muller, R.D. Jolly, G.L. Halac, R.M. White, A.P. Andrews, T.C. Lim and M.E. Motamedi, *Integrated silicon microbeam PI-FET Accelerometer*, IEEE Transactions on Electron Devices, **29**(1), 27-33 (1982)
3. P. Muralt, *Piezoelectric thin films: from smart materials to smart applications*, in ISIF, Aachen (2000)
4. J. Curie and P. Curie, *Développement, par pression, de l'électricité polaire dans les cristaux hémièdres à faces inclinées*, C. R. Acad. Sc., Paris, **91**, 294-295 (1880)
5. J. Curie and P. Curie, *Contraction et dilatation produite sur les cristaux hémièdres à faces inclinées*, C. R. Acad. Sc., Paris, **93**, 1137 (1881)
6. K. Lefki and J.M. Dormans, *Measurement of piezoelectric coefficient of ferroelectric thin films*, J. Appl. Phys., **76** (3), 1764-1767 (1994)
7. P. Muralt, *Piezoelectric thin films for MEMS*, Integ. Ferro., **17**, 297-307 (1997)
8. B. Noheda, D.E. Cox, G. Shirane, J.A. Gonzalo, S.E. Park and L.E. Cross, *A monoclinic ferroelectric phase in the* $Pb(Zr_{1-x}Ti_x)O_3$ *solid solution*, Appl. Phys. Lett., **74**, 2059 (1999)
9. B. Jaffe, W.R. Cook and H. Jaffe, *Piezoelectric ceramics*, Academic Press Limited, New York (1971)
10. N. Ledermann, P. Muralt, J. Baborowski, S. Gentil, K. Mukati, M. Cantoni, A. Seifert and N. Setter, *{100}-textured, piezoelectric* $Pb(Zr_x, Ti_{1-x})O_3$ *thin films for MEMS: integration, deposition and properties*, Sensors and Actuators, **A 105**, 162-170 (2003)
11. I. Kanno, S. Fujii, T. Kamada, and R. Takayama, *Piezoelectric properties of c-axis oriented Pb(Zr,Ti)O[sub 3] thin films*, Appl. Phys. Lett., **70**, 1378 (1997)

12. S. Hiboux, P. Muralt, and T. Maeder, *Domain and lattice contributions of dielectric and piezoelectric properties of thin films as a function of composition*, J. Mat. Res., **14**, 4307-4318 (1999)

13. M. Okada, S. Takai, M. Amemiya and K. Tominaga, *Preparation of c-axis oriented $PbTiO_3$ thin film by MOCVD under reduced pressure*, Jpn. J. Appl. Phys., **28**, 1030-1034 (1989)

14. G. Yi, Z. Wu and M. Sayer, *Preparation of $Pb(Zr,Ti)O_3$ thin films by sol-gel processing ; electrical, optical and elecrooptic properties*, J. Appl. Phys, **64**, 2717 (1988)

2

STATE OF THE ART

2.1 DEPOSITION AND SELECTED PROPERTIES OF PZT THIN FILMS

Today it is possible to integrate ferroelectric thin films on silicon microelectronics devices. The major driving force for this achievement was the non-volatile ferroelectric memory. Successful integration work also leads to an interest in PZT MEMS. Potential applications using the piezoelectric effect include: micro-actuators for nano-robotics [1], atomic force microscopy [2], motion sensors [3], ultrasound transducers sensors [4], micropumps [5], microphones [6] or active damping [7]. The pyroelectric effect is applied in infrared detectors useful for imaging, security and gas sensors [8, 9, 10].

2.1.1 OVERVIEW

In the early stages, PZT films were deposited by physical vapor deposition (PVD) methods, such as flash and electrode beam evaporation [11, 12], ion-beam deposition [13, 14] and radio-frequency magnetron sputtering [15]. More recently, metalorganic chemical vapor deposition (MOCVD) has attracted great interest due to its large deposition rates, ease for conformal coating and well-controlled film stoichiometry capabilities [16, 17]. Pulsed laser ablation techniques [18, 19] were used to evaluate material properties. One major drawback in vacuum based deposition procedures lies in the fact that they require large capital investments. Chemical solution deposition (CSD) methods seem to meet the requirement for an easy implementation of the deposition process with standard silicon wafer technology when the coating is performed on flat surfaces. Major advantages of the CSD method are easy control of material composition in multicomponent systems, the ability to produce uniform large area coatings and cost efficiencies.

Crucial issue in the PZT deposition is the substrate quality. In most cases, planar capacitor geometry must be used, implying growth of PZT on a bottom electrode. For MEMS application, this one is usually a platinum (111) thin film, which provides for a sufficient chemical and thermal stability in combination with a good electrical conduction. Of course, many investigations were made using perovskite conductors such as LSCO [20] or LMO [21]. In this work, we will concentrate, however, on the use of Pt electrode.

2.1.2 PHYSICAL VAPOR DEPOSITION OF PZT

Nowadays, different kinds of thin films in IC and micromachining are deposited by physical vapor deposition (PVD). PVD reactors may use a solid, liquid, or vapor raw material in a variety of source configurations. The first attempts for depositing PZT thin films by PVD method have come in the end of the 70's.

Ion beam deposition was used broadly in R&D, the data storage industry, and the optical components industry. This deposition method used an energetic, broad beam ion source carefully focused on a grounded metallic or dielectric sputtering target. Material sputtered from the target deposits on a nearby substrate to create a film [22]. This technique was manly exploited as research tool and is no more used.

Extensive work has been performed on magnetron sputter-deposition of ferroelectric thin films, and especially PZT. Several variations of this technique have been developed. Single multicomponent oxide (ceramic) [23, 24], multi element metal [25, 26] and multiple metallic targets [27, 28, 29] were used to synthesis PZT.

The approach that consists to use sintered PZT targets or a pressed mixture of TiO_2, ZrO_2 and PbO [30] has some drawbacks. First, stoichiometry variations at the target surface occur after repeated use, i.e. after different depositions, and the question of reproducibility in the composition of the final thin film is addressed. Then, the insulating nature of the oxide target limits the input power that may be applied on metallic targets, and thus reduces significantly the deposition rate. Finally, in the case of an "in-situ" deposition (described below) at elevated temperatures, excess lead must be added to the target in order to compensate the PbO loss. This implies to know what is the right excess lead content in the target for a given deposition temperature.

On the other hand, there are great advantages to use reactive sputtering from metallic targets in pure O_2 or Ar/O_2 gas mixture atmosphere. The principle is that the reactive gas reacts with the metallic targets during sputtering and forms the corresponding oxides, i.e. PbO, ZrO_2 and TiO_2 in the case of Pb, Zr and Ti targets used for the PZT deposition. This deposition technique allows high deposition rates due to higher input power, and the composition can be maintained constant throughout target lifetime by adjusting power levels. In this approach, there also two major configuration. The first one is to use three different metals (Pb, Zr, Ti) mounted on one backing plate. The target is composed of several sectors of the metals and is called multicomponent metal target. This process was used by Sreenivas et al [25, 31] for producing PZT thin films at various compositions. The other approach is to use several elemental metallic targets (called multiple targets method). In the multi target geometry, the substrate holding plate is continuously rotated underneath the targets during the deposition, achieving a layer-by-layer growth of the film. Contrary to the multicomponent metal target which is a static process, the thickness of the layer is strongly dependent on the rotation speed. The major disadvantage of this technique is a reduced deposition rate due to the dynamic deposition, but it allows a perfect control of the Zr/Ti ratio. Hence, all composition of the PZT phase diagram can be studied with the same three metallic targets of Pb, Zr and Ti just by adjusting the corresponding powers. Moreover, there is no more problem of PbO loss during an in-situ process since excess lead can be applied by increasing the power at the Pb target. Bruchhaus *et al* were the first to employ this technique in order to fabricate IR detectors [32].

2.1.3 METALORGANIC CHEMICAL VAPOR DEPOSITION (MOCVD)

Whereas before 1990 mostly physical deposition techniques were applied, the chemical methods are now becoming more and more important. Metalorganic chemical vapor deposition (MOCVD) is one of the most appealing film synthesis methods, because of its excellent film uniformity, compositional control, high deposition rates, large wafer-size scaling and also high degree of film thickness conformality. This in-situ deposition method is very well suited for microelectronic high-density ferroelectric random access memory (FeRAM) [33, 34] or dynamic random access memories (DRAMs) [35], where 3D capacitors can be well covered and thus exploiting the entire surface capabilities. It was shown that nucleation of the PZT perovskite phase started when the deposition temperature exceeded 550°C [36] and that to obtain single-phase PZT thin films, the optimal temperature should be contained between 600°C and 650°C [37]. However, more recent works from Funakubo *et al* [38] have shown property improvement of PZT films deposited as low as 400°C. Unfortunately, not much is known on piezoelectric properties of such films

2.1.4 CHEMICAL SOLUTION DEPOSITION (CSD)

Today, the chemical solution deposition (CSD) of PZT thin films seems to meet the integration requirements of the standard silicon wafer technology encountered in MEMS fabrication.

2.1.4.1 MOD

A chemical thin-film process has been reported [39, 40, 41, 42] based on the decomposition of metallo-organic compounds (MOD process). In this process, metal carboxylates such as Pb-2-ethylhexanoate or Pb-neodecanoate are codissolved with alkoxides, acetylacetonates, or carboxylates of titanium and zirconium, e.g., titanium-, zirconium isopropylate, titanium-, zirconium butylate, zirconium acetylacetonate, or titanium-di-methoxy-di-neodecanoate in organic solvents such as isopropanol, butanol, or xylene. These precursors are less sensitive to humidity than sol-gel precursors and are suitable for the deposition of thin oxide films deposited by spin coating on appropriate substrates. Decomposition of the spin-coated films at 500°C to 800°C results in the crystallization of the perovskite structure.

2.1.4.2 Sol-gel

The sol-gel process [43, 44] can be broadly defined as the chemical elaboration of ceramic materials by synthesis of precursor solution, gelation of the sol, drying and organics pyrolysis followed by a crystallization at high temperature. This sol-gel technique involves alkoxides where the macromolecular oxide network is obtained first through hydrolysis of the alkoxy groups and when the hydroxy groups are formed, polycondensation reactions take place.

The first reports of sol-gel deposition of $PbTiO_3$ and $Pb(Zr,Ti)O_3$ thin films were due to Gurkovich *et al* (1984) [45] and Budd *et al* (1985) [46] respectively. For PZT films, Budd used lead trhydrate, titanium isopropoxide, zirconium n-propoxide and 2-methoxyethanol as solvant. Driven by the potential applications of PZT thin films in devices, subsequent reports on the optimization of the solution precursors have been published, mainly by Schwartz *et al* at Sandia National Laboratories, USA [47, 48, 49, 50].

Sol-gel deposition is based on multiple spin coating of the wafer with a liquid precursor. After decomposing the residual organics through a pyrolysis at about 350°C, the film is crystallized during a final rapid thermal annealing (RTA) under oxygen atmosphere, usually at a temperature of 650°C.

2.1.4.3 CSD method over others

The advantages of CSD method over vacuum deposition processes lie in a better control of the material composition in multicomponent systems, the ability to produce uniform large area coating and the relative low level of investments required for the equipments.

The major inconvenient of this spin-coating deposition method lies in a need of an absolute planar substrate without any prior microstructuration. In the confection of three-dimensional structures this will be impossible, as the three-dimensional (3D) structures are usually prefabricated. Vacuum deposition processes are preferred.

2.1.5 GROWTH ISSUES

A crucial issue in PZT deposition is crystallization. The deposition temperature should be as low as possible to facilitate device fabrication. PZT thin films can nucleate and grow at much lower temperature (i.e. around 600°C) than bulk ceramics obtained by sintering powders. The necessary diffusion distances are much smaller and provide for a homogeneous and stoichiometric mixture on the molecular level. With most of the techniques described above, there are two routes to process the PZT films.

The first one is “in-situ” deposition (one step process). This latter is performed on a heated substrate and the crystallization process occurs directly during the film growth. The “in-situ” processing clearly helps for the crystallization at lower temperature. It has been shown for example by Li *et al* [51] that perovskite traces could be observed from 200°C for in-situ magnetron sputter-deposited $PbTiO_3$, and that good pyroelectric coefficients were obtained for $PbTiO_3$ grown at 450°C by in-situ multi targets sputtering [27]. Plasma effect may explain the lower crystallization temperature for sputter-deposited thin films [29, 52]. From the point of view of in-situ crystallization at relatively low temperatures, PLD (pulsed laser deposition) techniques are very attractive, since crystallization temperatures similar to the ones of sputter deposition methods have been reported [53, 54].

The other one is called “ex-situ” deposition (two steps process). The film, deposited below 300°C, is mostly amorphous and needs to be crystallized by an additional heat treatment in a furnace. This is this method we will more focus on with the use of the CSD sol-gel deposition technique.

2.1.5.1 Crystallization of sol-gel PZT

The preparation of high quality PZT films using the sol-gel technique requires a controlled conversion of the as-deposited structure to a PZT crystalline phase. The formation of the perovskite phase can be achieved by annealing the film at 500-700°C. Typically, the crystallization path can be separated into three stages [41, 55, 56, 57]. Upon heating, the amorphous phase transforms into oxygen deficient pyrochlore/fluorite structure, $Pb_2(Zr,Ti)_2O_{7-x}$, for a temperature range of ~350°C to ~600°C. Above ~470°C the perovskite phase starts crystallizing. For temperature exceeding 700°C and long exposures, a new lead deficient phase $Pb(Zr,Ti)_3O_7$ forms at the surface of the film due to volatilization of PbO. However, the crystallization path depends on many parameters [41, 55, 57, 58]. The starting amorphous film homogeneity can be influenced by the type of the solution chemistry, lead excess introduced in the PZT precursors, and the pyrolysis conditions (i.e. oxygen content). The conversion of this amorphous phase into perovskite structure strongly depends on the thermal treatments, annealing atmosphere, substrate-electrode structure, the solution chemistry, the lead excess in the precursor [59] and the pyrolysis conditions [60, 61].

2.1.5.2 Nucleation on Pt (111)

The growth of PZT thin films is nucleation controlled as observed in early work on sol-gel deposition [56]. It means that heterogeneous nucleation takes place more easily than homogeneous nucleation. This is very important for chemical solution deposition (CSD) process as it allows obtaining a columnar film microstructure nucleated at the bottom electrode. Several issues were proposed to control the film texture.

One of the first methods used to control the film texture was to influence the nucleation kinetics by means of the heating rates as demonstrated by Aoki *et al* [62] in 1994. He introduced an intermediate heating treatment at 480°C and 650°C to obtain {100} and {111} film texture respectively. In both cases, the films were then crystallized at 650°C during 10 minutes in air.

But nucleation controlled growth allows also to choose the texture of the film by using suitable combination of seeding layer and electrode. In 1998, the controlled growth of {111}-textures PZT thin films has been demonstrated by Muralt *et al* using few nm thick titania (TiO_2) seed layer on platinized electrode [63]. It was shown that this very thin titania affinity layer reduces the effective activation energy for nucleation, even though it exhibits another crystalline phase than PZT. The role of titania consists essentially in pinning PbO to avoid excess desorption before nucleation. In 1999, Hiboux *et al* reported that {100}-textured thin sputtered films can be obtained using 10 nm sputtered deposited {100}-oriented perovskite $PbTiO_3$ (PTO) seeding layer [52, 64, 65]. The deposition of this seed layer reduces lead loss during nucleation and inhibits the nucleation of pyrochlore second phase. Further more, it was shown to be effective in reducing the crystallization temperature of the pure perovskite, explained by the reaction of ample nucleation sites. On RF magnetron sputtered PZT films, Cattan *et al* reported in 1996 a dramatic change of the texture as the thickness of $PbTiO_3$ seed layer was changing from 2 to 40 nm [66]. On sol-gel PZT film, Ledermann *et al* reported in 2003 a {100}-texture obtained with 5 nm PTO (beginning of the junction between the PTO islands) and with 7.5-15 nm (swinching of the cell) [67]. Above 20 nm, it gives {111}-textured PZT films.

2.1.5.3 Phase transformation during post-annealing processes of perovskite PZT thin films

Not many studies have been carried out concerning the phase transformation of PZT thin films from amorphous to crystallization phase [68, 69, 70, 71, 72]. To this day no real theory of phase transformation has been developed. One can establish the activation energy values for the phase transformation using the Arrhenius plots based on the Johnson-Mehl-Avrami (JMA) kinetic analyses [73, 74, 75, 76]. This theory is based on solid state phase transformation and concentrate on the calculation of the crystallized volume as a function of time

2.1.6 PIEZOELECTRIC COEFFICIENT $e_{31,f}$

In MEMS based piezoelectric thin films, two major parameters govern the performances of the device: the piezoelectric film thickness and the transverse piezoelectric coefficient $e_{31,f}$. In most cases, the $e_{31,f}$ coefficient assures the electromechanical coupling of a deflective mechanical structure containing the PZT thin film capacitor. Improvements of such structures thus require an optimal $e_{31,f}$, and frequently a PZT film thickness of several micrometers. The $e_{31,f}$ coefficient describes the in-plane film stresses developed under an electric field at the condition that the film is free to change its thickness. One requirement for optimized films can be readily formulated. The e_{ij}-coefficients are obtained from the d_{ij}-coefficients by multiplication with the stiffness tensor ($e_{ij} = d_{ik}c_{kj}$). As a consequence, only dense films can provide optimal e_{ij}-coefficients.

As known from bulk ceramics, the properties of the $Pb(Zr_x,Ti_{1-x})O_3$ solid solution vary substantially with the compositional parameter x. The region near the morphotropic phase boundary (MPB) is of special interest. This boundary separates the tetragonal symmetry of the Ti-rich compositions from the rhombohedral symmetry of the Zr-rich compositions. The large number of possible polarization directions at this boundary leads to a peaking of permittivity and piezoelectric coefficients [77]. It has been shown that this peaking of properties is also present in sputtered [64] and in sol-gel [67] PZT but less pronounced.

In 1996, Luginbuhl *et al* measured a transverse piezoelectric coefficient $e_{31,f}$ of -3.3 C/m^2 on sol-gel PZT {111}-textured deposited on microbeams [78]. Dubois *et al* reported in 1999 [79] the effective transverse piezoelectric coefficient $e_{31,f}$ for sol-gel PZT {111}-textured films. The maximum was found for PZT 45/55 with $e_{31,f} = -8.3$ C/m^2. This value was comparable to those obtained by Shepard *et al* [80] using the wafer flexure method [81] as $e_{31,f}$ up to -8.2 C/m^2 for sputtered {111}-textured PZT 50/50. More recently, Ledermann *et al* reported in 2003 [67] the effective transverse piezoelectric coefficient $e_{31,f}$ for sol-gel PZT {100}-textured films showing superior properties, i.e. a larger $e_{31,f}$ at a smaller dielectric constant than the {111}-texture. The maximum was found for PZT 53/47 with $e_{31,f}$ = -12.1 C/m^2.

In the last 2 years, $e_{31,f}$ values of -1.7 C/m^2 for sputtered porous films [82] and -6.2 C/m^2 for sol-gel films were published [83]. Higher values were reported for other $PbTiO_3$ based film materials, so for epitaxial $Pb(Mg_{1/3}Nb_{2/3})/PbTiO_3$ a value of -11 C/m^2 [84, 85], and for $Pb(Yb_{1/2}Nb_{1/2})/PbTiO_3$ deposited on platinized silicon a value of -13 C/m^2 [86].

For comparison, $e_{31,f}$ derived from classical PZT ceramics data (Berlincourt) amounts -9.6 C/m^2 [77] and the calculated $e_{31,f}$ of optimized bulk ceramics of doped PZT (Motorola 3203 HD) amounts to -25 C/m^2 [87]. All these $e_{31,f}$ value are shown in Table 2.1.

Table 2.1: Effective transverse piezoelectric coefficient $e_{31,f}$ of various lead titanate based materials, and in particular PZT, prepared by different methods and different groups.

Material	**Deposition**	**-$e_{31,f}$ [C/m^2]**	**Temp. Pyro./Cryst.**	**Year**	**Reference**
PZT {111}	Sol-gel	3.3	350°C / 600°C	1996	78
PZT {111} 45/55	Sol-gel	8.3	400°C / 650°C	1999	79
PZT {111} 50/50	Sputtered	8.2	In-situ 600°C	1999	80
PZT {100} 53/47	Sol-gel	12.1	350°C / 650°C	2003	67
PZT	Sputtered	1.7	Ex-situ 675°C	2006	82
PZT 52/48	Sol-gel	6.2	350-500°C / 700°C	2006	83
PMN/PT	MOCVD	11	650°C	2006	84, 85
PYN/PT	Sol-gel	13	200°C / 750°C	2005	86
PZT 52/48	Bulk ceramic	9.6		1960	77
PZT 3203 HD	Bulk ceramic	25		1997	87

2.2 FABRICATION AND PATTERNING OF THREE DIMENSIONAL STRUCTURES

2.2.1 THREE DIMENSIONAL STRUCTURE FABRICATION

The seamless integration of conventional microelectronics with three-dimensional, microdynamic mechanical components is one of the prominent goals of MEMS technology. Conventional microelectronics integrated circuit (IC) processing is predominantly a two-dimensional fabrication technique. On the other hand, many MEMS microsensor and actuator applications require three-dimensional components. Since MEMS technology is an extension of IC processing, the primary challenge is to realize mechanical components with physically large and high-resolution features in all three dimensions.

LIGA (German acronym for X-ray lithography (X-ray Lithographie), Electroplating (Galvanoformung), and Molding (Abformung)) is a combined technique of lithography and electrochemistry which has become a powerful tool for making integrated micromechanical devices with high aspect ratios, even though they are limited to pseudo three dimensional (3D) microstructures with shapes similar to the extrusions from the two dimensional (2D) mask. All the cross-sections of different depths of these structures perpendicular to the light beam are similar to the 2D mask [88, 89, 90]. Since the amount of information contained in a 2D pattern in the mask is much smaller than that contained in truly 3D mould (e.g. geomorphologic map), new techniques for quick replication (transference of the information) of truly 3D micromould to the workpiece is highly desirable for batch production of microsystems. Examples of micromechanical devices are miniaturized springs, screws, and universal joints, motors and engines, turbines, gearboxes, chain drives, clutches, propellers and solenoids. Other examples of micro-electrical or optical devices are on-chip microwave transmission lines and high-Q inductors, switches or lens array for optical communications.

EFAB (Electrochemical Fabrication) technique was proposed by Cohen *et al* in 1999 [91]. A truly 3D mould (e.g. geomorphologic map) was resolved into contour map (a series of contour lines) automatically with the help of a computer and the workpiece was automatically fabricated layer by layer according to contour lines one by one. The process for production of many 2D masks and the alignment for each mask are thus simplified. However, a great number of steps should be taken if a truly 3D structure is desired.

CELT (an abbreviation for Confined Etchant Layer Technique) as a new approach of electrochemical 3D micromachining was proposed by Tian *et al* in 1992 [92]. The active etchant is electrochemically generated at the surface of a stable mould with 3D micro-pattern, and is rapidly consumed during its diffusion away from the surface into the solution. Therefore, the etchant is confined within an extra thin diffusion layer around the surface. As a result, a 3D pattern of the mould can be replicated on the etched substrate on approaching to the mould.

Very recently another important approach of electrochemical 3D micromachining was reported by Schuster *et al* [93]. The principle of this method is based on the time constant for local double layer charging, which varies linearly with the local distance between a tool electrode and a conductive workpiece in an electrochemical environment. On applying ultrashort voltage pulses with several tens of nanoseconds, significant charging of the double layer of workpiece only occurs at electrode separations in the nano- to micrometer range. Because the rates of electrochemical reactions are exponentially dependent on the potential drop in the double layer, the anodic dissolution is strongly confined to these polarized electrode regions in very close proximity. Reynarts *et al* [94] used the same so-called non-conventional machining technique for the development of real three-dimensional microstructures; electro-discharge machining (EDM) [95, 96].

All this presented techniques use micromould to develop three-dimensional structures. An other method is the use of sacrificial layer. Chomnawang *et al* [97] have fabricated 3D micro-inductors by means of sacrificial polymer. A high aspect ratio cubic structure is done on a silicon substrate by photoresist followed by hard curing, ending up with a cross-sectional bell-shape core with graded profile. Another possibility is to use Cu or Ni electroless [98] or electrodeposited bumps grown on a structured conductive layer. The deposition quality (hardness, surface state, internal stress…) depends on a lot of parameters such as bath chemical composition, pH, temperature, current density, agitation. The electrodeposition technique can be used directly to fabricate three-dimensional structures such as chromium micro tip developed by Lennon *et al* [99].

2.2.2 PHOTOLITHOGRAPHY ON THREE-DIMENSIONAL SHAPES

Since the development of microelectromechanical systems (MEMS) and the increasing use of three-dimensional (3D) microstructures, new techniques and processes are required to fulfill the demand for nonuniform photoresist layer over non-planar surfaces with high topography as the photolithographic step for three-dimensional structures fabrication is of primary importance. The process of spin coating, the conventional technique for photoresist coating on flat wafers, was optimized for coating on nonplanar surfaces too [100, 101]. However, it does not perform well for 3D MEMS devices with high topography. Electrodeposition of photoresist has been reported as an attractive method for 3D stacks of chips and interconnects [102, 103], but it requires a conductive layer. Recently, a new coating method, direct spray coating of photoresist [104], has been introduced as a resist coating technique specifically for MEMS. Although this technique is still in the early stages of exploration, it appears to be a promising technique for coating irregular surfaces as it presents some advantages over spin coating and electrodeposition of photoresist.

2.3 REFERENCES

1. P. Muralt, M. Kohli, T. Maeder, A. Kholkin, K. Brooks, N. Setter and R. Luthier, *Fabrication and characterization of PZT thin-film vibrators for micromotors*, Sensors and Actuators, **A 48**, 157-165 (1995)

2. Y. Miyahara, T. Fujii, S. Watanabe, A. Tonoli, S. Carabelli, H. Yamada and H. Bleuler, *PZT cantilever for non-contact atomic force microscopy*, Appl. Surf. Sci., **140**, 428-431 (1999)

3. J.J. Bernstein, S.L. Finberg, K. Houston, L.C. Niles, H.D. Chen, L.E. Cross, K.K. Li, K. Udayakumar, *Micromachined high frequency ferroelectric sonar transducers*, IEEE Trans., UFFC, **44**, 960-969 (1997)

4. J. Baborowski, N. Ledermann, P. Muralt and D. Schmitt, *Simulation and characterization of piezoelectric micromachined ultrasonic transducers (PMUT's) based on PZT/SOI membranes*, Integr Ferroelectr., **54**, 557-564 (2003)

5. P. Lugienbuhl, S.D. Collins, G.-A. Racine, M.-A. Grétillat, N.F.D. Rooij, K.G. Brooks and N. Setter, *Microfabricated Lamb wave device based on PZT sol-gel thin film for mechanical treansport of solid particules and liquids*, J. Micromech. Syst., **6**, 337-346 (1997)

6. N. Ledermann, P. Muralt, J. Baborowski, N. Forster and J.P. Pellaux, *Piezoelectric* $Pb(Zr_x,Ti_{1-x})O_3$ *thin film cantilever and bridge acoustic sensors for miniaturized photoacoustic gas detectors*, J. Micromech. Microing., **14**(12), 1650-1658 (2004)

7. L. Edery-Azulay and H. Abramovich, *Active damping of piezo-composite beams*, Compos. Struc., **74**(4), 458-466 (2006)

8. B. Willing, M. Kohli, P. Muralt, N. Setter and O. Oehler, *Gas spectrometry based on pyroelectric thin film arrays integrated on silicon,* Sensors and Actuators, **A 66**, 109-113 (1998)

9. H.R. Beratan, C.M. Hanson, J.F. Belcher and K.R. Udayakumar, *Thin film pyroelectric imaging array*, in International Symposium on Integrated Ferroelectrics, ISIF (Monterey, CA) (1998)

10. R. Bruchhaus, D. Pitzer, R. Primig, W. Wersing and Y. Xu, 5th Infrared Sensors and Systems, vol 4 (Dresden: Dresden University Press), 79-84 (1997)

11. L.S. Phillips and B.S Ma, *Ferroelectric films by flash evaporation of PZT,* Electronic Components, **12**, 523-526 (1971)

12. M. Oikawa and K. Toda, *Preparation of PZT thin films by an electron beam evaporation technique*, Appl. Phys. Lett., **28**(8), 491-492 (1976)

13. R.N. Castellano and L.G. Feinstein, *Ion-beam deposition of thin films of ferroelectric PZT*, J. Appl. Phys., **50**(6), 4406-4411 (1979)

14. S.B. Krupanidhi, *Low energy ion bombardment induced effects in multi-component electroceramic thin film*, in Science and technology of electroceramic thin films, edited by O. Auciello and R. Waser (Kluwer, Dordrecht, The Netherlands), **284**, 23-51 (1995)

15. M. Ischida, S. Tsuji, K. Kimura, H. Matsunami and T. Tanaka, *Epitaxial growth of ferroelectric PLZT thin films*, J. Crystal Growth, **45**, 393-398 (1978)

16. Y. Sakashita, T. Onon, H. Segawa, K. Tominaga and M. Okada, *Preparation and electrical properties of MOCVD-deposited PZT thin films*, J. Appl. Phys., **69**(12), 8352-8357 (1991)

17. M.D. Keijser, P.J. Van Veldhoven and G.J.M. Dormans, *Organomettalic chemical vapor deposition of lead zirconate titanate*, in Science and technology of electroceramic thin films, edited by O. Auciello and R. Waser (Kluwer, Dordrecht, The Netherlands), **284**, 75-84 (1995)

18. R. Dat, O. Auciello and A.I. Kingon, *Effects on the temperature on the ferroelectric properties of PZT based capacitors prepared by pulsed laser-ablation*, Integrated Ferroelectrics, **9**, 333-338 (1995)

19. R. Ramesh, O. Auciello, V.G. Keramidas and R. Dat, *Pulsed laser ablation-deposition and characterizatin of ferroelectric metal oxide heterostructures*, in Science and technology of electroceramic thin films, edited by O. Auciello and R. Waser (Kluwer, Dordrecht, The Netherlands), **284**, 1-22 (1995)

20. F. Wang and S. Leppävuori, *Properties of epitaxial ferroelectric* $PbZr_{0.56}Ti_{0.44}O_3$ *heterostructures with* $La_{0.5}Sr_{0.5}CoO_3$ *metallic oxide electrodes*, J. Appl. Phys., **82**(3), 1293-1298 (1997)

21. J.S. Choi, J.S. Kim, .I.R. Hwang, S.H. Hong, S.H. Kim, I.S. Byun, J.H. Lee, S.H. Jeaon, B.H. Park, T. Choi, S. Shin and J. Lee, *Epitaxially grown* $PbZr_{0.3}Ti_{0.7}O_3$ *thin films on* $LaMnO_3$ *applicable to nano-storage media*, Integr. Ferroelec., **75**, 139-146 (2005)

22. R.N. Castellano, M.R. Notis and G.W. Simmons, *Composition and stress state of thin-films deposited by ion-beam sputtering*, Vacuum, **27**(3), 109-117 (1977)

23. K. Abe, H. Tomita, H. Toyoda, M. Imai and Y. Yokote, *PZT thin film preparation on Pt-Ti electrode by RF sputtering*, Jpn. J. Appl. Phys., **30**(9B), 2152-2154 (1991)

24. K. Suu, A. Osawa, Y. Nishioka and N. Tani, *Stability control of composition of RF-sputtered* $Pb(Zr,Ti)O_3$ *ferroelectric thin film*, Jpn. J. Appl. Phys., **36**(Part 1, No. 9B), 5789-5792 (1997)

25. K. Sreenivas and M. Sayer, *Characterization of PZT thin films deposited from multi-element metal targets*, J. Appl. Phys., **64**(3), 1484-1493 (1988)

26. A. Fujisawa, M. Furihata, I. Minemura, Y. Onuma and T. Fukami, *Effect of Zr/Ti ratio on crystal structure of thin lead zirconate-titanate films prepared by reactive sputtering*, Jpn. J. Appl. Phys., **32**(Part 1, No. 9B), 4048-4051 (1993)

27. R. Bruchhaus, H. Huber, D. Pitzer and W. Wersing, *Deposition of ferroelectric PZT thin films by planar multi-target sputtering*, Ferroelectrics, **127**, 137-142 (1992)

28. K.Y. Kim, S.T. Kim and W.K. Choo, *Structural and electrical properties of PZT thin films prepared by multitarget reactive DC magnetron cosputtering*, Jpn. J. Appl. Phys., **32**, 1700-1707 (1993)

29. T. Maeder and P. Muralt, *In-situ thin film growth of* $PbTiO_3$ *by multi target sputtering*, Mat. Res. Soc. Sym. Proc., 362-366 (1994)

30. A. Okada, *Some electrical and optical properties of ferroelectric PZT thin films*, J. Appl. Phys., **48**(7), 2905-2909 (1977)

31. K. Sreenivas, M. Sayer and P. Garret, *Properties of DC magnetron sputtered lead zirconate titanate thin films*, Thin Solid Films, **172**, 251-267 (1989)

32. R. Bruchhaus, D. Pitzer, R. Primig, M. Schreiter and W. Wersing, *Sputtering of PZT thin films for surface micromachined IR-detector arrays*, Integrated Ferroelectrics, **25**, 1-11 (1999)

33. H.R. Kim, S. Jeong, C.B. Jeon et al, *Metalorganic chemical vapor deposition of very thin* $Pb(Zr,Ti)O_3$ *thin films at low temperatures for high-density ferroelectric memory applications*, J. Mater. Res., **16**(12), 3583-3591 (2001).

34. H. Funakubo, A. Nagai, J. Minamidate et al, *Trial for making three dimensional PZT capacitor for high density ferroelectric random access memory*, Integrated Ferroelectrics, **81**, 219-226 (2006)

35. C.S. Hwang, *(Ba,Sr)TiO3 thin films for ultra large scale dynamic random access memory. A review on the process integration*, Mat. Sci. and Eng. B-so. Sta. Mater. for Advan. Tech., **56**(2-3), 178-190 (1998)

36. T. Li, P. Zawadzki and R. A. Stall, *Microstructure and properties of PZT thin films made by one ant two step MOCVD*, Integrated Ferroelectrics, **18**, 155-169 (1997)

37. E. Hong, J.C. Shin, J. Choi, C.S. Hwang and H.J. Kim, *Preparation and characterization of PZT thin films by MOCVD using a solid delivery system*, J. Mater. Res., **15**(6), 1284-1290 (2000)

38. H. Funakubo, G. Asano, A. Nagai, H. Morioka, S. Yokoyama, T. Shibutami, N. Oshima and K. Akiyama, *Property improvement of MOCVD-PZT films deposited below 400°C*, Mat. Res. Soc. Symp. Proc., **784**, (2003)

39. J. Fukushima, K. Kodaira, and T. Matsushita, *Preparation of ferroelectric PZT films by thermal-decomposition of organometallic compounds*, J. Mater. Sci., **19**(2), 595-598 (1984)

40. R.W. Vest and J. Xu, *Preparation and properties of PLZT films from metallo-organic precusors*, Ferroelectrics, **93**, 21-29 (1989)

41. B.A. Tuttle, R.W. Schwartz, D.H. Doughty and J.A. Voigt, *Characterization of chemically prepared PZT thin films*, in Ferroelectric Thin Films, Mat. Res. Soc. Symp. Proc., **200**, 159-165, (1990)

42. M. Klee, P. Schnabel, W. Brand, and R. Mauczok, *Ferroelectric layers made by thermal decomposition of organometallic compounds*, in 1990 IEEE 7th International Symposium on Applied Ferroelectrics, IEEE Catalog no. 09CH28001, 685-688 (1991)

43. J. Livage, M. Henry and C. Sanchez, *Sol-gel chemistry of transition metal oxides*, Solid State chemistry, **18**, 259-341 (1988)

44. C.J. Brinker and G.W. Scherer, *Sol-gel science: the physics and chemistry of sol-gel processing*, Academic Press, INC., San Diego (1990)

45. S.R. Gurdovich an J.B. Blum, *Preparation of monolithic lead-titanate by sol-gel process*, in Ultrastructure Processing of Ceramics, Glasses and Composites, L.L.H.a.D.R. Ulrich, Editor, Wiley-Interscience, New York, 152-160 (1984)

46. K.D. Budd, S.K. Dey, and D.A. Payne, *Sol-gel processing of PT, PZ, PZT and PLZT thin films*, Brit. Cer. Soc. Proc., **36**, 107-121 (1985)

47. R.W. Schwartz, B.C. Bunker, D.B. Dimos, R.A. Assink, B.A.Tuttle, D.R. Tallant, and I.A. Weinstock, *Solution chemistry effects in PZT thin film processing*, Integrated Ferroelectrics, **2**, 243-254 (1992)

48. R.W. Schwartz, T.J. Boyle, S.J. Lockwood, M.B. Sinclair, D. Dimos and C.D. Buchheit, *Sol-gel processing of PZT thin films: A review of state-of-the-art and process optimization strategies*, Integrated Ferroelectrics, **7**(1-4), 259-277 (1995)

49. R.W. Schwartz, J.A. Voigt, B.A. Tuttle, R.S. DaSalla and D.A. Payne, *Comments on the effects of solution precursor characteristics and thermal processing conditions on the crystallization behaviour of sol-gel derived lead zirconate titanate thin films*, J. Mat. Res., **12**(2), 444-456 (1997)

50. R.W. Schwartz, *Chemical solution deposition of perovskite thin films*, Chem. Mater., **9**, 2325-2340 (1997)

51. X. Li, J. Liu, Y. Zeng and J. Liang, *Low-temperature in situ preparation of ferroelectric PZT thin films by reactive sputtering*, Appl. Phys. Lett., **63**(17), 2345-2347 (1993)

52. T. Maeder, P. Muralt, M. Kohli, A. Kholkin and N. Setter, *$Pb(Zr,Ti)O_3$ thin films by in-situ reactive sputtering on micromachined membranes for micromechanical application*, British Ceram. Proc., **54**, 206-218 (1995)

53. N. J. Wu, A. Ignatiev, A. W. Mesarwi, H. Lin, K. Xie and H.D. Shih, *Heterostructures of PZT and YBaCuO on MgO substrate prepared by PLD*, Jpn. J. Appl. Phys., **32**, 5019-5023 (1993)

54. R. Ramesh, O. Auciello, V.G. Keramidas and R. Dat, *PLD-deposition and characterization of ferroelectric metal oxide heterostructures*, Science and Technology of Electroceramic Thin Films, **284**, 1-22 (1995)

55. M.J. Lefevre, J.S. Speck, R.W. Schwartz, D. Dimos, and S.J. Lockwood, *Microstructure development in sol-gel derived lead zirconate titanate thin films: the role of precursor stoiechiometry and processing environment*, J. Mat. Res., **11**(8), 2076-2084 (1996)

56. K.C. Chen and J.D. Mackenzie, *Crystallization kinetics of metallo-organics derived thin film*, Mat. Res. Soc. Sym. Proc., **180**, 663-668 (1990)

57. K.G. Brooks, J.M. Reaney, R.D. Klissurska, Y. Huand, L. Bursil and N. Setter, *Orientation of rapid thermally annealed lead zirconate titanate thin films on (111) Pt substrate*, J. Mat. Res., **9**(10), 2540-2553 (1994)

58. M. Klee, A. de Veirman, P. van de Weijer, U. Mackens and H. van. Hal, *Analytical study of the growth of polycrystalline titanate thin films*, Philips J. of Res., **47**(3-5), 263-285 (1993)

59. M. Klee, R. Eusemann, R. Waser, H. Van Hal and W. Brand, *Processing and electrical-properties of $Pb(Zr_xTi_{1-x})O_3$ (x = 0.2-0.75) films – Comparison of metalo-organic decomposition and sol-gel processes*, J. of Appl. Phys., **72**(4), 1566-1576 (1992)

60. C.W. Law, K.Y. Tong, J.H. Li and K. Li, *Effect of pyrolysis temperature on the characteristics of PZT films deposited by the sol-gel method*, Thin Solid Films, **335**(1-2), 220-224 (1998)

61. J. M. Marshall, Q. Zhang, Z. Huang and R. W. Whatmore, *Orientation control of low temperature deposited sol-gel PZT 52/48 films*, Ferroelectrics, **318**, 41-48 (2005)

62. K. Aoki, Y. Fukuda, K. Numata, and A. Nishimura, *Dielectric properties of (111) and (100) lead-zirconate-titanate films prepared by sol-gel technique*, Jpn. J. Appl. Phys., **33**, 5155-5158 (1994)

63. P. Muralt, T. Maeder, L. Sagalowicz, S. Hiboux, S. Scalese, D. Naumovic, R.G.Agostino, N. Xanthopoulos, H. J. Mathieu, L. Patthey, and E.L. Bullock, *Texture control of $PbTiO_3$ and $Pb(Zr,Ti)O_3$ thin films with TiO_2 seeding*, J. Appl. Phys., **83**(7), 3835-3841 (1998)

64. S. Hiboux and P. Muralt, *Piezoelectric and dielectric properties of sputter deposited (111), (100) and random-textured $Pb(Zr_xTi_{1-x})O_3$ (PZT) thin films*, Ferroelectrics, **224**, 315-322 (1999)

65. S. Hiboux, *Study of growth and properties of in-situ sputter deposited PZT thin films*, Thesis n° 2510, EPFL (2001)

66. E. Cattan, R. Roma, G. Velu, B. Jaber, D. Remiens and B. Thierry, *Influence of $PbTiO_3$ buffer layers on microstructural properties of PZT films deposited by sputtering*, Mat. Res. Soc. Symp. Proc., **433**, 291-296 (1996)

67. N. Ledermann, P. Muralt, J. Baborowski, S. Gentil, K. Mukati, M. Cantoni, A. Seifert and N. Setter, *{100}-textured, piezoelectric $Pb(Zr_x, Ti_{1-x})O_3$ thin films for MEMS: integration, deposition and properties*. Sensors and Actuators, **A 105**, 162-170 (2003)

68. S.A. Mansour, G.L. Liedl and R.W. Vest, *Microstructural developments and dielectric properties of rapid thermally processed PZT thin films derived by metallo-organic decomposition*, J. Am. Ceram. Soc., **78**(6), 1617-1623 (1995)

69. S. Trolier-McKinstry, J. Chen, K. Vedam and R.E. Newnham, *In situ annealing of sol-gel ferroelectric thin films by spectroscopic ellipsometry*, J. Am. Ceram. Soc., **78**(7), 1907-1913 (1995)

70. E.M. Griswold, L. Weaver, M. Sayer, F. Czerwinski and J. Szpunar, *Crysrallization kinetics in ferroelectric thin films: Viability of atomic force microscopy*, Micron, **26**(6), 559-564 (1995)

71. O. Babushkin, T. Lindbäck, K. Brooks and N. Setter, *PZT phase formation monitored by high-temperature X-ray diffractometry*, J. of the Europ. Ceram. Soc., **17**, 813-818 (1997)

72. V.Y. Shur, E.B. Blankova, A.L. Subbotin, E.A. Borisova and A.V. Barannikov, *Phase transformation kinetics induced in thin sol-gel PZT films under thermal annealing*, Phys. of Solid State, **43**(5), 902-907 (2001)

73. Y.-M. Sung and W.-C. Kwak, *Fluorite-to-Aurivillius phase transformation kinetics in sol-gel derived SBT thin films*, Chem. Phys. Lett., **411**, 389-394 (2005)

74. Y.-M. Sung, K.-S. Park, S.M. Park and G.M. Anilkumar, *Formation of nanoporous and nanocrystalline anatase films py pyrolysis of PEO-*TiO_2 *hybrid films*, J. of Crys. Grow., **286**, 173-177 (2006)

75. B. Lee, C. Kim, S.-H. Kim and H. Shin, *Revisit of phase transformation kinetics in PZT thin films by sol-gel method using scanning force microscopy*, Integrated Ferroelectrics, **68**, 247-258 (2004)

76. A.P. Wikinson, J.S. Speck. A.K. Cheetham, S. Natarajan and J.M. Thomas, *In Situ X-ray diffraction study of crystallization kinetics in* $PbZr_{1-x}Ti_xO_3$ *(PZT, x = 0.0, 0.55, 1.0)*, Chem. Mater., **6**, 750-754 (1994)

77. D.A. Berlincourt, C. Cmolik, and H. Jaffe, *Piezoelectric properties of polycrystalline PZT compositions,* in Proceedings of the IRE, Institute of Radio Engineers, New York (1960)

78. P. Luginbuhl, G. Racine, P. Lerch, B. Romanowicz, K. Brooks, N. deRooij and P. Renaud, *Piezoelectric cantilever beams actuated by PZT sol-gel thin film*, Sensors and Actuators, **A 54**, 530-535 (1996)

79. M.-A. Dubois and P. Muralt, *Measurement of the effective transverse piezoelectric coefficient* $e_{31,f}$ *of AlN and PZT thin film*, Sensors and Actuators, **A 77**(2), 106-112 (1999)

80. J.F. Shepard Jr., F. Chu, I. Kanno and S. Trolier-McKinstry, *Characterization and aging response of the* d_{31} *piezoelectric coefficient of lead Zirconate titanate thin films*, J. Appl. Phys., **85**(9), 6711-6716 (1999)

81. J.F. Shepard Jr., P. Moses and S. Trolier-McKinstry, *The wafer flexure technique for the determination of the transverse piezoelectric coefficient (*d_{31}*) of PZT thin films*, Sensors and Actuators, **A 71**, 133-138 (1998)

82. E. Defaÿ, C. Zinck, C. Malhaire, N. Baboux and D. Barbier, *Modified free vibrating beam method for characterization of effective* e_{31} *coefficient and leakage resistance of piezoelectric thin films*, Review of Scientist Instruments, **77**, 103903 (2006)

83. R.A. Wolf and S. Trolier-McKinstry, *Temperature dependence of piezoelectric response in lead zirconate titanate films*, J. Appl. Phys., **95**, 1397-1406 (2006)

84. S. Yokoyama, S. Okamoto, H. Funakubo, T. Iijima, H. Okino, T. Yamamoto, K. Nishida, T. Katoda and J. Sakai, *Crystal structure, electrical properties, and mechanical response of (100)-/(001)-oriented epitaxial* $Pb(Mg_{1/3}Nb_{2/3})O_3$*-*$PbTiO_3$ *films grown on*

$(100)_c$SrRuO_3||(100)SrTiO_3 subsrtate by metal-organic chemical vapor deposition, J. Appl. Phys., **100**, 054110 (2006)

85. J.-P. Maria, J.F. Shepard Jr., S. Trolier-McKinstry, T.R. Watkins and A.E. Payzant, *Characterization of the piezoelectric properties of $Pb_{0.98}Ba_{0.02}(Mg_{1/3}Nb_{2/3})O_3$ $PbTiO_3$ epitaxial thin fims*, Int. J. Appl. Ceram. Technol., **2**, 51-58 (2005)

86. N.B. Gharb and S. Trolier-McKinstry, *Dielectric nonlinearity of $Pb(Yb_{1/2}Nb_{1/2})O_3$-$PbTiO_3$ thin films with {100} and {111} crystallographic orientation*, J. Appl. Phys., **97**, 064106 (2005)

87. S. Sherrit, H.D. Wiederick, B.K. Mukherjee, *A complete characterization of the piezoelectric, dielectric and elastic properties of Motorola PZT 3203 HD including losses and dispersion*, Proc. SPIE 3037, 158–169 (1997)

88. E.W. Becker, W. Ehrfeld, P. Hagman, A. Maner and D. Müenchmayer, *Fabrication of microstructures with high aspect ratios and great structural heights by synchrotron radiation lithography, galvanoforming, and plastic moulding (LIGA process)*, Microelectron. Eng., **4**(1), 35-56 (1986)

89. H. Guckel, T.R. Christenson, K.J. Skrobis, D.D. Denton, B. Choi, F.G. Lovell, J.W. Lee, S.S. Bajkar, T.W. Chapman, *Deep X-Ray and UV Lithographies for Micromechanics*, IEEE Solid State Sensor and Actuator Wisconsin Workshop, Hilton Head, SC, 118-122 (1990)

90. L.T. Romankiw, *A path: from electroplating through lithographic masks in electronics to LIGA in MEMS*, Electrochim. Acta, **42**(20-22), 2985-3005 (1997)

91. A. Cohen, G. Zang, F.-G. Tseng, F. Mansfeld and P. Will, *EFAB: Rapid, Low-Cost Desktop Micromachining of High Aspect Ratio True 3-D MEMS*, Technical Digest of The 12th IEEE International conference on Micro Electro Mechanical Systems, Orlando, Florida, 244-251 (1999)

92. Z.W. Tian, Z.D. Feng, Z.Q. Tian, X.D. Zhuo, J.Q. Mu, C.Z. Li, H.S. Lin, B. Ren, Z.X. Xie and W.L. Hu, *Confined etchant layer technique for two-dimensional lithography at high resolution using electrochemical scanning tunneling microscopy*, Faraday Discuss, **94**, 37 44 (1992)

93. R. Schuster, V. Kircher, P. Allongue and G. Ertl, *Electrochemical Micromachining*, Science, **289**(5476), 98-101 (2000)

94. D. Reynaerts, W. Meeusen and H. Van Brussel, *Machining of three-dimensional microstructures in silicon by electro-discharge machining*, Sensors and Actuators, **A 67**(1-3), 159-165 (1998)

95. C. van Osenbruggen, *Micro spark erosion* (in Dutch), Philips Technisch Tijdschrift, **20**, 200–213 (1969)

96. R. Snoeys, F. Staelens and W. Dekeyser, *Current trends in non-conventional material removal processes*, Annals CIRP, **35**, 467–480 (1980)

97. N. Chomnawang and J.-B. Lee, *On-chip 3D micro-inductor for high-frequency applications using deformation of sacrificial polymer*, Department of Electrical and Computer Engineering, Louisiana State University, Baton Rouge (2002)

98. from Tyndall National Institute website : www.tyndall.ie/PDFs/plating.pdf

99. E. Lennon and F. Ayela, *Electrodeposition through thick photoresist moulds for the synthesis of a sharp chromium microtip*, J. of Micromech. and Microeng., **12**, 122-127 (2002)

100. M. Ichiki, L. Zhang, Z. Yang, T. Ikeharaa nd R. Maeda, *Spray coating fabrication: thin film formation on non-planar surface*, Proc. Transducers, 825 – 828 (2003)

101. N.P. Pham, E. Boellard, J.N. Burghartz and P.M. Sarro, *Photoresist coating methods for the integration of novel 3-D RF microstructures*, J. MEMS, **13**(3), 491–499 (2004)

102. C. Christensen, P. Kersten. S. Bouwstra. and J. W. Petersen, *Wafer through-hole interconnections with high vertical wiring densities*, IEEE Trans. Comp. Pack. Manu. Tech. A, **19**(4), 516-522 (1996)

103. S. Linder, H. Bakes, F. Gnaedinger and E. Doering, *Photolithography in anisotropically etched grooves*, Proc. 9th IEEE MEMS 96 Technical Digest, 38-43 (1996)

104. M. Parodi, T. Batchelder, P. Haaland, and J. McKibben, *Spin coating and alternative techniques for flat panel displays*, Semiconductor Int., **19**(1), 101-106 (1996)

3

GROWTH, OPTIMIZATION & CHARACTERIZATION OF SOL-GEL PZT THIN FILMS

3.1 SOL-GEL DEPOSITION OF PZT

3.2 GROWTH STUDIES

3.3 FUNCTIONAL PROPERTIES

3.4 SUMMARY

3.5 REFERENCES

Chemical solution deposition (CSD) of PZT is still continuing to progress. On the one hand, improvements were made in solution chemistry and preparation, as well as in heat treatments for crystallization. On the other hand, a lot of work was spent to improve growth substrates for the seeding of desired film textures. The activation energy for nucleation of a specific orientation can be lowered by a suitable growth substrate. As explained earlier, for PZT deposition on Pt(111) electrodes, efficient seed layers were found in the form of about 10-15nm thick $PbTiO_3$\{100\} thin films for the \{100\}-orientation, and 2nm thick TiO_2(100) thin films for the \{111\}-orientation. The goal in this work is to optimize the \{100\}-texture. This chapter is devoted to the study and improvement of processing and properties of sol-gel grown thin PZT films by the sol-gel method. This includes the optimization of the $PbTiO_3$\{100\} seed layer, including the uniformity on a whole 4 inch wafer. The removal of the concentration gradient in B-site occupancy ratio (Zr/Ti) was identified as essential step for further improvements.

3.1 SOL-GEL DEPOSITION OF PZT

3.1.1 PRECURSOR SOLUTION PREPARATION

Six precursor solutions of rhombohedral, MPB and tetragonal $Pb(Zr_x,Ti_{1-x})O_3$ composition with x = 0.63, 0.58, 0.53, 0.48 and 0.43 are synthesized using an improved 2-methoxyethanol route of Budd *et al* [1] and Gurkovich and Blum [2]. The first step of precursor preparation is the dissolution of the lead acetate reagent in 2-methoxyethanol during 45 minutes at 100°C and 500mbar as shown on Figure 3.1. This step is followed by a distillation to remove the water during 30 minutes at 125°C and 300mbar. The dehydrated powder is re-dissolved in dry 2-methoxyethanol during 1h at 105°C and 500mbar. Titanium and zirconium alkoxides are added and the solution is refluxed during 3h at 100°C and 500mbar. A vacuum distillation at 300mbar and 110°C is used to remove reaction by-products and to adjust the concentration of the precursors to 0.45M.

To improve the drying behavior of the sol–gel, 4 vol.% formamide is added to the solution (inhibition of the hydrolysis [3]). The solution is then filtered through 0.45µm PTFE syringe filter and stored under dry argon. Two solution precursors are prepared in order to balance the lead loss during the rapid thermal annealing (RTA). The standard one has 10% lead excess and the solution used for the last layer before the RTA has 30% lead excess.

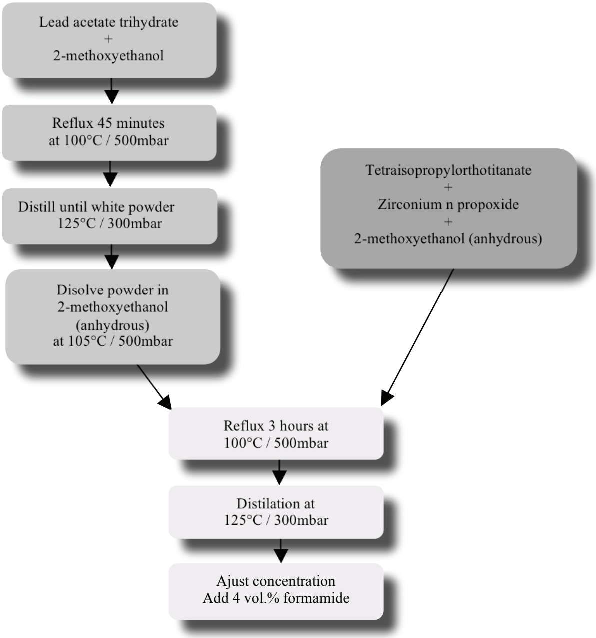

Figure 3.1: Schematic of the PZT solution precursors preparation.

3.1.2 DEPOSITION AND CRYSTALLIZATION OF PZT

The CSD PZT thin films are deposited on platinized silicon wafers ((111)-textured Pt electrodes as obtained from sputter deposition at 300°C in a Balzers, BAS 450) by multiple spin coating of the solution precursors, each layer is subsequently pyrolyzed at 350°C for 20 seconds as shown on Figure 3.2. After the deposition of four single layers (three layers with 10% lead excess, one layer with 30% lead excess), the PZT film is thermally annealed at 650°C for 1 minute using a rapid heating module (Qualiflow Therm, Jipelec JetFirst 150) in 100sccm flowing oxygen. During the heating ramp (15 °C/s), a short plateau at 520°C is applied to favor crystallization of {100} grains (as proposed in [4]). As the heating rate is very fast, this step serves as well to avoid overshoot of temperature. As film thickness of a single spin is about 60nm, 4 and 32 single layers are required to form 250nm and 2µm PZT film respectively.

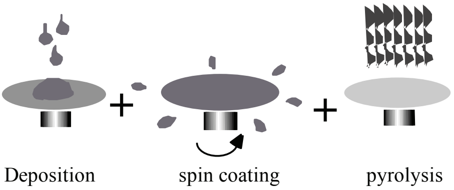

Figure 3.2: Schematic view of the sol-gel deposition technique.

3.2 GROWTH STUDIES

3.2.1 OPTIMIZATION OF SOL-GEL SEED LAYER

It has been shown that {100}-textured PZT of morphotropic composition fabricated by chemical solution deposition (CSD) provides the highest transverse piezoelectric coefficient [5]. This specific texture was obtained in earlier work using a seeding layer of sputter deposited $PbTiO_3$ [6]. However, in a CSD process it is advantageous to be also able to produce the seed layer by chemical methods. The solution used in this study was made in the same way as described before for PZT, with the difference that the $PbTiO_3$ precursor contains 30% lead excess to enhance seed layer orientation and to avoid problems related to lead evaporation. In addition, the final solution was diluted with 2-methoxyethanol to obtain a thinner film. The $PbTiO_3$ seed layer was deposited on a platinized wafer ($Pt/TiO_2/SiO_2/Si$) using spin coating at 3000 rpm for 40s. The film was subsequently pyrolyzed at 350°C for 60 seconds to evaporate the solvent and pyrolyze the organics after which the seed layer is crystallized by RTA at 650°C for 60 seconds.

Four different crystallization conditions have been applied on the deposited pyrolysed seed layer to study the phase growth and orientation of grains. These anneal conditions are shown in Figure 3.3. The four different processes stop at 520°C (A), 550°C (B), 650°C 0sec (C) and 650°C 60sec (D) respectively. The corresponding X–ray diffractions (Kristalloflex 805 (Siemens, Germany) with Cu Kα radiation), using θ-2θ scans from 20 to 50 degrees, are presented in Figure 3.4. On the first diffraction pattern (A), no crystallization peaks are visible. The layer is still amorphous. The film begins to crystallize in the perovskite phase between 520° and 550°C as the {100}-oriented PTO peaks appear on the diffraction pattern (B). No significant differences are visible on diffraction pattern (B), (C) and (D). The (100)-peak is the strongest one. A closer look on the (111) platinum peak (see Figure 3.5), reveals an increase in the intensity of the latter. This is due to the recrystallization of the Pt layer when reaching 650°C (C) and staying at this temperature for 60 seconds (D). There is in addition a shift of the Pt(111) peak due to an imposed strain. Following the Bragg equation:

$$2d\sin\theta = n\lambda, \tag{3.1}$$

the shift to a higher theta angle means that the distance between the (111) planes (d) is decreasing. This negative out-of-plane strain is caused by a tensile stress of the film. The strain value of 0.48% - as derived in comparison to the lattice constant of powder - corresponds to a tensile stress of 800MPa. It can be entirely explained by non-relaxed thermal mismatch during cool down.

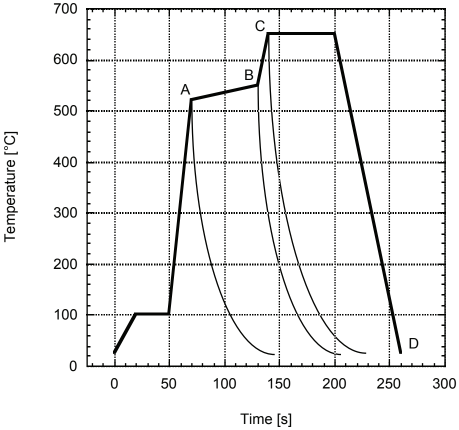

Figure 3.3: A, B, C and D anneal conditions for $PbTiO_3$ seed layer crystallization.

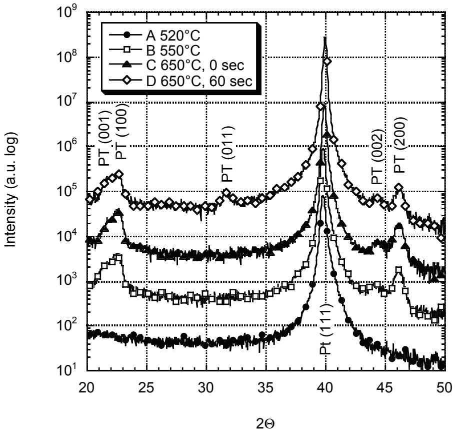

Figure 3.4: X-ray diffractogram of 1 layer (15nm) of $PbTiO_3$ at different crystallization conditions.

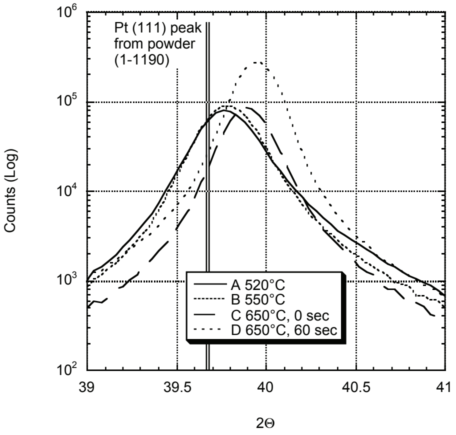

Figure 3.5: X-ray diffraction pattern of (111) Platinum under different crystallization conditions of the seed layer.

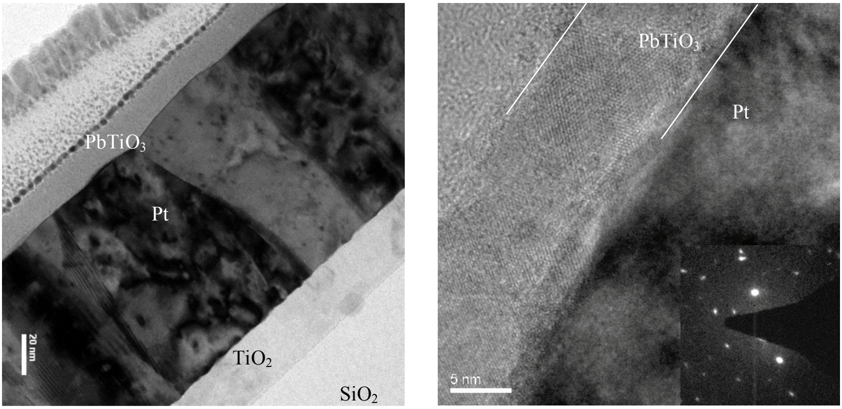

(a) (b)

***Figure 3.6:** TEM micrographs of lead titanate seed layer deposited on 100nm platinum bottom electrode and 25nm titanium dioxide barrier layer. (a) ~18nm amorphous PT annealed at 520°C and (b) ~15nm crystallized PTO annealed at 550°C with corresponding diffraction pattern. (C. Sandu)*

More details on the effect of annealing were obtained by transmission electron microscopy (TEM) (Philips CM 300). As can be seen in Figure 3.6, the PTO layer is still amorphous after annealing at 520°C, confirming the information gathered from XRD. After annealing at 550°C, a polycrystalline microstructure appears, showing the perovskite diffraction peaks as expected. The shrinkage during crystallization amounts to 18%. The fact that this film contains mostly a-domains can be explained by the large tensile residual stress resulting from the shrinkage. The observed crystallization temperature somewhere between 520 and 550°C is higher than reported in the literature. Kwak and Desu give a temperature of 500°C for a complete transformation to perovskite on sapphire [7]. They apply, however, longer annealing times.

The new seed layer was benchmarked against the sputter deposited one. For this purpose, 2µm PZT thin films have been deposited on fully platinized 100mm wafers with two differently deposited $PbTiO_3$ seed layers. The first one is deposited by sputtering, and the second one by the above described CSD process. Both PZT films are pyrolysed and crystallized using the same solutions and processes. The crystalline texture and phase analysis of the films are determined by X-ray diffraction θ-2θ scans that are carried out from 20° to 50° at 0.04° increment per 1 second. The texture index of the film (plans parallel to the surface only) was obtained by normalizing the peak intensities with the corresponding peaks of randomly oriented powder according to the following equation [8]:

$$P(hkl) = \frac{\dfrac{I(hkl)}{I_0(hkl)}}{\displaystyle\sum_{1}^{N} \dfrac{I(hkl)}{I_0(hkl)}} \tag{3.2}$$

where N is the number of peaks considered (in our case N = 3 as the relevant orientations are {100}, {110} and {111}) and I(hkl) and I_0(kkl) are the integrated peak intensities of the film and the randomly oriented PZT 52/48 powder (JCPDS file #33-784).

The sputter deposited seed layer is much less uniform than the one obtained by sol-gel. In addition, it exhibits also a 10% small texture index (Figure 3.7). In CSD films, the {100}-texture index amounted to up to 99.3%. This 100% are quite constant on the whole wafer (8 samples).

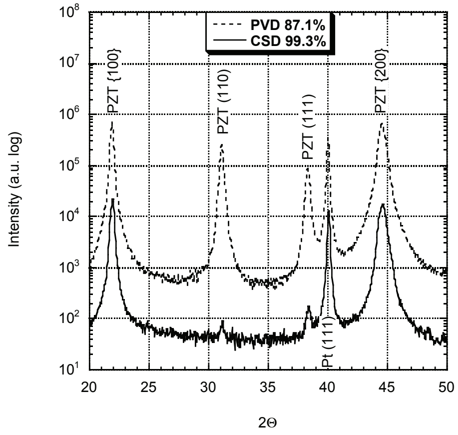

Figure 3.7: X-ray diffractogram of 2 µm sol-gel PZT using different seed layer deposition methods; the sputtered (PVD) and the sol-gel (CSD).

We can conclude that the sol-gel $PbTiO_3$ seed layer enhances the texture degree of PZT as compared to the sputtered version, is less time consuming and gives full homogeneity of {100}-oriented PZT on whole 100mm wafers. This simplifies the deposition procedure compared to a sputtered seed layer, and makes the seeding procedure more practical for PZT MEMS.

3.2.2 PHASE EVOLUTION OF PZT THIN FILMS DURING ANNEALING

The same four different crystallization conditions have been applied on 250nm thick pyrolysed PZT films (consisting of 4 spun layers) to study phase growth and orientation. The annealing conditions are the same as the one applied for the $PbTiO_3$ seed layer (Figure 3.3) with the exception that the ramping time between 520°C and 550°C is 10 seconds instead of 60 seconds. The four different processes stop at 520°C (A), 550°C (B), 650°C 0sec (C) and 650°C 60sec (D), respectively. The corresponding X–ray diffractograms are shown in Figure 3.8. The spectrum of the as pyrolysed film (pyrolysis temperature: 350°C) is shown for comparison.

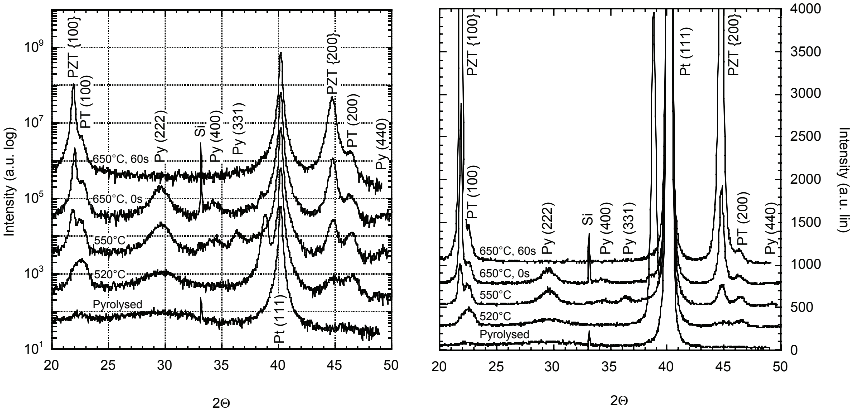

Figure 3.8: X-ray diffractograms with logarithm and linear y-axis of sol-gel PZT (250nm) at different annealing conditions on crystallized sol-gel $PbTiO_3$ seed layer.

The crystallization on the lead titanate seed layer obviously follows the sequence: amorphous film → pyrochlore (Py = $Pb_2Ti_2O_6$) → perovskite. The conversion is completed after the full annealing schema and yields highly {100}-oriented single-phase perovskite (D: 650°C 60sec). Pyrochlore diffraction lines are rather broad, indicating the large compositional range and fine-grained nature of this phase.

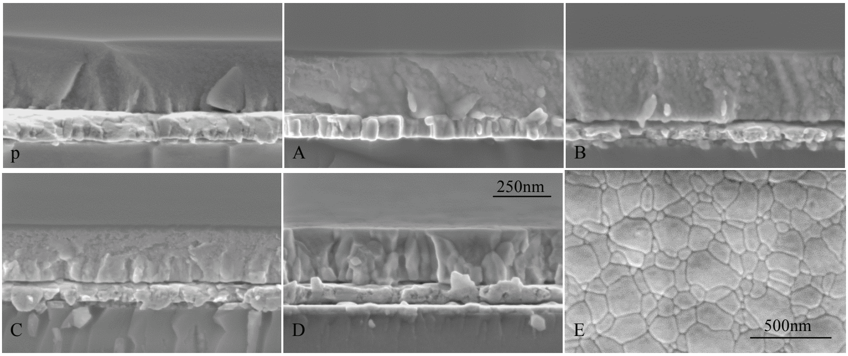

Figure 3.9: ***SEM cross-sections and top view of the 250nm PZT layer annealed under different conditions. (p) pyrolysed layer at 350°C, annealed at (A) 520°C, (B) 550°C, (C) 650°C for 0 second and (D) fully crystallized at 650°C for 60 seconds. (E) top view of the crystallized PZT layer.***

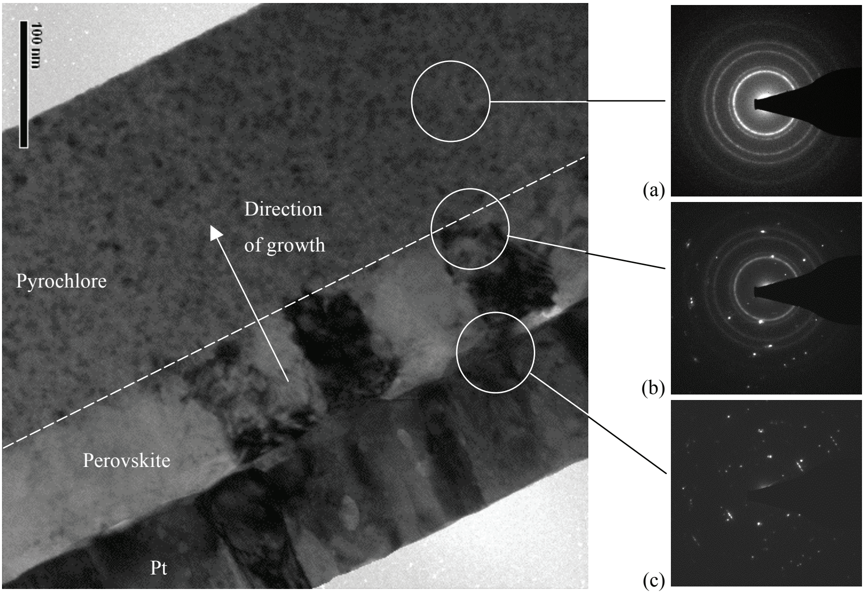

Figure 3.10: ***TEM micrographs of 250nm PZT annealed with the (C) condition of Figure 3.3, i.e. 650°C, 0s. Pattern (a), (b) and (c) show diffractions from pyrochlore phase, pyrochlore/perovskite phases and perovskite/platinum layer respectively. (C. Sandu)***

The SEM (Léo 1550 with GEMINI column) micrographs of Figure 3.9 give information on grain structure and roughly confirm the nature of the phases and the crystallization temperatures obtained from the X-ray diffraction patterns in Figure 3.8. Micrograph (p) shows an amorphous PZT layer of about 350nm. The {100} peak of the (already crystallized) seed layer is hardly detected by XRD when covered with the amorphous PZT phase. The origin of the PTO(100) peak in the XRD after annealing at 520°C (fig. 3.8) is more likely due to a Ti-rich phase growing on the seed layer at an early stage. Very remarkable is the strong peak at 38.8°. This peak is probably due to formation of instable mixed pyrochlore of $Pb_2(Zr, Ti)O_3$ composition. The beginning of crystallization can indeed be seen on top of the bottom electrode starting from the lead titanate seed layer after anneal at 520 °C (micrograph A). The large shrinkage in the PZT layer from 350 nm to 250 nm (~25%) and the granular aspect prove that the amorphous phase is densified or mostly transformed already. As it is difficult to know which phase is actually represented by the Py(222) peak (fluorite or pyrochlore) and as there is still some lead excess present at 520 °C, we align with the idea that the observed peak corresponds best to be $Pb_2Ti_2O_6$ (ref. JCPDS 26-142), an oxygen deficient, metastable variant of the more conventional pyrochlore structure, as proposed by Brooks *et al* [9]. The corresponding X-ray pattern indicates that the 520°C PZT consists mostly of Py(222), with distinguishable PTO perovskite {100} seed layer. No significant structural changes are observed between micrograph (A) and (B), but the instable mixed pyrochlore $Pb_2(Zr, Ti)O_3$ peak has disappeared and PZT {100}-orientation is appearing, as well as intensified pyrochlore (222) and (331). The latter could be responsible for the more granular aspect as shown in micrograph B. On the micrograph (C), two distinct phases are observed. The lower part of the PZT film is crystallized in the {100}-oriented perovskite phase, while the upper part still contains the pyrochlore phase. Figure 3.10 shows the corresponding TEM micrograph and resulting diffraction patterns of each present phase. It illustrates the massive pyrochlore nanograins present in the upper part of the film, possibly mixed with amorphous phases. The lower part is entirely crystallized (in PZT{100}). This picture illustrates well the heterogeneous nucleation of the perovskite on the seed layer, followed by columnar growth, and the homogeneous nucleation of the pyrochlore throughout the film. At the stage of the observed film, the nucleation front is astonishingly smooth, and approximates a homogeneous growth behavior (far away from dendritic growth). This is supported by Avrami coefficients close to 1 in sol-gel growth of thin films [10]. The perovskite grows into the pyrochlore / amorphous matrix. The pyrochlore phase diffraction pattern (a) exhibits rings showing the presence of $Pb_2Ti_2O_6$ pyrochlore-type. On diffraction pattern (b), both pyrochlore and {100}-oriented perovskite phase are present. And on diffraction pattern (c), PZT perovskite and (111) platinum can be seen. Micrograph (D) and (F) of Figure 3.9 illustrate the fully crystallized perovskite layer free of second phases, including the surface.

3.2.3 GRADIENT FREE SOL-GEL PZT THIN FILMS

One of the striking differences between thin films [5, 11] and bulk materials is the relatively moderate peaking of properties at the morphotropic phase boundary (MPB) of films, as compared to ceramics [12] or theoretical PZT behavior derived from ion displacements [13] as shown on Figure 3.11. One of the reasons was revealed in 1994 by Amanuma *et al* [14] using Auger electron spectroscopy (AES) and quantified in 2003 by Ledermann *et al* [5] using energy dispersive X-ray analysis (EDX): a strong gradient of Zr/Ti compositional ratio was observed, reaching from 0.79 (44/56) on the bottom of the layer to 1.9 (65/35) at the top of the layer. The average ratio was 1.12 (53/47) as given by the concentrations in the solution. Knowing the large variation of e.g. electrostrictive coefficients with composition [15], and the large importance of domain contributions at the MPB, any gradient is expected to deteriorate properties at the MPB.

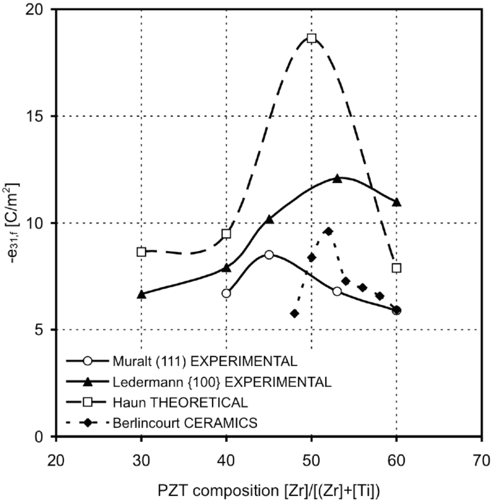

Figure 3.11: ***Relative peaking of properties of sol-gel PZT thin film in (111)-orientation (Muralt [11]) and in {100}-orientation (Ledermann [5]) as compared to theoretical single-phase single-domains ceramic model (Haun [13]) and PZT bulk ceramics (Berlincourt [12]).***

3.2.3.1 Zr/Ti content calculation for gradient free PZT films

Compositional gradients in sol-gel processing are formed during crystallization anneal. For the present discussion we are considering a phase transformation from an amorphous phase of metal oxides, as obtained after pyrolysis, to a perovskite phase, thus ignoring effects by the occurrence of transient phases (fluorites, pyrochlores) that are reported for complexer systems such as Pb_2ScTaO_6 [16], slow heating rates [17] or high pyrolysis temperatures [9]. We are dealing with heterogeneous nucleation, often also referred to as nucleation controlled growth, meaning that the perovskite phase starts growing from the interface to the substrate layer. This behavior was frequently reported for good quality films [9], and is in fact a stringent condition for obtaining columnar grains. It is also known that Ti-rich compositions nucleate and grow more easily, because the transformation to perovskite is more exothermic with increasing Ti concentration (see discussions and data in ref. 18). Diffusion inside the non-reacted, amorphous part is larger than in the crystalline phase where it is practically zero for the cations due to the low growth temperature (i.e 650°C) as compared to temperatures at which A and B-site cations start to migrate (above 850°C). In order to get a theoretical access to the problem, we consider one-dimensional growth along one direction (designed as z), since the grains are much longer (2µm in our case) than wide (about 200 to 300nm in our case). True three-dimensional (3D) growth is restricted to the first tenths of nanometers, passing to a one-dimensional one for larger thicknesses. This is supported by measured Avrami coefficients close to 1 in sol-gel growth of thin films [19]. We consider the layer before the growth front at z=s in an interval ds. This layer is a kind of adlayer from which the crystal takes the atoms, and to which the amorphous phase delivers or removes atoms that are taken in excess, or repelled in excess, respectively. The flux into the crystalline phase $j^{(c)}$ is proportional to the atom concentrations $c_{Ti}^{(\alpha)}(s)$ and $c_{Zr}^{(\alpha)}(s)$ in the amorphous phase, and proportional to specific rates (or speeds, unit is m/s) κ_{Ti} and κ_{Zr} at which Ti and Zr are integrated into the perovskite lattice.

$$\begin{aligned} j_{Ti}^{(c)}(s) &= \kappa_{Ti} c_{Ti}^{(\alpha)}(s) \\ j_{Zr}^{(c)}(s) &= \kappa_{Zr} c_{Zr}^{(\alpha)}(s) \end{aligned} \tag{3.3}$$

To keep the model simple, we assume that the total density of Zr and Ti is always the same (no shrinkage in volume), i.e.

$$c_0 = c_{Ti}^{(\alpha)}(x) + c_{Zr}^{(\alpha)}(x) = c_{Ti}^{(c)}(x) + c_{Zr}^{(c)}(x) \tag{3.4}$$

The total flux into the crystal phase

$$j^{(c)}(s) = \kappa_{Ti} c_{Ti}^{(\alpha)}(s) + \kappa_{Zr} c_{Zr}^{(\alpha)}(s) = \kappa_{Zr} c_0 + (\kappa_{Ti} - \kappa_{Zr}) c_{Ti}^{(\alpha)}(s) \tag{3.5}$$

defines the propagation speed of the crystal front as

$$v(s) = \frac{j^{(c)}(s)}{c_0} = \kappa_{Zr} + (\kappa_{Ti} - \kappa_{Zr})\frac{c_{Ti}^{(\alpha)}(s)}{c_0} \tag{3.6}$$

As we know that $\kappa_{Ti} > \kappa_{Zr}$, the growth speed slows down with increasing Zr concentration. The Ti and Zr concentrations in the crystal phase are obtained as $c_{Ti}^{(c)}(s)ds = j_{Ti}^{(c)}(s)dt$ and $c_{Zr}^{(c)}(s)ds = j_{Zr}^{(c)}(s)dt$. The relative Zr concentration in the perovskite phase $\gamma_{Zr}^{(c)}$ is obtained from the one in the amorphous phase $\gamma_{Zr}^{(\alpha)}$ as follows

$$\gamma_{Zr}^{(c)} = \frac{c_{Zr}^{(c)}}{c_{Zr}^{(c)} + c_{Ti}^{(c)}} = \frac{j_{Zr}^{(c)}}{j_{Zr}^{(c)} + j_{Ti}^{(c)}} = \frac{r\gamma_{Zr}^{(\alpha)}}{\left[1 - (1 - r)\gamma_{Zr}^{(\alpha)}\right]} \tag{3.7}$$

where r is the relative rate for Zr: $r = \kappa_{Zr} / \kappa_{Ti}$. There is a diffusion flux $j^{(d)}$ in the amorphous phase accounting for the supply/removal of atoms. This flux is expressed as:

$$j^{(d)}(s) = v\left(c^{(\alpha)}(s) - c^{(c)}(s)\right) \tag{3.8}$$

where it is understood that the concentration in the perovskite phase is the one after the crystallization front has passed the time dt afterwards. Related to the diffusion flux, a gradient in the amorphous phase will be installed adjacent to the adlayer according to the diffusion constant D:

$$j^{(d)}(s) = -D\frac{\partial c^{(\alpha)}}{dz} \tag{3.9}$$

It is clear that the diffusion flux must be quite large to match observed compositional gradients. Diffusion velocities must be several times larger than the velocity of the growth front. We used a simple approach to estimate the relative rate coefficient r. We know the concentrations in the amorphous phase at least at the beginning of growth. In order to pass from 53% Zr to 44% at the bottom of the layer, the rate ratio r must amount to 0.70. We divided one layer of 250nm into four separate layers with thicknesses of approximately 60nm, where each layers was spun and pyrolysed from solutions with different chemical compositions. The average concentration was chosen to be the one of the MPB, i.e. 53% Zr. The calculation yielded a proposed concentration of 63% Zr for the first layer, i.e. 10% in excess. The films were prepared with equidistant concentrations of 63, 58, 48, 43% Zr concentration and deposited on CSD $PbTiO_3$ seed layer.

3.2.3.2 *Film composition*

Figure 3.12 shows EDX profile realized in a TEM facility for (a) a 2µm PZT film using 53/47 standard solutions (“gradient film”), and (b) the 2µm “gradient free” PZT film prepared with the new solutions. Both exhibit the ABO_3 compound stoechiometry of the perovskite structure. That is, for the $Pb(Zr,Ti)O_3$, Pb has 20 atomic % and the sum of Zr and Ti also (Figure 3.12 (c)). As elements of low atomic number are difficult to detect by EDX, the 60 atomic % of the oxygen is extracted from the sum of all elements. The lead content is more homogeneous on the gradient free film.

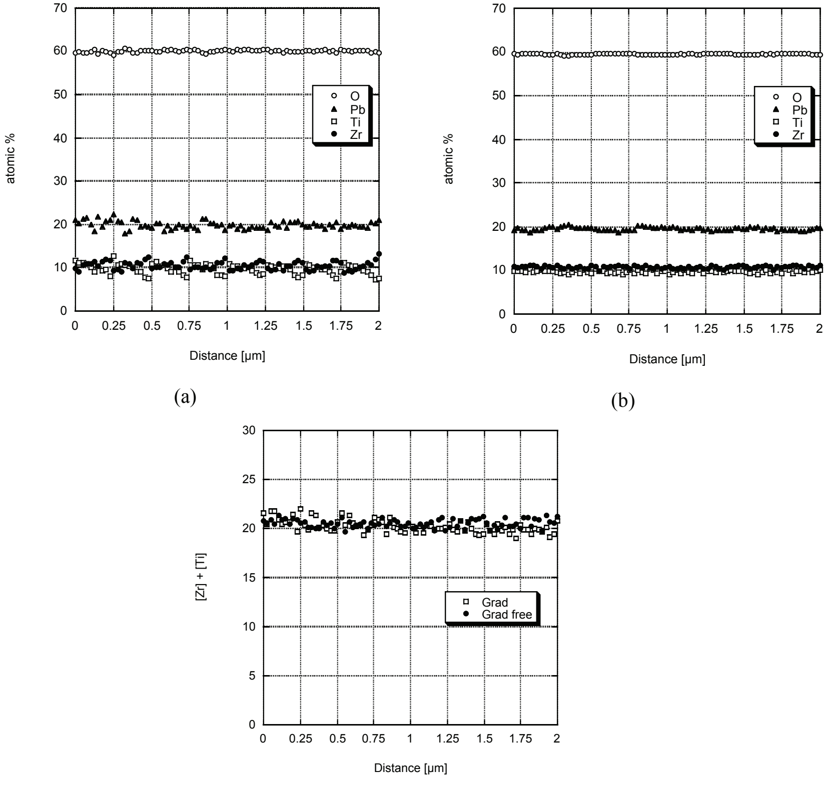

(a)

(b)

(c)

Figure 3.12: O, Pb, Ti and Zr EDX chemical analysis profile in atomic % for (a) gradient PZT film, and (b) gradient free PZT film and (c) Sum of Zr and Ti content in atomic % along the PZT layer for both gradient and gradient free films.

From this EDX analysis, the resulting composition of Zr is evaluated. Figure 3.13 shows the Zr contents of the “gradient free” PZT film, as compared to the gradient PZT film. Both films have otherwise been prepared under the same conditions. The variation of the Zr/Ti composition is very strong in the gradient film with peak concentrations of 45/55 ± 4.7% and 63/37 ± 3.4%, thus confirming the previous results [5]. However, in the gradient free PZT film, the variation of the Zr/Ti composition is much less pronounced staying within 52.5 ± 2.5% Zr.

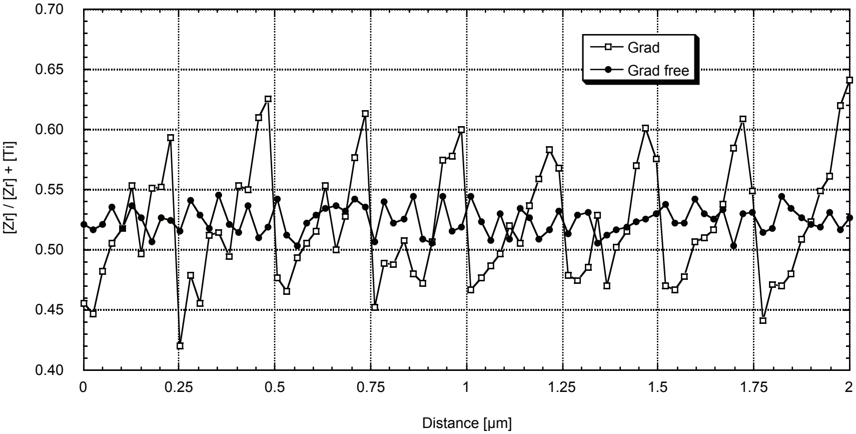

Figure 3.13: Zr content within 2 µm PZT thin films measured as a function of the distance to the bottom electrode.

The TEM cross-section micrographs in dark field contrast (Figure 3.14) reveal a very clear difference in the orientation of crystalline planes. On the gradient film, a difference in the contrast is observed at each crystallization step (columnar grain in the center of the micrograph). Each annealed layer starts with a bright contrast, obviously due to tetragonal symmetry (Ti-rich). Half way in each annealed layer, the contrast changes to dark grey, very compatible with the idea that the symmetry changes to rhombohedral and thus slightly tilts away the planes giving rise to the observed diffraction spot used for the image. In the gradient free film there is no such contrast change observed. The micrograph (b) of Figure 3.14 shows an example of a grain ranging from the bottom to the top electrode. The crystalline phase is much more homogeneous. The chosen diffraction peak is the (201) in both cases. Figure 3.14 shows the diffraction diagram of the gradient free PZT film.

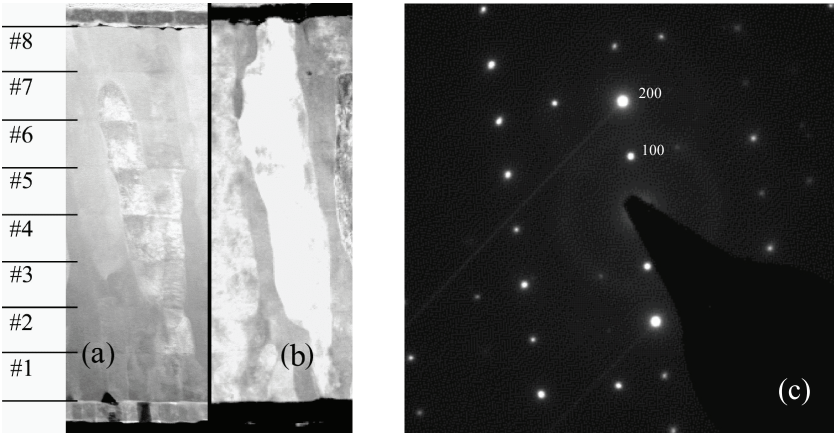

***Figure 3.14:** Dark field TEM images of (a) gradient PZT film, and (b) gradient free PZT film and (c) (201) diffraction diagram of the gradient free PZT film. (M. Charrière)*

3.2.3.3 Microstructure and texture

Figure 3.15 shows SEM micrographs of cross-section and top views of the 2 µm gradient and gradient free PZT films. They show the columnar growth of the grains nucleated on the bottom electrode, and a dense and crack-free morphology. A histogram of the grain size is shown in Figure 3.16 for both gradient and gradient free films. The mean diameter of the grains is 1.5 times larger in the gradient free film (294 nm with 127 nm standard deviation) than in the gradient film (194 nm with 71 nm standard deviation).

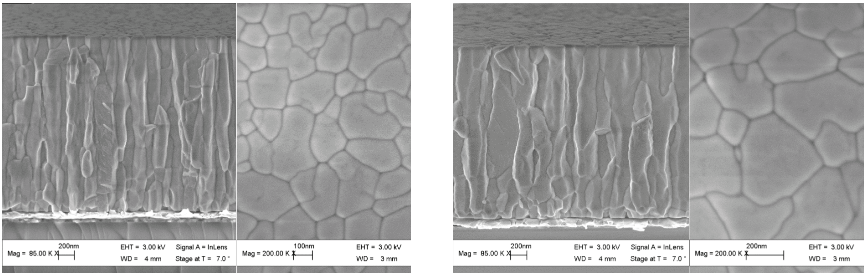

(a) (b)

***Figure 3.15:** SEM cross-section and top views of 2µm PZT {100}-textured Zr/Ti gradient (a) and gradient free (b) PZT thin films (at same magnification)*

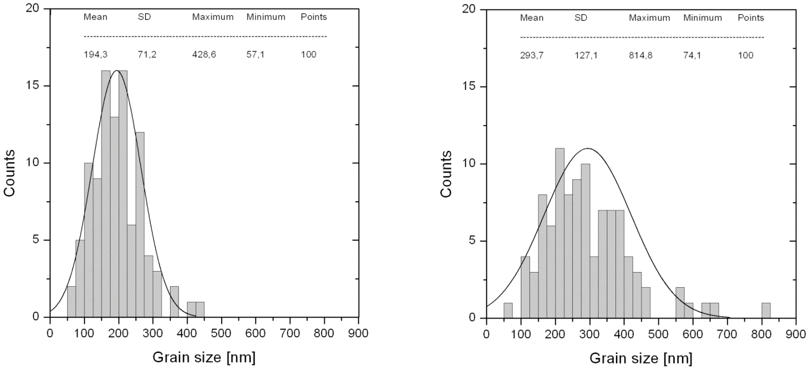

(a) (b)

Figure 3.16: Grain size histogram of (a) 2 µm PZT {100}-textured Zr/Ti gradient and (b) gradient free thin films.

Information about phase purity and texture are obtained by X–ray diffraction, using a 2-Theta scan from 20 to 50 degrees. The results are shown on Figure 3.17. The films are highly {100}-textured. Gradient and gradient free films are 99.3% and 98.4% {100}-oriented respectively.

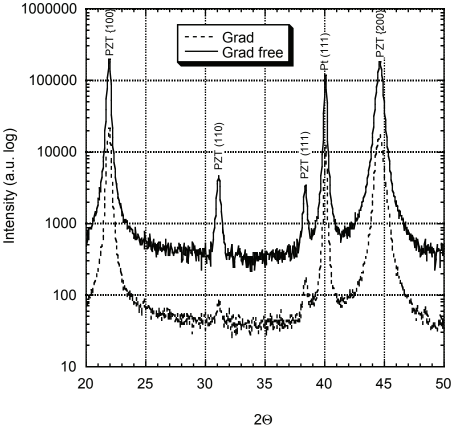

Figure 3.17: X-rax diffractogram of 2µm PZT {100}-textured Zr/Ti gradient and gradient free thin films.

3.3 FUNCTIONAL PROPERTIES

The effective dielectric constant $\varepsilon_{33,f}$ (theoretically in between fully clamped ε_{33}^{x} and free $\varepsilon_{33}^{\sigma}$), the loss factor tan δ and the admittance are measured with an impedance analyzer (Hewlett-Packard, HP-4194). The CV curves are performed with the same double-beam Mach–Zehnder interferometer used for the measurement of the $d_{33,f}$ coefficient (in the form of CV curves). Measurements are carried out at 5kHz with superimposed fixed Ac bias (0.1V) and varying DC electric field [20].

Ferroelectric properties (P-E loops) are obtained by measuring polarization hysteresis loops, with a set-up based on standard Sawyer-Tower circuits [21]. Triangular waveform of different amplitudes (from 0 to 400kV/cm) and a frequency of 250Hz are used. Two hysteresis loops are performed consecutively with a break of 1 second between each. Only the second hysteresis is measured. Different frequencies can be applied to control the stability of the films (1Hz to 1kHz). Coercive fields and remnant polarizations are extracted from these polarization loops.

The relevant coefficients of piezoelectric thin films are the effective values $d_{33,f}$ and $e_{31,f}$. Polycrystalline thin films exhibit a cylindrical symmetry where the polar axis is normal to the film plane, and the in-plane directions are equivalent. This symmetry is the same as of poled ceramics. Without loss of generality, one can reformulate the equations of state such that the free parameters are the in-plane strain (x_1, x_2) and the out-of-plane stress (σ_3). The direct effect then reads as follows [22]:

$$\begin{aligned}
D_3 &= e_{31,f}\left(x_1 + x_2\right) + d_{33,f}\sigma_3 + \varepsilon_{33,f}\varepsilon_0 E_3 \\
x_3 &= d_{33,f}E_3 - \frac{c_{13}^{E}}{c_{33}^{E}}\left(x_1 + x_2\right) + \frac{\sigma_3}{c_{33}^{E}} \\
\sigma_{1,2} &= -e_{31,f}E_3 + \left(c_{11}^{E} - \frac{\left(c_{13}^{E}\right)^2}{c_{33}^{E}}\right)x_{1,2} + \left(c_{12}^{E} - \frac{\left(c_{13}^{E}\right)^2}{c_{33}^{E}}\right)x_{2,1} + \frac{c_{13}^{E}}{c_{33}^{E}}\sigma_3
\end{aligned} \tag{3.10}$$

where $d_{33,f} = \dfrac{e_{33}}{c_{33}^{E}}$

and $\varepsilon_{33,f} = \varepsilon_{33}^{T} + \dfrac{d_{33,f}e_{33}}{\varepsilon_0}$

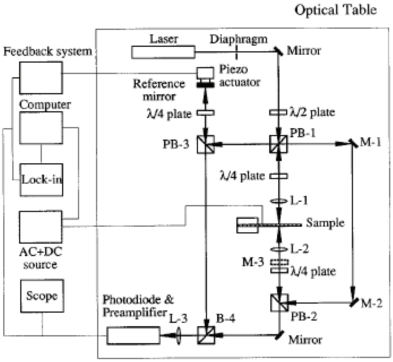

Figure 3.18: Schematic of the double beam interferometer [20].

The $d_{33,f}$ coefficient can directly be measured as x_3/E_3 provided that $x_1 = x_2 = \sigma_3 = 0$. This measurement has been done with a double-beam Mach–Zehnder interferometer (Figure 3.18) [20] that only measures the thickness change of a film clamped on a much thicker substrate (assuming $x_1 = x_2 = 0$) at $\sigma_3 = 0$. The main advantage on this set-up lies in the fact that the film expansion along the 3-axis (thickness variation) can be discriminated from the bimorph-like bending of the sample.

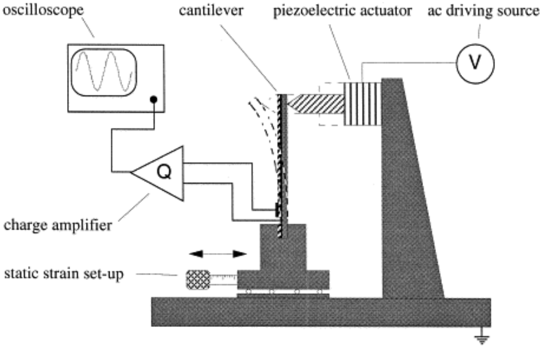

Figure 3.19: Schematic view of the $e_{31,f}$ transverse piezoelectric coefficient setup [23].

The measurement of the transverse piezoelectric coefficient $e_{31,f}$ has been realized by means of a cantilever bending method (Figure 3.19), collecting the charges as a function of x_1 and x_2 at zero σ_3 and electric field.

A small AC strain (varying from 0 to $-70\cdot10^{-6}$) is applied on the tip of the cantilever. A very well defined top electrode collects the charges created by the strained piezoelectric film. These charges are then converted to voltage by a charge amplifier and monitored on an oscilloscope. The effective transverse piezoelectric coefficient is calculated knowing the beam geometry, the clamping position and the beam deflection. Details about the sample preparation and the measurement technique have been described previously [23].

Finally, prior to any measurements, the samples of all compositions are hot poled at 150°C under 100kV/cm during 10 minutes and cooled down under field.

3.3.1 ELECTRICAL CHARACTERIZATION

DC bias dependent polarization and dielectric coefficient $\varepsilon_{33,f}$ are shown in Figure 3.20 and Figure 3.21. They confirm the high quality of the obtained films. A considerable improvement of properties is observed. The dielectric constant amounts to 1250 and 1620, for the gradient and the gradient free film respectively. These values are summarized in Table 3.1.

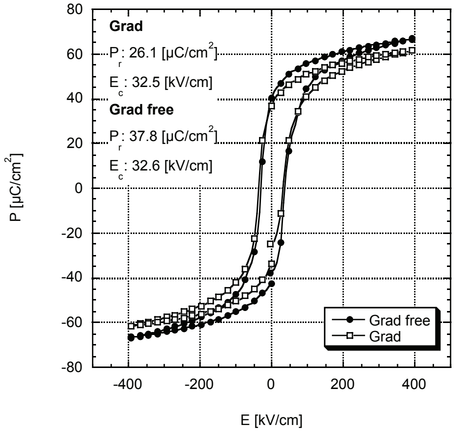

Figure 3.20: Ferroelectric loop of 2µm PZT with and without Zr/Ti gradient measured at a frequency of 250Hz.

Table 3.1: Summarized electrical characterizations of 2µm gradient and gradient free PZT films from Figure 3.20 and Figure 3.21.

		PZT 53/47	**PZT Grad free**
Remanent polarization P_r	[µC/cm^2]	26.1	37.8
Coercive field E_c	[kV/cm]	32.5	32.6
Relative dielectric constant $\varepsilon_{33,f}$	[-]	1250	1620
Dielectric loss tan δ	[%]	3.5	3.4

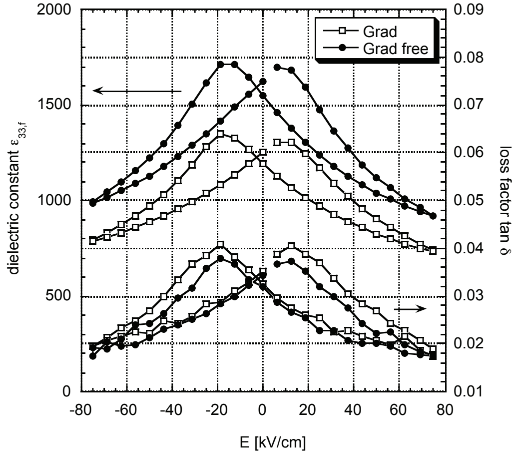

Figure 3.21: CV curve of 2 µm PZT with (Grad) and without (Grad free) Zr/Ti gradient. The dielectric constant is as 1620 and 1250 for gradient free and gradient PZT thin films at an electric field of 0 kV/cm respectively. The corresponding loss factor curves are in bottom of the graph. AC source: 0.1V at 5kHz.

By plotting the dielectric loss factor tan δ as a function of the dielectric constant for various electric fields (from the CV curve), the resultant curves give very interesting results following equation (3.11) (Figure 3.23). Both fitting curves (from grad and grad free films) cross the x-axis at the same point. This value (~280) can be considered as the intrinsic lattice dielectric constant $\varepsilon_{33,f}^{(i)}$ of the PZT.

$$\tan\delta = A\left(\varepsilon_{33,f} - \varepsilon_{33,f}^{(i)}\right) \tag{3.11}$$

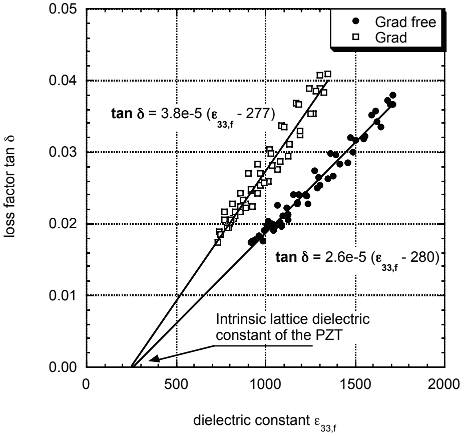

Figure 3.23: Dielectric loss factor tan δ as a function of the dielectric constant $\varepsilon_{33,f}$ at various electric fields (from the CV curve Figure 3.21) for gradient and gradient free PZT films. The two lines cross the x-axis at the same value (~280) corresponding to the intrinsic lattice dielectric constant $\varepsilon^{(i)}_{33,f}$ of the PZT.

It is known that by applying a DC electric field E, domains of larger product $\vec{P}\cdot\vec{E}$ grow at the extent of those with less favorable polarization directions. As a result, the domain wall density is becoming smaller. The small signal response, like the dielectric constant and loss in this case, are very much the result of reversible domain wall oscillations. As these walls diminish in number, the dielectric constant and loss diminish as well. This is in fact well demonstrated by Figure 3.21. In ferroelectrics, the dominant noise source is domain wall motions. At an electric DC field leading to a monocrystal situation (in our film, such a high field would lead to a break down), the dielectric constant reaches a small value equal to the lattice dielectric constant or even smaller (due to the field), expected to be in the range of 200 to 300. The dielectric losses will be very small, much less than 1%. The graph in Figure 3.23 shows that there is a linear relation ship between the loss tangent and the dielectric constant, if domain walls are removed by a DC electric field, or in other words, both are proportional to the domain wall density. At zero losses, the intrinsic dielectric constant should be obtained. This is indeed the case; even more, both materials yield the same intrinsic value. The different slopes can be interpreted in two different ways: either the domain wall density is larger for the gradient film, or the displacement of walls is more dissipative in the gradient film. For both postulations one can find arguments. Larger grains (as in the gradient free film) should exhibit a smaller domain wall density, and the inhomogeneous composition in gradient films could lead to more friction where domain walls hit the compositional limit where symmetry changes.

3.3.2 PIEZOELECTRIC PROPERTIES

The evolution of the transverse piezoelectric coefficient $e_{31,f}$ has been determined as a function of an applied AC and DC negative strain (from 0 to $-7\cdot10^{-5}$ peak-to-peak strain). The $e_{31,f}$ coefficient has been measured as well as a function of an applied DC bias. All measurements were done at a frequency of 110Hz.

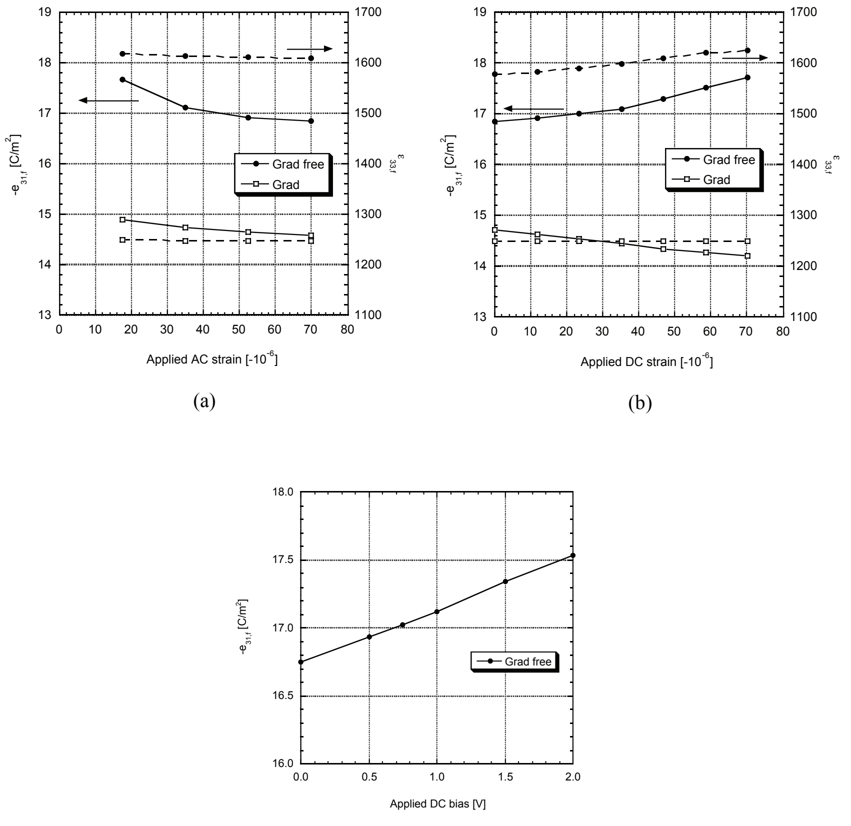

(a)

(b)

(c)

Figure 3.24: Effect of (a) applied AC strain, (b) applied DC strain and (c) applied DC bias on the transverse piezoelectric coefficient $e_{31,f}$ and the dielectric constant $\varepsilon_{33,f}$ measured at 110Hz of gradient and gradient free PZT films

Very high values of transverse piezoelectric coefficient $e_{31,f}$ have been achieved. An $e_{31,f}$ of -14.9 C/m^2 and -17.7 C/m^2 are measured for gradient and gradient free films respectively for low AC strain (Figure 3.24 (a)). A small decrease in the coefficient is observed with increasing applied AC strain (2.1% and 4.6% for gradient and gradient free films respectively). This effect is due to a lower mobility of the domain walls with increasing AC strain. Figure 3.24 (b) shows the effect of applied DC strain on the transverse $e_{31,f}$ coefficient. A decrease of 3.5% of the coefficient is observed with -$7 \cdot 10^{-5}$ applied DC strain on the gradient film. On the other hand, an enhancement of 3.5% of the coefficient is observed with the same applied DC strain on the gradient free film. By applying a DC bias on the film, the $e_{31,f}$ coefficient increases (Figure 3.24 (c)). This bias acts as a polling effect and thus reorients even better the dipoles present in the film. In some kind of way, the measurement of the transverse coefficient is done during poling, that is on a film with an applied electric filed helping every dipole to be parallel to the field. With a better polarization, the $e_{31,f}$ coefficient is higher.

In order to complete the description of piezoelectric properties, the longitudinal coefficient has been evaluated as well. A typical loop as obtained by measuring the small signal $d_{33,f}$ as a function of a superimposed DC electric field is given in Figure 3.25 for both grad and grad free films.

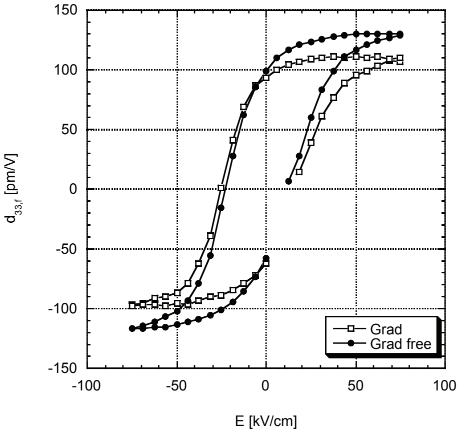

Figure 3.25: Clamped longitudinal piezoelectric coefficient $d_{33,f}$ as a function of DC electric field for both grad and grad free films. Measurement performed under the same conditions as in Figure 3.21 (AC source: 0.1V at 5kHz).

Formally, transverse and longitudinal coefficients are related to each other by the fully clamped e_{31} coefficient and the stiffness constant c_{31}^{E} relating in-plane strain to out-of-plane stress:

$$e_{31,f} = e_{31} - c_{13}^{E} \cdot d_{33,f} \tag{3.12}$$

In Figure 3.26, the results of the PZT using gradient film (standard solution 53/47 and sol-gel seed layer) and gradient free film (new solution and sol-gel seed layer) are summarized in a $d_{33,f}$ vs. $e_{31,f}$ plot and compared to literature data of PZT bulk ceramics (pure PZT ceramics from Berincourt [12]), sol-gel PZT (with sputtered seed layer from Ledermann [5]) and optimized doped ceramics, 3203 HD from Motorola [24]. The effort made to optimize the properties of sol-gel films clearly shows that a substantial enhancement has been obtained.

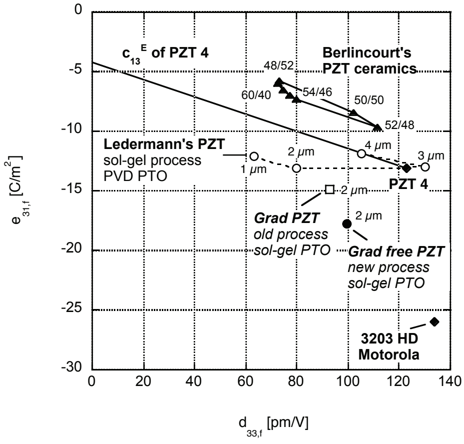

Figure 3.26: Comparison of 2µm {100}-textured PZT 53/47 using old process (Grad PZT) and new process (Grad free) and a sol-gel seed layer, with Berlincourt's PZT bulk ceramics [12], 1-4µm Ledermann's sol-gel PZT [5] and optimized PZT ceramic 3203 HD from Motorola [24].

It is interesting to note that increasing film thickness (above 1µm) in the gradient film lead to an increase in $d_{33,f}$ but not an increase of $e_{31,f}$. Relating that to the microstructure, we notice that an increase in thickness leads to an elongation of the grains along the thickness direction, but does not lead to an increase in grain diameter in case of the film with gradients. The grains of the next layer just nucleate on the previous grains and continue growth with about the same diameter. In the gradient-free film, however, grains become also wider. The top part of the film exhibits grains that are 50% larger than in the reference film. This must be ascribed to the much less abrupt - of even absent - change of the lattice parameters nucleating the perovskite on the previous PZT layer. In case of the gradient film, a Ti rich composition nucleates on a Zr rich film having different lattice parameters changing from tetragonal phase to rhombohedral phase. This leads to an increase on interface energy, and thus to smaller nuclei with island character. It appears that such conditions are less favorable for lateral growth of the grains. Larger grain diameters are expected to have an impact on domain size

Although no single crystal data for PZT allows the derivation of the theoretical properties of textured films, $e_{31,f}$ coefficient can be approximate using theoretical value of Haun [13, 15]. In his work, the electrostrictive coupling between the ferroelectric polarization and stress (Q_{ij}) and ferroelectric polarization (P_i) have been derived from poled bulk ceramics. The transverse piezoelectric coefficient $e_{31,f}$ of a c-domain clamped on a plane is derived from the standard Landau-Ginzburg-Devonshire [25] free energy as follows:

$$d_{31} = 2\varepsilon_0\varepsilon_{33}Q_{12}P_3 \tag{3.13}$$

And as

$$e_{31,f} = \frac{d_{31}}{s_{11}^E + s_{12}^E} \tag{1.3}$$

equation (3.13) becomes:

$$e_{31,f} = \frac{2\varepsilon_0\varepsilon_{33}Q_{12}P_3}{s_{11}^E + s_{12}^E} \tag{3.14}$$

where		
	d_{31}	: transverse piezoelectric coefficient [pm/V]
	ε_0	: absolute permittivity = $8.8542\cdot10^{-12}$ [C/Vm]
	ε_{33}	: lattice dielectric constant [-]
	Q_{12}	: electrostrictive coefficient [m^4/C^2]
	P_3	: c-domain ferroelectric poloarization [C/m^2]
	s_{11}^E, s_{12}^E	: elastic compliance of PZT [m^2/N]

Taking values for Q_{12}, P_3 and lattice dielectric constant ε_{33} from [15] and the elastic compliance coefficients from [26] for a PZT 50/50 tetragonal (001) c-domain, a $e_{31,f}$ value of -18.7 C/m^2 is calculated. Our experimental values of -17 to -17.7 C/m^2 agree very well with these best available data for PZT monocrystals.

A summary of the different measured and calculated dielectric and piezoelectric values of the gradient, gradient free and PZT 50/50 tetragonal (001) c-domain from Haun is presented in Table 3.2.

Table 3.2: Measured and calculated dielectric and piezoelectric values for different PZT.

	$e_{31,f}$ [C/m^2]	d_{31} [pm/V]	d_{33} [pm/V]	$d_{33,f}$ [pm/V]	$\varepsilon^{(i)}_{33,f}$ [-]	$\varepsilon_{33,f}$ [-]	ε^{T}_{33} [-]
Grad PZT	-14.9	-145	266	93	277 ^{1}	1250	1740 ^{2}
Grad free PZT	-17.7	-173	305	100	280 ^{1}	1620	2310 ^{2}
PZT 50/50 Haun [15]	-18.7	-156	327	169	300 (?)		

1. from Figure 3.23
2. from equation (1.5)

On Figure 3.26, it can be seen that the gradient and gradient free PZT film $e_{31,f}$ coefficients are superior to those derived from classical ceramics data (Berlincourt) and those from standard sol-gel PZT using sputtered seed layer (Ledermann). The improvement in the $e_{31,f}$ coefficient of the gradient film compare to Ledermann's sol-gel films is only due to a better {100}-texturing of the PZT layer (95% vs. 99.3% {100}-oriented).

However, there is still a large gap in $e_{31,f}$ between our films and an optimized ceramics like the 3203 HD from Motorola.

3.3.3 FIGURE OF MERIT

Piezoelectric coefficients describe directly achievable piezoelectric forces and charges. But not only these coefficients have to be considered for optimization of properties. Depending on applications, more complex figures of merits (FOM) have to be taken into account. Dielectric constant as well the dielectric loss contributes to signal-to-noise ratio and power efficiency.

In sensors, the obtained signal is proportional to the transverse piezoelectric coefficient $e_{31,f}$ while the dielectric noise current density is proportional to the dielectric loss tan δ. the signal-to-noise (S/N) figure of merit is thus defined by:

$$S/N\left[Pa^{0.5}\right] = \frac{|e_{31,f}|}{\sqrt{\varepsilon_0 \varepsilon_{33,f} \cdot \tan\delta}} \tag{3.15}$$

In actuators, the relevant coefficient is the coupling factor k^2, which quantifies the energy transfer from the electrical system to the mechanical system [27]. The coupling coefficient depends on the geometry and the material involved. It is usually approached by finite element modeling. However, in some simple cases, k^2 can be calculated analytically. For a thin clamped disk, used as stator in ultrasonic micromotors [28], the coupling coefficient and the power efficiency figures of merit are given by:

Material's coupling factor
$$(k_{p,f})^2 = \frac{2e_{31,f}^2}{\varepsilon_0 \varepsilon_{33,f}} \left(\frac{1-\nu}{Y}\right)_{Si} \tag{3.16}$$

Power efficiency
$$\frac{(k_{p,f})^2}{\tan\delta} = \frac{2e_{31,f}^2}{\varepsilon_0 \varepsilon_{33,f}} \left(\frac{1}{\tan\delta}\right)\left(\frac{1-\nu}{Y}\right)_{Si} \tag{3.17}$$

Table 3.3: Figures of merits of gradient free PZT, gradient PZT and standard 53/47 PZT.

FOM	Definition	PZT Grad free	PZT Grad	PZT 53/47 [5]
$\varepsilon_{33,f}$	-	1620	1250	935
tan δ	-	3.4	3.5	3.6
$-e_{31,f}$ [C/m^2]	-	17.7	14.9	12.1
Signal-to-noise ratio [Pa$^{0.5}$]	$\frac{\lvert e_{31,f}\rvert}{\sqrt{\varepsilon_0 \varepsilon_{33,f} \tan\delta}}$	2.4	2.2	2.1
Coupling factor	$\frac{2e_{31,f}^2}{\varepsilon_0 \varepsilon_{33,f}} \left(\frac{1-\nu}{Y}\right)_{Si}$	0.24	0.22	0.20
Power efficiency	$\frac{2e_{31,f}^2}{\varepsilon_0 \varepsilon_{33,f}} \left(\frac{1}{\tan\delta}\right)\left(\frac{1-\nu}{Y}\right)_{Si}$	7.1	6.3	5.5

In case of sol-gel {100}-textured PZT thin films, it turns out that constant Zr/Ti content with $PbTiO_3$ sol-gel seed layer is best in all cases. The FOM definition and measured values for gradient free PZT (PTO sol-gel seed), gradient PZT (PTO sol-gel seed) and standard 53/47 PZT (from [5]) are summarized in Table 3.3. For coupling coefficient and power efficiency, it was assumed that the PZT thin film is part of composite structure that contains primarily silicon (Young's modulus Y = 130MPa, Poisson's coefficient $\nu = 0.278$).

By using different Zr/Ti content solution, gradient free PZT films are fabricated and exhibit high $e_{31,f}$ values. Thus, this gradient free PZT is the best material for application in piezoelectric MEMS, in particular for transducers and actuators. The coupling factor is more than 10% higher than gradient PZT and 23% higher than PZT 53/47 using PVD seed layer.

3.4 SUMMARY

A sol-gel based $PbTiO_3$ seed layer was developed in order to improve sol-gel PZT thin films. The new seed layer yielded a larger {100}-texture (99.3% with 2 µm thick PZT film) and a better homogeneity on 100 mm wafers. In addition, its use greatly simplifies the deposition procedure as compared to the use of sputtered seed layers. The crystallization of the lead titanate occurs between 520° and 550°C. After seed layer anneal, a tensile stress appears in the platinum bottom electrode due to thermal misfit.

The crystallization of PZT on top of the new seed layer was studied. Perovskite nucleation sets in at 550 °C. In the bulk of the film, there are transient nanograins of oxygen deficient fluorites or pyrochlores. The (100) perovskite growth front moves from the bottom electrode to the top of the film, all grains growing with about the same speed.

A further improvement was realized by eliminating compositional variations in the solid solution. PZT thin films of homogeneous composition were synthesized by means of a modified sol-gel route on $Pt(111)/TiO_x/SiO_2/Si$ substrates. Compositional variations in sol-gel process films could be reduced from 40-70% Zr concentration to 50-55% Zr concentration. As a consequence, lateral grain diameters were increasing, as well as the dielectric constant and the transverse piezoelectric coefficient $e_{31,f}$. The improvement in properties can be a direct consequence of a more homogeneous composition, and thus reduced micro strains, or also an indirect consequence due to increase grain diameters. The relative dielectric constant $\varepsilon_{33,f}$ was measured as 1620, and the remnant transverse piezoelectric coefficient $e_{31,f}$

was measured as -17.7 C/m^2. This $e_{31,f}$ value of gradient free films comes close to the best available theoretical values of PZT 50/50 by combining results from Haun *et al* on d_{31} [15] and Jaffe *et al* for elastic constants [26] amounting -18.7 C/m^2.

3.5 REFERENCES

1. K.D. Budd, S.K. Dey and D.A. Payne, *Sol–gel processing of PT, PZ, PZT and PLZT thin films*, Br. Ceram. Proc., **36**, 107–121 (1985)
2. S.R. Gurkovich and J.B. Blum, *Preparation of monolithic lead-titanate by sol–gel process*, in: L.L.H.A.D.R. Ulrich (Ed.), Ultrastructure Processing of Ceramics, Glasses and Composites, Wiley/Interscience, New York, 152–160 (1984)
3. G. Orcel and L. Hench, *Effect of formamide additive on the chemistry of silica-gels. Part 1. NMR of silica hydrolysis*, J. Non-Cryst. Solids, **79**, 177–194 (1986)
4. S. Kalpat and K. Uchino, *Highly oriented PZT thin films: growth, control of texture, and its effect on dielectric properties*, J. Appl. Phys., **90**, 2703-2710 (2001)
5. N. Ledermann, P. Muralt, J. Baborowski, S. Gentil, K. Mukati, M. Cantoni, A. Seifert, and N. Setter, *{100}-textured, piezoelectric* $Pb(Zr_x,Ti_{1-x})O_3$ *thin films for MEMS: integration, deposition and properties*, Sensors and Actuators, **A 105**, 162-170 (2003)
6. T. Maeder, P. Muralt, M. Kohli, A. Kholkin and N. Setter, $Pb(Zr_x,Ti_{1-x})O_3$ *thin films by in-situ reactive sputtering on micromachined membranes for micromechanical applications*, British Ceramic Proceedings, **54**, 207-218 (1995)
7. C.K. Kwok and S.B. Desu, *Low-temperature perovskite formation of PZT thin films by a seeding process*, J. Mater. Res., **8**(2), 339-344 (1993)
8. G.B. Harris, *Quantitative measurements of preferred orientation in rolled uranium bars*, Philos. Mag., **43**, 113-123 (1952)
9. K.G. Brooks, I.A. Reaney, R. Klissurska, Y. Huang, L. Bursill, and N. Setter, *Orientation of rapid thermally annealed lead zirconate titanate thin films on (111) Pt substrates*, J. Mater. Res., **9**, 2540-2553 (1994)
10. Y.-M. Sung, G.M. Anilkumar and S.-J. Hwang, *Influence of nanoparticle seeding on the phase formation kinetics of sol-gel-derived* $Sr_{0.7}Bi_{2.4}Ta_2O_9$ *thin films,* J. Mater. Res., **18**(2), 387-395 (2003)

11. P. Muralt, M.-A. Dubois, A. Seifert, D.V. Taylor, N. Ledermann and S. Hiboux, *In-plane piezoelectric coefficient of PZT thin films as a function of composition*, Ferroelectrics, **224**, 235-242 (1999)

12. D.A. Berlincourt, C. Molik, and H. Jaffe, *Piezoelectric properties of polycrystalline PZT compositions, in Proceedings of the IRE*, Institute of Radio Engineers, New York (1960)

13. M.J. Haun, E. Furman, S.J. Jang, and L.E. Cross, *Thermodynamic theory of the lead zirconate-titanate solid solution system, part V: Theoretical calculations*, Ferroelectrics, **99**, 63-86 (1989)

14. K. Amanuma, T. Hase and Y. Miyasaka, *Crystallization behavior of sol-gel derived Pb(Zr,Ti)O3 thin fims and polarization switching effect on film microstructure*, Appl. Phys. Lett., **65**(24), 3140-3142 (1994)

15. M.J. Haun, Z.Q. Zhuang, E. Furman, S.J. Jang, and L.E. Cross, *Thermodynamic theory of the PZT solid solution system, Part III*, Ferroelectrics, **99**, 45-54 (1989)

16. Z. Huang, J. Battat, P.P. Donohue, M.A. Todd, and R.W. Whatmore, *On the phase transformation kinetics in lead scandium tantalate thin films*, J. Phys. D: Appl. Phys., **36**, 3039-3046 (2003)

17. A. Seifert, L. Sagalowicz, P. Muralt, and N. Setter, *Microstructural evolution of dense and porous (PbCa)TiO3 thin films for pyroelectric applications*, J. Mater. Res., **14**, 2012-2022 (1999)

18. P. Muralt, *Texture control and seeded nucleation of nanosize structures of ferroelectric thin films* , J. Appl. Phys., **100**, 051605 (2006)

19. Y.-M. Sung and W.-C. Kwak, *Fluorite-to-Aurivillius phase transformation kinetics in sol-gel derived SBT thin films*, Chemical Physics Letters, **411**, 389-394 (2005)

20. A.L. Kholkin, C. Wütrich, D.V. Taylor and N. Setter, *Interferometric measurements of electric field-induced displacements in piezoelectric thin films*, Rev. Sci. Instrum., **67**, 1935–1941 (1996)

21. C.B. Sawyer and C.H. Tower, *Rochelle salt as a dielectric*, Physical Review, **35**, 269-273 (1930)

22. P. Muralt, *Piezoelectric thin films for MEMS*, Integr. Ferroelectr., **17**, 297–307 (1997)

23. M.-A. Dubois and P. Muralt, *Measurement of the effective transverse piezoelectric coefficient $e_{31,f}$ of AlN and PZT thin films*, Sensors and Actuators, **A 77**, 106–112 (1999)

24. S. Sherrit, H.D. Wiederick, B.K. Mukherjee, *A complete characterization of the piezoelectric, dielectric and elastic properties of Motorola PZT 3203 HD including losses and dispersion*, Proc. SPIE 3037, 158–169 (1997)

25. M.J. Haun, E. Furman, S.J. Jang, and L.E. Cross, *Thermodynamic theory of the PZT solid solution system, Part I*, Ferroelectrics, **99**, 13-25 (1989)

26. B. Jaffe, W.R. Cook and H. Jaffe, *Piezoelectric Ceramics*, London: Academic Press (1971)

27. T. Ikeda, *Fundamentals of piezoelectricity*, Oxford: Oxford University Press (1990)

28. P. Muralt, M. Kohli, T. Maeder, A.L. Kholkin, K.G. Brooks, N. Setter and R. Luthier, *Fabrication and characterization of PZT thin film vibrators for micromotors*, Sensors and Actuators, **A 48**, 157–165 (1995)

4

FREE PZT THIN FILM CALOTTE MEMBRANES

4.1 INTRODUCTION

4.2 FABRICATION OPTIONS

4.3 PREPARATION OF MICROMOULD

4.4 CMP

4.5 SPRAY COATING PHOTORESIST

4.6 FILMS DEPOSITION & PATTERNING

4.7 LIBERATION OF MEMBRANE

4.8 CHARACTERIZATION & RESPONSE

4.9 SUMMARY

4.10 REFERENCES

4.1 INTRODUCTION

The standard fabrication method to obtain PZT coated plates or membranes is based on flat supporting layers made of stress compensate Si_3N_4/SiO_2 layers [1], stress free nitride layers [2], or crystalline silicon layers that are either the remaining silicon after deep etching [3], or the device wafer of a SOI (silicon on insulator) [4]. In this part, we try to go one step further, and investigate the possibility to establish curved membranes. The considered geometry is the one of a calotte, thus an area on a sphere, limited by a circle. Not used so frequently in English, the translation is given here: “cap”, meaning among other things *“the broad upper part of the fruiting body of most mushrooms and toadstools, at the top of a stem and bearing gills or pores”* (from Oxford American Dictionary). The aim is thus to fabricate free PZT membranes in calotte shape that could be used as resonator. As the height of the calotte exceeds the film thickness by many times, this work implies new thin film fabrication with a three dimensional sacrificial structure, or mould. With regard to performance, the calotte shape could partially remedy a disadvantage of flat plate structures: the useful force direction is usually perpendicular to the substrate plane. A planar thin film, however, produces its piezoelectric forces along the substrates plane, and the vertical dilatation of the film is a too small effect. It thus needs a mechanism to redirect the force, or the excursion. This is, for instance, realized by means of a long heterogeneous double layer cantilevers (length L), where the in-plane forces create a bending analogous to the bi-metal effect, which leads to an excursion of the cantilever tip proportional to L^2. In the callotte, there is at least a vertical component of the local in-plane stress or strain. The calotte shape could serve to focus acoustic emission, or concentrate reception of acoustic waves. In the audible range, such structure could be used as ear aid between 20 and 20 kHz (in sensor mode), at ultrasonic frequencies, new type of p-MUT's (piezoelectric Micromachined Ultrasonic Transducer) could be conceived.

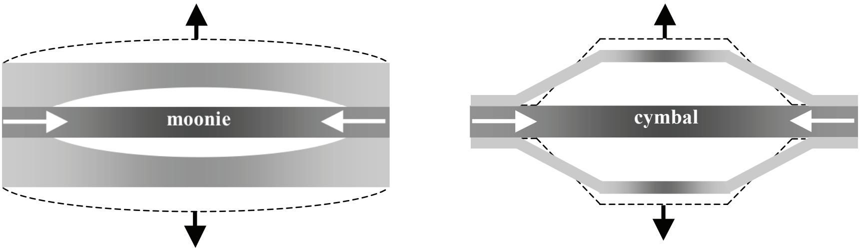

Figure 4.1: Moonie and Cymbal transducers.

In the world of bulk devices, there are known structures with improved redirection capabilities not needing the bending mechanism (which reduces coupling). They work on the basis of the so-called flex-tensional mechanism. Moonies [5, 6, 7, 8, 9] or cymbals [10, 11] as flex-tensional transducers consist of a piezoelectric disk sandwiched between two metal end-caps (Figure 4.1). The caps contain a shallow cavity on their inner surface. The cavities enable the caps to convert and amplify the small radial displacement of the disk into a much larger axial displacement normal to the surface of the caps. In the moonies, both the d_{31} (= d_{32}) and d_{33} coefficients of the piezoelectric ceramic contribute to the axial displacement of the composite. The shallow spaces under the endcaps produce a substantial increase in strain by combining the d_{33} and d_{31} coefficients of the ceramic. It is attractive for hydrophone, transceiver, and actuator applications, and is especially advantageous for use as a non-resonant low-frequency projector in deep water.

In the cymbal, the endcaps are fabricated by punching metal sheets. The cymbal design removes most of the region with stress concentration, and yields higher and more reproducible displacements. Even though this new design looks similar to the earlier moonie design, it has a different displacement mechanism. Displacement is primarily a result of flexural motion of moonie endcaps. For the cymbal, the displacement is created by the combination of the flexural and rotational motion of the endcaps.

Even if moonies and cymbals can be named as three-dimensional structures, they are made out of bulk disk of piezoelectric material. In order to integer 3D components into MEMS and IC technology, advanced or new processes of microfabrication have to be further developed or improved.

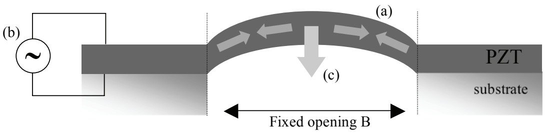

Figure 4.2: Schema showing the forces and displacements of the membrane under electric field.

The functioning of the new structure is explained in Figure 4.2. The transverse deformation in the PZT layer (a), describing a hemi-sphere, is transformed in a z movement (c) under electric field (b). The deformation only operates on the “fixed opening” part of the thin film (diameter base of the hemi sphere B). The film around the calotte is clamped onto the substrate and thus does not permit any movement of the PZT thin film. The diameter on the base stays constant while the length of the hemi-sphere of the calotte changes.

Without going too much into the detail, a simple calculation is done to evaluate the structure. Figure 4.3 shows a cut through the calotte. R is the curvature radius, B the base diameter of the calotte hemi-sphere, C the curvature of the calotte, h the height of the hemi-sphere regarding the base and φ the angle determining the length of the calotte C.

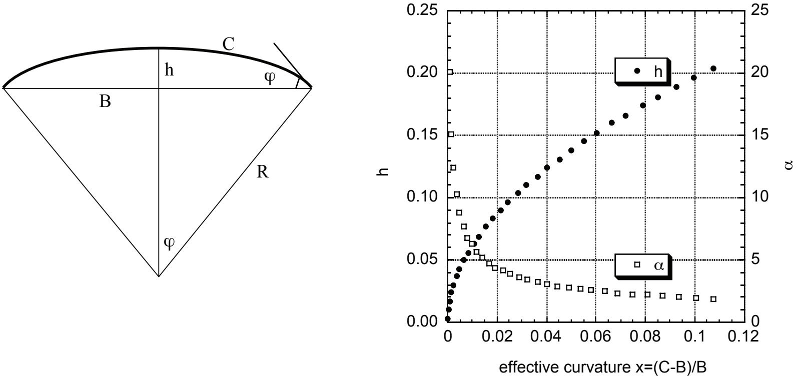

Figure 4.3: Schematic cut through the calotte with relevant parameters and graph of the height h and slope α as a function of the effective curvature x of the calotte.

The curvature C, the base diameter B and the height of the calotte h are equal respectively to:

$$C = 2R\varphi \tag{4.1}$$

$$B = 2R\sin\varphi = \mathrm{cst} \tag{4.2}$$

$$h = R\left(1 - \cos\varphi\right) \tag{4.3}$$

By plotting the height h of the calotte as a function of the effective curvature x $(= \frac{C - B}{B})$, we see that the slope α of this curve is very steep for small h and become smaller for bigger h (Figure 4.3). The calculation of the derivative of the height of the calotte by the applied voltage V is as follows:

$$\frac{\partial h}{\partial V} = \alpha \frac{\partial \varepsilon}{\partial V} = \alpha \frac{1}{B} \frac{\partial \mathrm{Capacitance}}{\partial V} = \alpha \frac{1}{B} d_{31} \tag{4.4}$$

We can see that we will have a large response for large α, that is for small h, i.e. for small angles φ.

In the converse mode, the calotte works as an actuator. The deformation of the membrane will drive a vertical displacement of the calotte allowing any wave propagation. In the direct mode, the calotte works as a sensor. A wave is propagated onto the device, which will cause a deformation of the thin film membrane. This deformation is transformed into electrical charges by the PZT layer and then measured. This study will focus on the microfabrication of the calotte for high frequency applications in the MHz region. Correspondingly, calotte diameter will vary from about 10 to 150 µm.

4.2 FABRICATION OPTIONS

There are varied possibilities to realize a calotte shape of a membrane. In the following, some of them will be explained and detailed with regard to advantages and disadvantages. Depending on the process convex, i.e. the structure goes above the silicon plane, or concave shape will be studied (Figure 4.4).

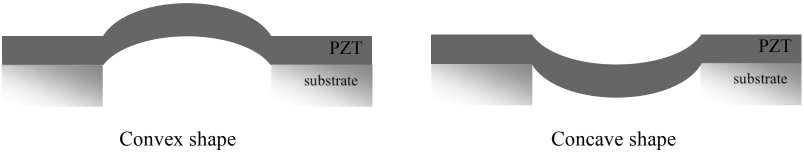

Figure 4.4: Convex and concave shape possibilities to realize the free-standing calotte membranes.

4.2.1 ROUTES TO CONVEX SHAPE

Convex shape requires the use of a predefine form, i.e. using a sacrificial feature tailored from sacrificial layer grown on top of the wafer plane. The sacrificial feature could be made of BPSG (Boron Phosphor Silicon Glass), Cupper or Nickel.

4.2.1.1 BPSG positive sacrificial layer

This doped silicon dioxide film is deposited by LPCVD (Low Pressure Chemical Vapor Deposition) at relatively low temperature (LTO: Low Temperature Oxide), patterned, and reflown in order to smoothen the edges. The latter can be performed at 700-900°C. The etching in BHF exhibits much higher rates than for thermally grown oxide.

The LTO silicon oxide is deposited by silane (SiH_4) with oxygen chemical reaction in the temperature range between 400°C and 450°C.

$$SiH_4 + O_2 \xrightarrow{425°C} SiO_2 + 2H_2 \tag{4.5}$$

The trimethylborate (TMB) and the phosphine (PH_3) are used for the BPSG deposition. These two compounds react with oxygen to give boron and phosphor oxide respectively which combine afterwards with the silicon atoms.

TMB: Tri-Methyl-Borate or $B(OCH_3)_3$

$$2B(OH_3)_3 + 9O_2 \longrightarrow B_2O_3 + 6CO_2 + 9H_2O \tag{4.6}$$

PH_3: Phosphine

$$4PH_3 + 5O_2 \longrightarrow 2P_2O_5 + 6H_2 \tag{4.7}$$

The boron and phosphor oxide combine with silicon oxide to form the BPSG (B_2O_3-P_2O_5-SiO_2).

Typical thicknesses used in microsystems applications are between 500 Å and 2µm. For thicker layers (4-5 µm), multiple deposits are required. The rate deposition is 6 to 9 nm per minute.

To achieve a calotte profile, quite a number of steps are needed:

- 10 hours of deposition for a BPSG layer of 5 µm high (maximum),
- a structuration of cylinders into the deposited layer,
- a reflow of the BPSG cylinders between 700 and 900°C under certain atmosphere [12, 13, 14].

This route was not pursued because it is too limiting in feature height.

4.2.1.2 Electrodeposition of Cupper and Nickel

Another possibility is to use Cu or Ni electroless or electrodeposited calotte grown on a structured conductive layer. The deposition quality (hardness, surface state, internal stress…) depends on a lot of parameters such as bath chemical composition, pH, temperature, currant density, and agitation. The so obtained hemi-sphere can have the sizes needed for the calotte fabrication. The major problem, using electroless or electrodeposited bumps of Cu or Ni, is the microelectronic material compatibility. Effectively, Cu and Ni are not CVD compatible material and can cause oven contamination problems. Furthermore, the chemical solutions (HNO_3 or ammonium persulphate for Cu and HCl or HF for Ni) needed to dissolve these Cu or Ni bumps sacrificial layers, are extremely corrosive for the final device (Ti, TiO_2, Pt and PZT). Moreover, additional barrier layers would be needed to prevent chemical reactions (oxidation and alloying) when depositing PZT on top of Cu or Ni.

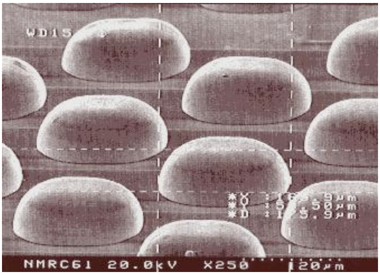

Figure 4.5: Electroless Ni bumps (58µm high deposited at 20µm/hr) on an Al substrate deposited from a proprietary NMRC Ni bath [15].

4.2.2 ROUTES TO CONCAVE SHAPE

A concave shape can be fabricated using a sacrificial layer or a micromould directly made in the substrate by any etching methods. Three different possibilities will be presented.

4.2.2.1 Concave shape with silicon dioxide sacrificial layer

First, a cylinder with required diameter has to be etched in a silicon substrate by RIE (Reactive Ion Etching). Once the cylinder is etched away, a wet oxide or LTO (see section 4.2.1.1) has to be deposited on the silicon substrate (the hole has to be "over-filled"). Then the oxide is polished by CMP process (Chemical Mechanical Polishing, see section 4.4) till reaching the surface of the hole, i.e. the surface of the silicon wafer. As the SiO_2 is softer than the silicon, it will be more polished and will consecutively form a concave calotte as shown on Figure 4.6.

Figure 4.6: Concave calotte membrane formed by CMP with sacrificial layer.

However it is difficult to well reproduce size and shape of the calotte because the filling of the depressions with slurry varies from hole to hole. This process cannot give reproducible results.

4.2.2.2 Concave calotte with anisotropic wet etching of silicon

A boat shape cavity is structured into the silicon substrate by wet anisotropic etching using a KOH solution (Figure 4.7). Diameter and depth can be easily achieved, however no spherical shapes are possible. In addition etching of KOH is always time-consuming.

Figure 4.7: Concave calotte shape structured by KOH wet etching.

4.2.2.3 Round shaped concave calotte with isotropic etching of silicon

The cavity is produced into the silicon substrate by dry or wet isotropic etching. This way of fabricating the required shape is probably the easiest one and was the first to be tested.

By dry etching

A silicon dioxide mask is micro-structured with the wanted size (reckoning under-etch effect) and then used to etch the silicon. C_2F_6 gas is used in an Alcatel 601 E to prepare the SiO_2 mask deposited by wet oxidation (650nm). For the silicon isotropic etching, SF_6 gas is used. The final structure gives the desired calotte form (Figure 4.8) except for an under-etched attack angle of over 90° (Figure 4.9). Knowing that other layers will be deposited on the calotte, shadowing problems will occur and discontinuities in films will appear. This angle can be softened using CMP on the whole substrate.

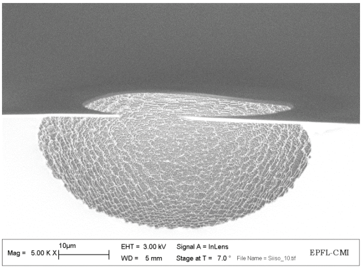

Figure 4.8: Silicon cavity obtained by dry isotropic SF_6 etching with SiO_2 mask.

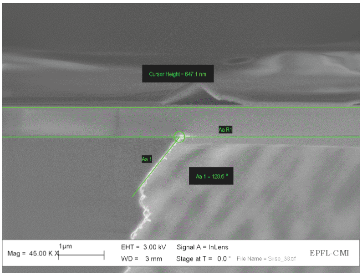

Figure 4.9: Under-etched angle of over 90°.

Moreover, a bad surface state is obtained as shown on Figure 4.10. A multitude of 300 nm peaks are observed. Growing a thick wet oxide or immerging the substrate into TMAH can remove this undesirable bad effect.

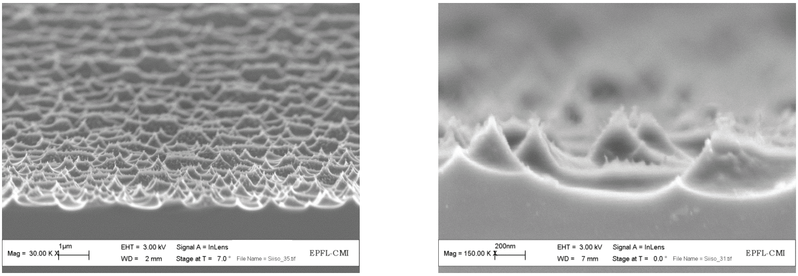

Figure 4.10: Silicon surface state after dry isotropic SF_6 etching.

Before attempting to optimize this process, wet isotropic etching was evaluated.

By wet etching

A solution of HF, HNO_3 diluted in H_2O or CH_3COOH is used (HNA) [16]. This method seems to give a better surface state as well as under-etched angle smaller than 90° (Figure 4.11). This process has been maintained for our study.

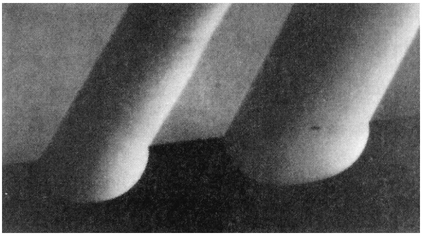

Figure 4.11: Wet silicon isotropic etching with HNA solution [17].

4.3 PREPARATION OF MICROMOULD

HNA system is a mixture of Hydrofluoric acid (HF) and Nitric acid (HNO_3). Water can be used as diluent, but acetic acid is preferred because it better prevents the dissociation of the nitric acid and so preserves the oxidizing power of HNO_3, which depends on the non-dissociated nitric acid species for a wide range of dilution [18].

The overall reaction is:

$$\mathrm{Si} + \mathrm{HNO_3} + 6\mathrm{HF} \longrightarrow \mathrm{H_2SiF_6} + \mathrm{HNO_2} + \mathrm{H_2O} + \mathrm{H_2} \tag{4.8}$$

The etching occurs via a redox reaction followed by dissolution of the oxide by an acid (HF) that acts as a complexing agent. Points on the silicon surface randomly become oxidation or reduction sites. These act like localized electrochemical cells, sustaining corrosion current of about 100 A/cm^2 (which is relatively large). Each point on the surface becomes both an anode and cathode site over time. If the time spent on each is the same, the etching will be uniform; otherwise selective etching will occur.

Silicon is promoted to a higher oxidation state at an anodic site which supplies positive charge in the form of holes:

$$Si + 2h^{+} \longrightarrow Si^{2+} \tag{4.9}$$

NO_2 from the nitric acid is simultaneously reduced at a cathode site which produces free holes:

$$2NO_2 \longrightarrow 2NO_2^{-} + 2h^{+} \tag{4.10}$$

The Si^{2+} combines with OH^{-} to form SiO_2:

$$Si^{2+} + 2OH^{-} \longrightarrow Si(OH)_2 \longrightarrow SiO_2 + H_2O \tag{4.11}$$

The SiO_2 is then dissolved by HF to form a water soluble complex of H_2SiF_6:

$$SiO_2 + 6HF \longrightarrow H_2SiF_6 + 2H_2O \tag{4.12}$$

The nitric acid has a complex behavior. The normal dissociation in water is (deprotonation):

$$HNO_3 \longleftrightarrow NO_3^{-} + H^{+} \tag{4.13}$$

An autocatalytic cycle for the production of holes and HNO_2 takes place:

$$HNO_2 + HNO_3 \longrightarrow N_2O_4 + H_2O \tag{4.14}$$

$$N_2O_4 \longleftrightarrow 2NO_2 \longleftrightarrow 2NO_2^{-} + h^{+} \tag{4.15}$$

$$2NO_2^{-} + 2H^{+} \longleftrightarrow 2HNO_2 \tag{4.16}$$

NO_2 is effectively the oxidizer of Si. Its reduction supplies holes for the oxidation of the Si. HNO_2 is regenerated by the reaction (autocatalytic). The oxidizing power of the etching solution is set by the amount of undissociated HNO_3.

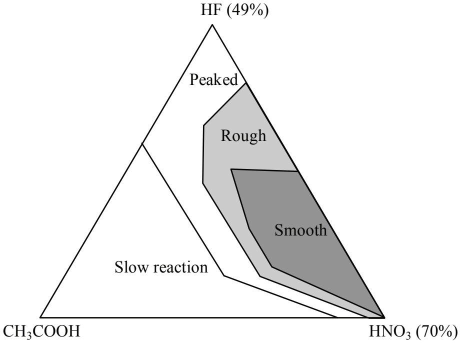

Figure 4.12: Resultant geometry of the etched die as a function of the etchant composition in the HNA system [16].

At high HF and low HNO_3 concentrations, etching tends to be difficult to initiate and exhibits an uncertain induction period. In addition, it results in relatively unstable silicon surfaces proceeding to slowly grow a layer of SiO_2 over a period of time. The etch rate is limited by the oxidation rate, so that the etching speed tends to be orientation dependent and affected by dopant concentration, defects and catalysts (sodium nitrate often is used). At low HF and High HNO_3 concentrations, the etch rate is controlled by the ability of HF to remove SiO_2 as it is formed. Etches in this regime are isotropic and truly polishing, producing a bright surface with anisotropies of 1% or less (favoring the <110> direction) when used on <100> wafers [19]. The Figure 4.12 summarizes how the topology of the Si surfaces depends strongly on the composition of the etch solution. Around the maximum etch rates the surfaces appear quite flat with rounded edges, and very slow etching solutions lead to rough surfaces.

To test the etching power of HNA system, substrates are prepared with holes, that are structured in a wet oxided (650 nm) silicon wafer by means of photolithography. No stripping of photoresist is performed after SiO_2 etching. The first tested solution used (Solution #1) was diluted in water with composition ratio of 16:16:1 (HF:HNO_3:H_2O). It was extremely reactive. This solution etches the Si substrate 40 µm in 5 seconds. The resultant etching is shown on Figure 4.13. During the reaction, deep red smoke escapes from the solution (HNO_2) accompanied with evaporation of H_2 bubbles (Figure 4.14). The etch rate is more than 480 µm/min. A part of the reactive character of the solution, the surface state is nearly perfect (Figure 4.15) and the under etch angle is slightly smaller than 90°C (Figure 4.16). The remaining photoresist is dissolved during the process. As the first solution seems to be too much reactive, another mixture has been tried (Solution #2). The solution #1 has been half diluted with water (1:1:2). The result geometry is not satisfying as shown on Figure 4.17. This process took place in the limiting region between rough and smooth surface (Figure 4.12) and is not yet yielding sufficiently smooth surface. In addition this HF-rich solution too quickly removes resist and oxide films used as mask.

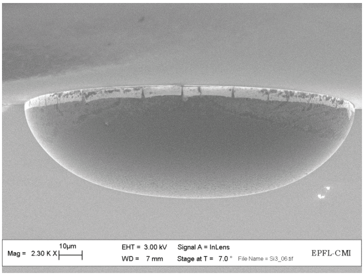

Figure 4.13: Silicon cavity done by wet isotropic HNA etching.

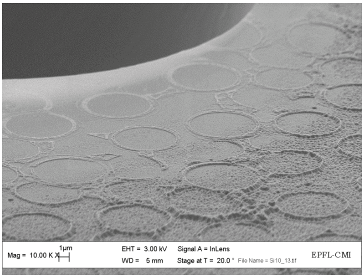

Figure 4.14: Effect of H_2 bubbles formation on the etching.

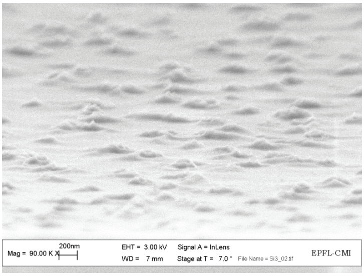

Figure 4.15: Surface state at the bottom of the cavity after HNA wet etching.

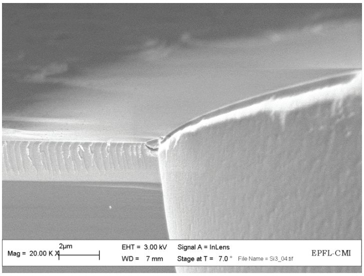

Figure 4.16: Under etch angle slightly smaller than 90°.

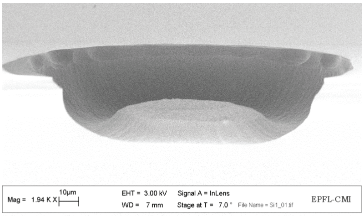

Figure 4.17: HNA Si etching with composition (1:1:2).

New tests are thus performed with acetic acid (CH_3COOH) as diluent instead of water. A third solution (Solution #3) was prepared as follows: 23%Vol HF, 72%Vol HNO_3 and 5%Vol CH_3COOH (composition ~2:7:1). This one gives excellent results (Figure 4.18). The etching is less reactive than Solution #1. A ring of SiO_2, used as mask, is still visible. The etch rate of the latter is 230 nm/min. Normal etch time is 2.5 minutes to achieve the right dimensions of the calotte. The etch rates of silicon for large opening (disks of 80 µm in diameter) are 10 µm/min laterally and 15 µm/min vertically. For small opening (disks of 10 µm in diameter), the etch rate is 7.5 µm/min laterally and vertically. Surface state is perfect for our application as shown on Figure 4.19. The remaining photoresist is dissolved during the process.

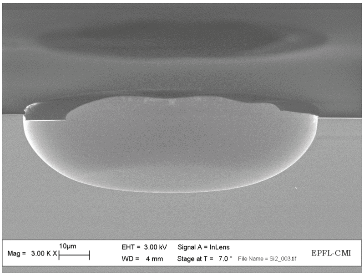

Figure 4.18: Silicon wet etching with (2:7:1) HNA solution.

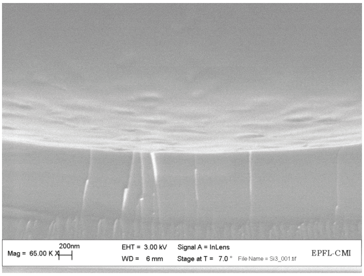

Figure 4.19: Surface state after (2:7:1) HNA solution etching.

A last solution (Solution #4) has been tested adding a little bit of NH_4F in Solution #3 to avoid dissolution of the photoresist. Effectively, ammonium fluoride (NH_4F) is added in HF to form BHF (Buffered HF) used to etch the silicon dioxide without dissolving the photoresist. This solution doesn't give better results. Even if the resist stay longer on the sample, the etching of the substrate takes more time and is less homogeneous.

Table 4.1 summarizes the different solution prepared with the composition ratio of each constituent being hydrofluoric acid (HF), nitric acid (HNO_3), water, acetic acid (CH_3COOH) and ammonium fluoride (NH_4F).

Table 4.1: Summary of the different used HNA solutions with composition ratio.

Solution #	**HF (49%)**	**HNO_3 (69%)**	**H_2O**	**CH_3COOH**	**NH_4F**	**surface state**
1	16	16	1			Rough / very reactive
2	1	1	2			Rough / long
3	2	7		1		Smooth
4	2	7		1	1	Less homogeneous / long

After micromould etching, the remaining silicon wet oxide is removed with BHF. The substrate is now ready for the next step, i.e. Chemical Mechanical Polishing (CMP).

4.4 CMP

CMP (Chemical Mechanical Polishing) is used to control the angle on top of the calotte that should be small. In general terms, CMP removes material from uneven topography on a wafer surface until a flat (planarized) surface is created. This allows subsequent photolithography to take place with greater accuracy, and enables film layers to be built up with minimal height variations. CMP combines the chemical removal effect of an acidic or basic fluid solution with the "mechanical" effect provided by polishing with an abrasive material. The CMP system usually has a polishing "head" that presses the rotating wafer against a flexible pad. A wet chemical slurry containing a micro-abrasive is placed between the wafer and pad. In the present case (for silicon polishing), the slurry contains diluted water with Na^+OH^- groups and silica particles of around 80 nm in diameter (from 20 to 80 nm with majority of 80). The concentrated basic solution has a pH at around 11 and, after dilution, a pH of about 9. The Na^+OH^- groups are used to stabilize the solution.

After polishing the substrate, it has to be cleaned in BHF in order to get rid of any remaining silica particles that agglomerate into the cavities.

4.5 SPRAY COATING PHOTORESIST

Uneven surfaces constitute a special challenge to photolithography. Simple spin coating of such surfaces leads to irregular coverage overcome by spray coating. PVD processes will be used to deposit the successive layers and patterned by spray-coated photoresist.

The direct spray coating is performed in an EVG 150 system. Compared to spin coating, spray coating operates on a different principle and it doesn't suffer from the resist thickness variation caused by the centrifugal force. The direct spray system includes an ultrasonic spray nozzle, which generates a distribution of droplets of micrometer size. It can reduce the effect of fluid dynamics of photoresist on the wafer as the resist droplets are supposed to stay where they are being deposited. The central part of the aerosol is forwarded to the dispense nozzle which is constructed to reduce the carrier gas pressure and to redirect the resist spray perpendicular to the substrate surface. During spray coating, the wafer is rotated slowly while the swivel arm of the spray coating unit is moved across the wafer. The low spinner speed (30-60rpm) is to minimize the centrifugal force. The rotating also allows resist coverage in all the angle of the cavities.

To get the proper droplet size distribution of photoresist, a resist solution with viscosity of less than 20cSt (centistokes = 10^{-6} m^2/s) is necessary. Photoresist AZ9260 (Clarient) diluted with a solvent is used for this spray system as it results in good coverage and uniform layer. Lower viscosity solutions can form a smoother layer but it may flow easier into high aspect ratio features and therefore can cause a resist thickness variation at top and bottom of cavities. The choice of the photoresist composition, i.e. the amount of solvent included and the solution viscosity, is very important. Although dedicated spray resist coating equipment is commercially available (EVG 150 system), the spray technology is not as developed as spin coating and specific resist solutions are still under development.

Advantages

For coating non-planar surfaces, spray coating presents some advantages over spin method. First, this technique uses much less resist than spin coating. The spray process requires no spin off photoresist so that it can effect up to 70% less resist consumption compared to spin process. Secondly, the reproducibility of spray coating is much better than spin coating. The resist thickness is repeatable over all cavities with the same size, regardless the position of cavities on the wafer. Spray coating has no thickness variation caused by directional effect of spinning. Thirdly, the direct spray coating doesn't require a special underlayer and can be applied on both insulating and conductive layers.

Disadvantages

Although the spray technique gives better results than spinning, variations in resist thickness are observed if cavities with a large difference in size are present on the same wafer. The resist thickness at the bottom of a small cavity is thicker that the one in a large cavity. If the difference in dimension of cavities is large, it will lead to a large variation in resist thickness between cavities. Consequently, this may affect the resolution of printed patterns in the photoresist when using the same exposure energy on the wafer. Hence, it will be easier to control the patterning process if the dimensions of cavities on the same wafer are comparable. Another challenge is the flowing of photoresist due to its gravity, resulting in a thicker resist layer at the bottom corner and a thinner one at the top corner of the same cavity. This flow effect will be of great influence for patterns that run in and across cavities. A solution to this problem is the use of a higher dose of exposure energy to remove excess photoresist at the bottom corner of the cavity. At the top corner the resist tends to be thinner due to surface tension at sharp corner. Sometime this will results in very poor coverage of photoresist at the top corner.

Spray coating can be used at all stages of the process and gives quite encouraging results, especially for patterning structures at the bottom of deep cavities. CMP turns out to be also useful for photolithography. CMP softens the angle of the calotte for further microfabrication. Indeed, spray coated photoresist will cover the structure, but for vertical walls (edge of the calotte) it is nearly impossible. On this specific region, if vertical walls are present, the resist will flow down the cavity, leaving the edge uncovered (Figure 4.20).

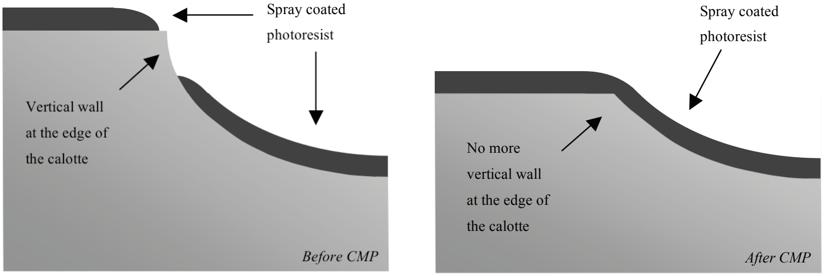

Figure 4.20: Spray coated photoresist on the edge of the calotte before and after CMP process.

4.6 FILMS DEPOSITION & PATTERNING

The device to be demonstrated requires many steps of microfabrication, such as bottom and top electrode deposition and patterning, PZT sputtering and etching as well as silicon bulk micromaching. All the fabrication steps will be presented in the following. A summarized process flow with cross section is shown in section 4.7.1.

4.6.1 SiO_2, WET OXIDATION

The first layer being deposited after micromould preparation (Si isotropic etching and CMP) is SiO_2. The 500 nm wet oxidation of the substrate is performed in a Centrotherm oven under water vapor flux at 1050°C. The oxide grows as:

$$\mathrm{Si} + 2\mathrm{H_2O} \xrightarrow{1050°\mathrm{C}} \mathrm{SiO_2} + 2\mathrm{H_2} \tag{4.17}$$

The substrate is now ready for further PVD deposition of bottom electrode, piezoelectric PZT layer and top electrode and subsequent patterning.

4.6.2 BOTTOM ELECTRODE

Further platinum bottom electrode with TiO_2/Ti (30/5 nm) barrier and adhesion layers are deposited using a sputter tool BAS 450 (Balzers) at 300°C. The 100 nm platinum layer is fully crystallized and {111}-oriented. The Pt layer is than patterned using spray coated photoresist (diluted AZ9260 from Clariant). This step is done to etch the Pt under top electrode guideline and contact to avoid parasitic capacitance. The etching is performed by dry etching using a RIE/ICP (Reactive Ion Etching with Inductively Coupled Plasma) reactor from STS. Chlorine gas is used to etch the platinum with a selectivity of 1/8 regarding the photoresist. The etching rate is about 35 nm/min. The spray coated photoresist mask is stripped in Shipley Remover 1165 at 70°C followed by microwave plasma aching in oxygen.

4.6.3 PIEZOELECTRIC PZT DEPOSITION

The deposition method that is employed for the PZT thin film synthesis is based on in-plane magnetron reactive in-situ sputtering of multiple metallic targets. The machine is a Nordiko 2000

(Nordiko Ltd, Havants, Hants, UK), equipped with 4 targets (Figure 4.21). The substrate-holder can be heated by quartz lamps and can either move on any targets or continuously rotate at a given speed. This allows in-situ deposition, static deposition for multilayers and dynamic deposition with a mixture of the different sources. Argon, oxygen, nitrogen gases, or a mixture of them can be used for the plasma discharge with a given flow and pressure controlled by a baratron gauge. High vacuum is achieved by means of turbomolecular pump backed up with rotary pump. Ni replaces the Inconel substrate-holder in order to achieve excellent temperature homogeneity on the whole surface (4 inch).

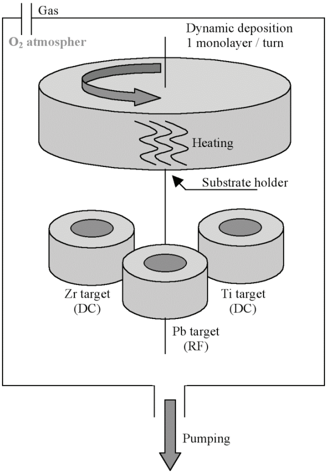

Figure 4.21: Schematic representation of the in-plane multi-target sputtering equipment.

For the PVD PZT thin film deposition, 3 metallic targets of Pb, Zr and Ti are reactively sputtered in O_2 in order to form the PbO, ZrO_2 and TiO_2 corresponding oxides, respectively. The substrate-holder rotates continuously at 6 rpm on the 3 targets and allows the mixture of the 3 oxides. The perovskite structure of PZT is formed in-situ, as the substrate holder being heated to 570-590 °C during deposition. The speed rotation corresponds to about 1 monolayer per turn of the substrate. One of the great advantages of this deposition configuration is the flexibility in the control of the stoechiometry (Zr/Ti ratio). Details in PZT thin film deposition condition are given in reference [20]. The main disadvantage of this deposition method is an in-homogeneity in the thickness and texture index and, consequently, in the properties on 4 inch wafers.

First, a seed layer of $PbTiO_3$ is sputtered for 3 minutes and 20 seconds corresponding to a thickness of about 15 nm. The deposition time for the PZT is 333 minutes, which correspond to 1 µm thick on a planar substrate. Figure 4.22 shows the calotte with the deposition of PZT. The layer is then patterned with spray-coated photoresist. Wet etching of PZT is done to reach the bottom electrode contact.

This etching is a critical topic in piezoelectric MEMS microfabrication. Despite the fact it is usually avoided because of the lack of etch control and photoresist undercut, the wet etching of PZT films remains a very versatile, fast and cheap method to open large areas (bigger than 50 x 50 μm^2) like vias. Because of high concentrations of hydrofluoric acid (HF), most of etch recipes are not selective to SiO_2 and to the TiO_2 adhesion/barrier layer of the platinum bottom electrode. Delamination of the structure can occur. In term of etching rate, HCL solutions are found to be very effective and selective etchants [21]. The used solution is a mixture of 30 ml of concentrated HCL (47%), 70 ml of water and 5 drops of HF. The etching rate is about 2 µm/min at 50°C. The etching is normally done in several time (3-4) to avoid too much under-etch.

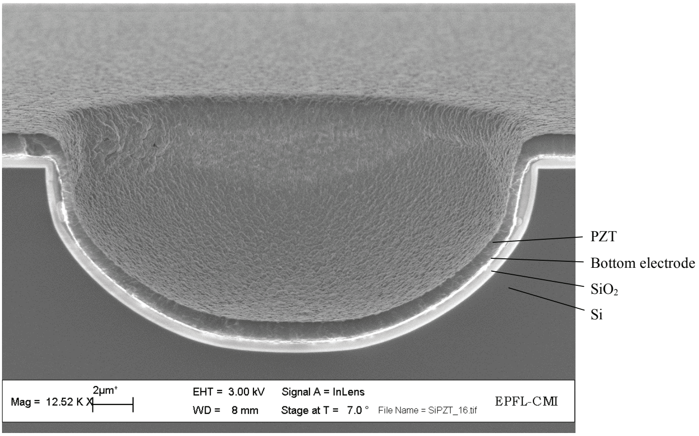

Figure 4.22: Calotte with Si, SiO_2, bottom electrode and PZT without CMP.

4.6.4 GROWTH OF PZT SPUTTERED FILM ON NON-FLAT SURFACES

Sputtered films are obtained from an atom or molecule flux that is quite diffuse, having the maximal arrival rate nevertheless in direction of the source (see Figure 4.23 a). Geometries are usually optimized for achieving uniform films on flat surfaces. When making coatings in holes or recessions, as required in this work, substantial changes in thickness distribution, chemical composition, and grain structure can be expected due to oblique incidence (Figure 4.23 b) and shadowing effects. Although first described 30 years ago [22], the details of all the consequences are not yet well described, and depend much on the materials system, and on the deposition temperature.

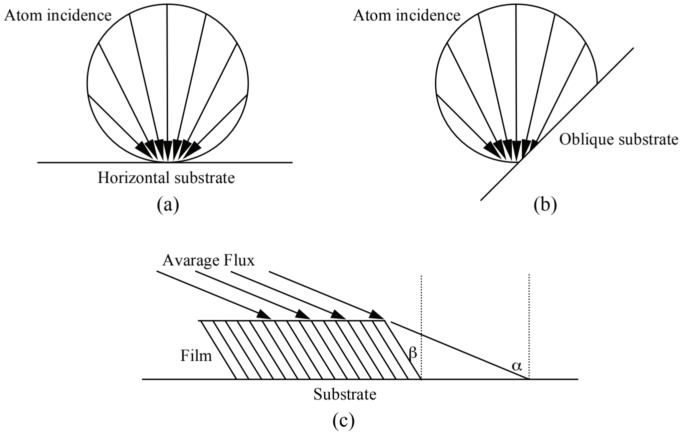

Figure 4.23: Atom incidence of a sputtered film on (a) horizontal and (b) oblique substrates. (c) deposition geometry of a sputtered film according to Nieuwenhuizen with an angle α formed by the source direction and the substrate normal [22].

According to Nieuwenhuizen [22] (Figure 4.23 c), the columnar grains should grow into the so-called tangent rule expressed by empirical equation (4.18). The angle β between the columns and the substrate normal is universally observed to be somewhat less than the angle α, formed by the source direction and substrate normal (Figure 4.23 b).

$$\tan\alpha = 2\tan\beta \tag{4.18}$$

In the present case, the sputtered PZT grains grow normal to the bottom electrode even on vertical wall, which is parallel to the sputtered flux (Figure 4.24). This growth property seems to be astonishing for a sputter process, but is explained by the large mobility of the ad-atoms at the growth temperature of 570°C. It follows more the way of growing as CVD film where the reactants are absorbed on the heated substrate surface and the ad-atoms undergo migration and film-forming reactions. Then a surface diffusion takes place, followed by nucleation and finally growth of the film. Atoms are finally chemisorbed at the site by surface diffusion, and not directly from the vapor. The effect of ion bombardment is slightly observed at the edges, where material is rather etched away, than added by an oblique flux. Physical removal by sputtering is indeed maximal at an angle of about 50° inclination of the surface.

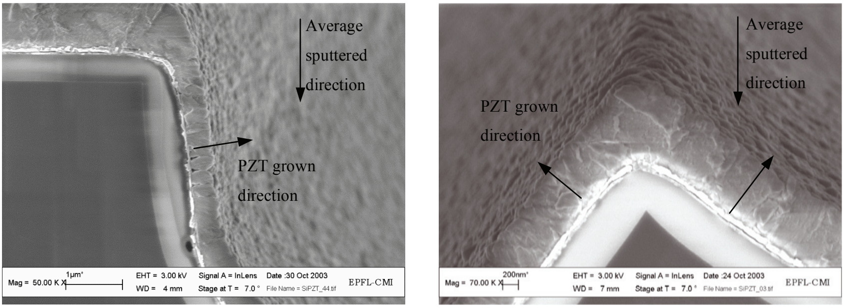

Figure 4.24: SEM micrographs of perpendicular growing of PZT even on surface nearly perpendicular to the PVD bombardment direction.

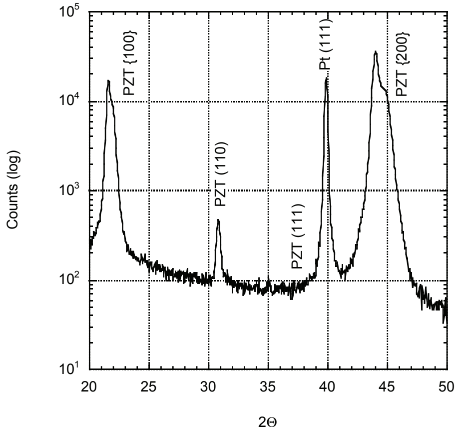

Figure 4.25: X-ray diffraction pattern of sputtered PZT film showing {100}- and {200}-preferred orientations.

The question is whether the crystalline planes are in the same direction as the grain grown direction. The X-ray diffraction pattern shows a {100}-preferred orientation of the 45/55 PZT sputtered film (Figure 4.25). To be sure that all grains grow in the {100} direction, diffraction diagrams with TEM facilities are made on the PZT layer from the top side, where the sputtered flux is perpendicular to the substrate, and along the slope, where the sputtered flux is parallel to the substrate.

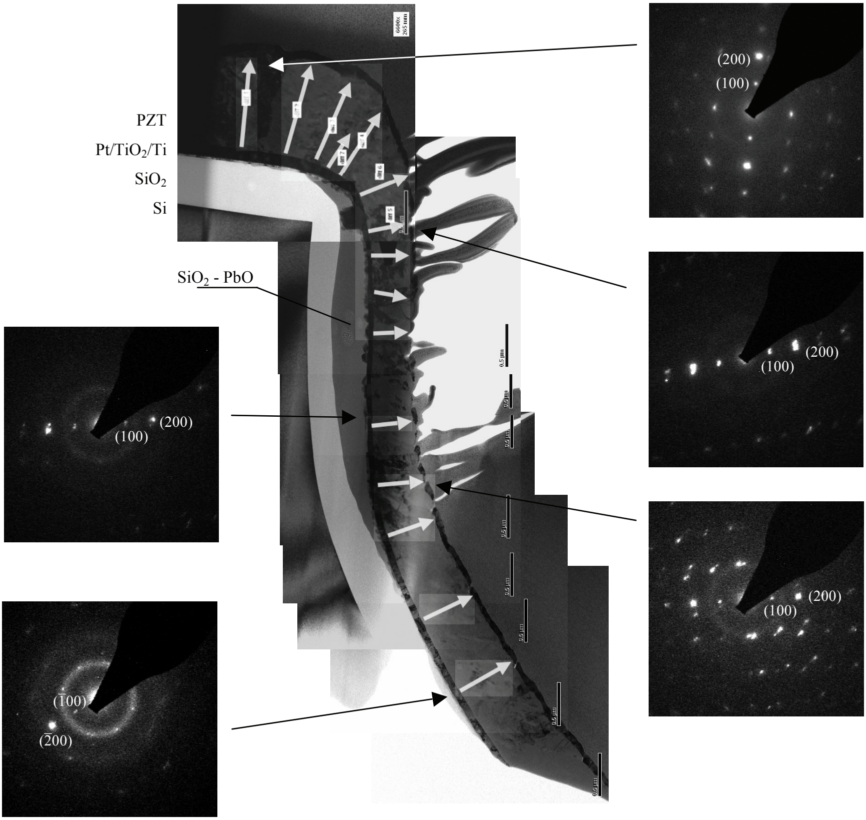

Figure 4.26: TEM micrographs and diffraction diagrams confirming the {100}-preferred growth orientation of the sputtered PZT film along the silicon substrate. The white arrows on the PZT layer correspond to the direction of the {100}-grain growth obtained from the diffraction diagrams.

These results are exposed in Figure 4.26. The diffraction diagrams clearly show that the grains grow perpendicular to the substrate in the {100}-preferred orientation proving the diffusion growth mode of the sputtered PZT layer. Moreover, the platinum bottom electrode grows perpendicular to the substrate as well. This deposition is made at 300°C. Thus, the PZT layer follows exactly the crystalline plane of the bottom electrode, using the lead titanate seed layer, to grow in the {100}-preferred orientation anywhere on the substrate.

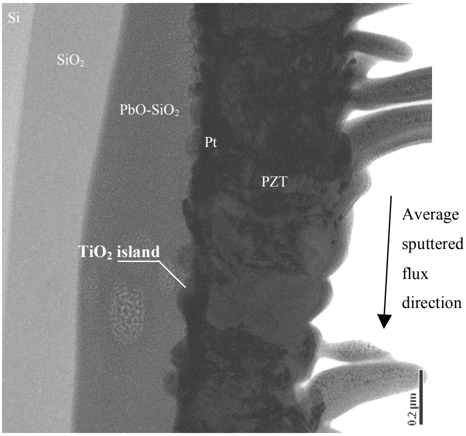

Figure 4.27: TEM micrograph of vertical wall parallel to the PZT sputter flux illustrating the creation of a SiO_2-PbO layer due to the diffusion of the lead (contained in PZT) to the SiO_2. This diffusion is caused by the bad homogeneity of the Ti/TiO_2 barrier-layer.

Chemical analysis has been made along the PZT thin film, on the bottom electrode and on the silicon dioxide using EDX (Energy Dispersive X-ray Analysis) profile realized in a TEM facility. Along the vertical part of the substrate, a darker layer is seen between the silicon dioxide and the platinum bottom electrode (Figure 4.27). This phase turns out to be a mixture of SiO_2 and PbO. Effectively, the adhesion layer of Ti/TiO_2 as well as the Pt layer are thinner on the walls. The titanium film is only 3 nm and the titanium dioxide is 20 nm. A TEM micrograph shows TiO_2 islands at the walls after PZT deposition. The electrode stack thus becomes a less good diffusion barrier. The lead contained in the PZT film diffuses through the Platinum layer to the silicon substrate and forms a SiO_2-PbO phase in the silicon dioxide. This effect is also reflected in the chemical analysis showing stoichiometric PZT in this area, and excess Pb on the less inclined areas. On the non-damaged part of the barrier layer, about

30% excess lead is measured, as no lead excess is measured along the damaged barrier layer (Figure 4.28). This PbO-SiO_2 phase is made out of quartz and $Pb_5Si_8O_{21}$ [23]. As the PZT deposition is carried out at 570°C, the phase formation is either high or low quartz. $Pb_5Si_8O_{21}$ is presumed to be a stable phase because it could be made dry by reaction of quartz with hexagonal $PbSiO_3$, or by hydrothermal crystallization from glass. Fortunately, this part is polished away during the CMP process. The zirconium content varies from 53 to 60 at%. On the vertical part, the Zr content drops considerably to 40 at% (Figure 4.28). This change is due to a better mobility of the Ti atoms regarding Zr.

No other phase than the perovskite one was detected, even though lead excess was observed. This phenomenon has been observed in the past, and ascribed to the presence of Pb^{4+} ions on the B-site. It occurs only when lead containing perovskites are deposited by sputtering with in-situ crystallization [24, 25]. A possible explanation of the absence of B-site lead on vertical walls can be the absence of ion bombardment. The oxidation of Pb to Pb^{4+} could thus be assigned to bombardment by negative oxygen ions. Further experiments would be needed to rule out the first explanation given before, i.e. lead loss by interdiffusion happening also there, where no ion bombardment occurs.

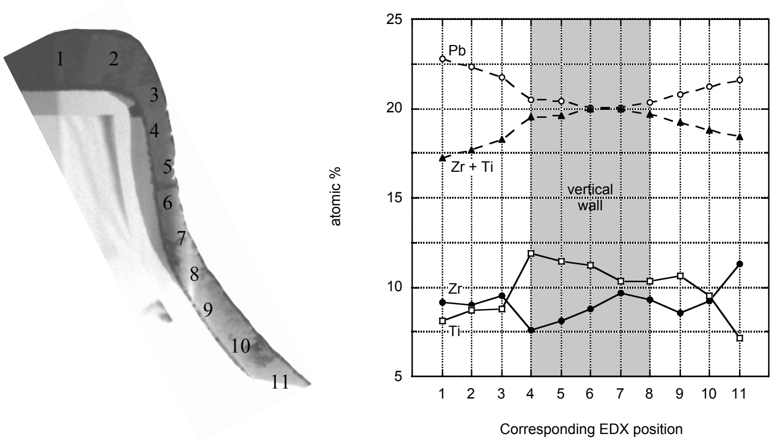

(a) (b)

Figure 4.28: EDX chemical analysis of the zirconium, titanium and lead along the PZT layer (b) grown on a non-flat surface (a).

4.6.5 TOP ELECTRODE

Top electrode was first deposited by lift-off using 15 nm chromium and 100 nm gold evaporated materials. Problems occur due to bad step coverage, internal stress and shadowing effect of the layer, principally due to this method. It is well known that evaporation is a good method for lift-off process due to bad step coverage. The resist is then easily dissolved because it is in direct contact with solvent (Figure 4.29). Even if the deposition rate is very much larger than sputtering (thousand of layers per second compared to one atomic layer per second), discontinuities appear along the top electrode and open circuits, from top till down the calotte cavity.

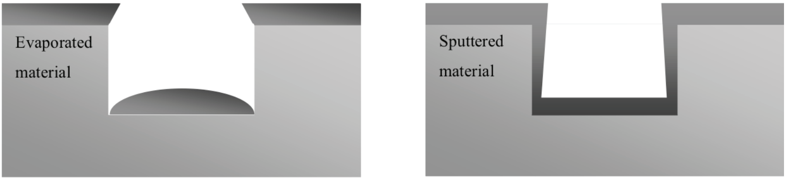

Figure 4.29: Schema showing evaporation vs sputtering of a material into a cavity.

Sputtering method was thus used instead of evaporation, giving a much better step coverage and adhesion of the layer along the top electrode. The material deposited was a layer of 100 nm of platinum under DC bias of 50 V with a gas flux of 40 sccm of Ar at a pressure of 10 mTorr. Although the PVD method gives good step coverage, the spray-coated photoresist is so thick that no problems were encountered dissolving it. This method gives a well-patterned top platinum PVD electrode.

After top electrode deposition and patterning, front side of the device is finished. Last step of the process consists of a backside etch to liberate completely the calottes and thus complete the entire process.

4.7 LIBERATION OF MEMBRANE

Dry anisotropic etching is chosen to liberate the calottes from the backside of the wafer. Deep RIE/ICP silicon etching is performed. The entire wafer has to be etched from part to part to reach the calotte. As wet oxidation was first used to deposit the SiO_2, this layer will be exploited as hard mask to perform the post silicon etching.

Firstly, a photolithography is achieved on the backside to prepare the hard oxide mask. The etching is performed in an Alcatel RIE/ICP 601^E reactor using C_2F_6 gas (20sccm). The applied power on the coil is 1500W and the applied bias on the platen is 80V. The etch rate is around 320 nm/min, with a selectivity of 1 to 1 regarding the photoresist.

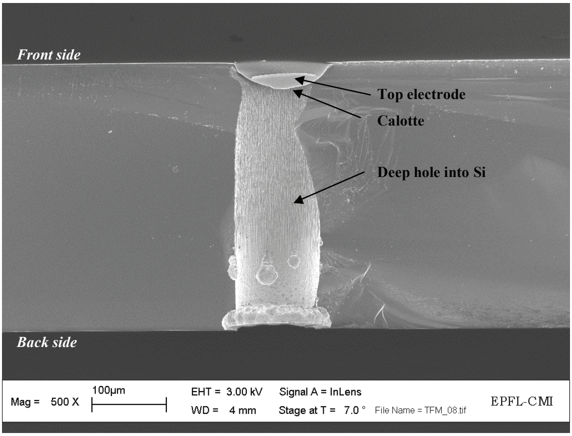

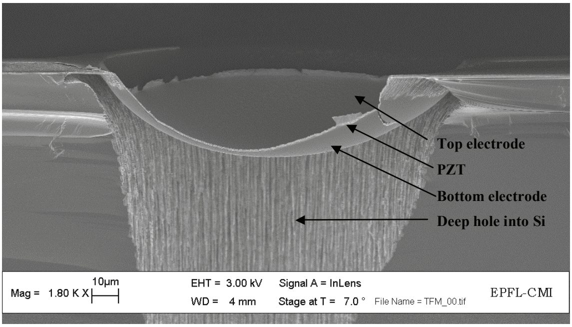

Figure 4.30: Released calotte with deep RIE silicon etching using Bosch process with CMP.

Then the silicon layer (~380 µm) is etched using the Bosh process [26] with sequentially alternating 300 sccm of etching gas SF_6 for 9 seconds and 200 sccm of passivation gas C_4F_8 (polymerization of side wall) for 2 seconds. Applied power on the coil is 1800W and applied bias on the platen is 80V. The etch rate is around 7 to 10 µm/min. The selectivity is about 200 with respect to SiO_2.

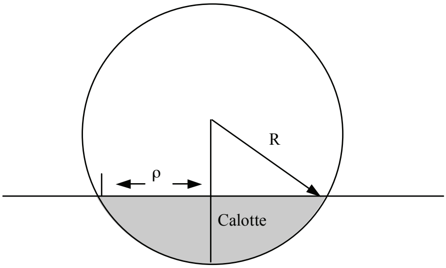

Figure 4.31: Schematic view of the calotte with radius of curvature R and opening ρ

The last layer of SiO_2 is etched using C_2F_6 gas to release the calotte. Figure 4.30 shows the finished device that is the membrane with a calotte shape done only of PZT and its electrodes. Figure 4.31 shows a schematic view of the geometry of the calotte with the curvature radius R and the opening radius ρ. Figure 4.32 is the top view of the device, showing the calotte membrane, top and bottom electrode contacts. The darker part connecting the calotte membrane and the top electrode contact is free of PZT to avoid parasitic capacitance.

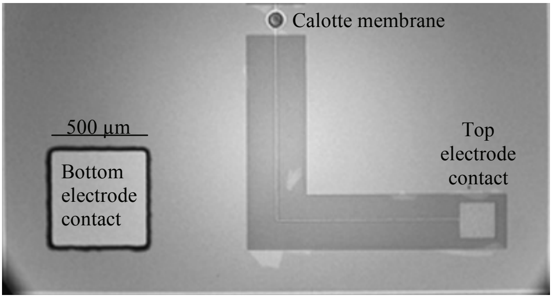

Figure 4.32: Microscope top picture of complete calotte device.

4.7.1 SUMMARIZED PROCESS FLOW

Starting with a double side polished wafer (380 µm), 650 nm of thermal wet oxide is grown (A). The latter is patterned to attack the silicon with the isotropic HNA solution to form the calotte micromould. This step is followed by CMP process to soften the sidewalls (B).

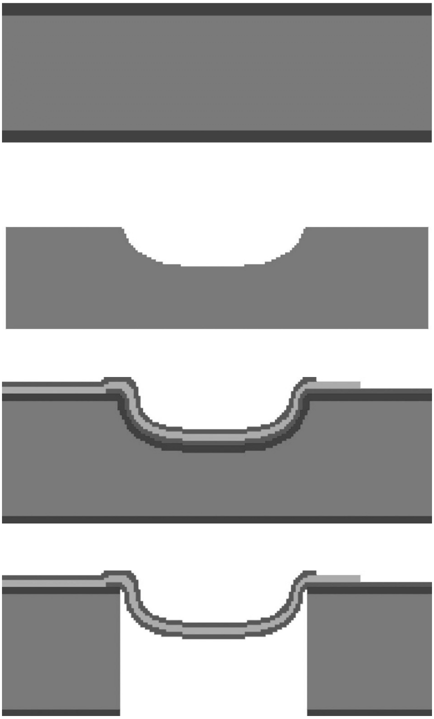

A. Double side polished wafer (380 µm) with 650 nm of SiO_2 wet oxide.

B. SiO_2 is patterned to etch the Si with HNA solution followed by CMP process to soften the sidewalls.

C. Further SiO_2 wet oxide, Ti, TiO_2 and Pt PVD bottom electrode, $PbTiO_3$ and PZT PVD piezoelectric layer and Pt top electrode are deposited and patterned.

D. Subsequent SiO_2, Si and SiO_2 are etched away by RIE/ICP dry etching to liberate the calotte membrane.

Figure 4.33: Generic process flow for the microfabrication of calotte membrane (cross section).

Further SiO_2, Ti/TiO_2 adhesion and barrier layer followed by 100 nm platinum are sputtered at 300°C on the substrate. This layer will be used as bottom electrode. The platinum layer is patterned to avoid any parasitic capacitance between top and bottom electrodes on non-active parts of the device. A 15 nm lead titanate film is sputtered at 530°C as a seed layer to give the PZT film the desired {100}-

orientation. The 1 µm 45/55 PZT film is directly sputtered on the nucleation layer at about 570°C. Sputtered platinum is deposited on the PZT at room temperature as top electrode. This layer is patterned by lift-off process (C).

Subsequent SiO_2, Si and SiO_2 are etched away by RIE/ICP dry etching to liberate the calotte membrane from the backside (D).

4.8 CHARACTERIZATION & RESPONSE

Characterization on the material (PZT) has been performed and response of the device has been measured using different characterization methods such as:

- SEM and TEM analysis
- Dielectric coefficient
- Ferroelectric loop
- Resonance frequencies
- Amplitude deflection

4.8.1 STRUCTURAL ANALYSIS

Different measurements on the PZT material are performed to characterize the structure of the layer.

4.8.1.1 SEM Micrograph

Scanning electron microscopy was used to observe top views and cross-sections of the calotte device and the stack of all the different layers deposited. Thickness, density and discontinuity can be qualitatively determined by this method.

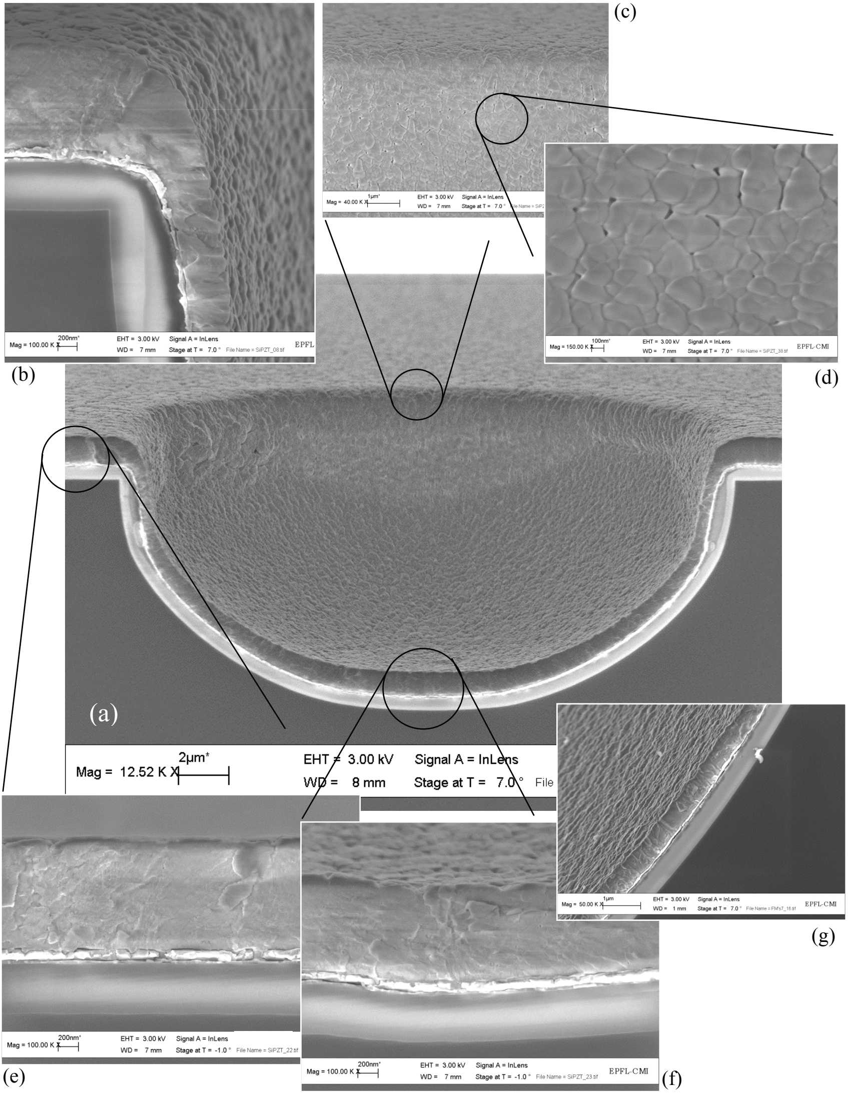

Figure 4.34: SEM micrographs of the entire calotte without CMP (a). (b) shows an enlarged cross section of the edge. (c) and (d) show top view of the PZT layer. (e) is a cross section of the PZT layer at the top of the substrate beside the calotte and (f) at bottom of the calotte.(g) is between (e) and (f).

Figure 4.34 shows the 1 μm PZT sputtered layer on the substrate. The film is dense and has the same thickness at the top of the substrate (e) and at the bottom of the calotte (f). No discontinuities can be observed along the platinum bottom electrode and the PZT layer, even at the edge of the calotte (b). PZT grains are about 200nm large (d).

4.8.2 DIELECTRIC & PIEZOELECTRIC RESPONSE

Dielectric coefficient has been measured using an impedance analyzer HP 4194A. The $\varepsilon_{33,f}$ value was 830 with a loss of 5% for a 45/55 PZT at 1 kHz. This value is in good agreement with the work done by S. Hiboux on in-situ sputter properties of PZT [27] even if the deposition is performed on a non-flat surfaces.

The transverse response is quantified by the $e_{31,f}$ value of the film. Beam structure were added in the design to measure the transverse piezoelectric coefficient directly on the same wafer as the calotte device. A value of -6.50 C/m^2 has been evaluated.

4.8.3 FERROELECTRIC LOOPS

As in chapter 3, the ferroelectric property measurements were performed with the setup of the ceramics laboratory. Polarization hysteresis loops were obtained by using a triangular waveform.

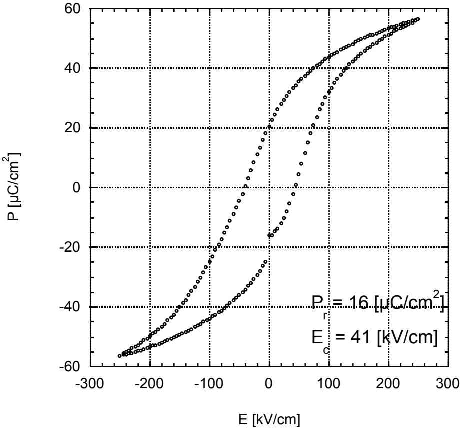

Figure 4.35: Polarization hysteresis loop of PZT 45/55 of calotte measured at 250Hz.

Figure 4.35 shows the hysteresis loop of PZT 45/55 deposited on prepared substrate for calotte device fabrication. This measurement has been performed on $e_{31,f}$ beam structures present on the design of the device. A remnant polarization of 16µC/cm^2 and a coercive field of 41kV/cm are measured. As for the value of the dielectric constant, remnant polarization and coercive field are good classical values for this kind of film concentration.

4.8.4 RESONANCE FREQUENCY

All the measurements and characterizations made so far on the PZT film show that it exhibits good texture, density, homogeneity, dielectric and ferroelectric responses. These tests were essential to the next characterization, which is the device response itself. Without a good piezoelectric PZT layer, either no or bad response of the device would be measured.

Table 4.2: Resonance frequency of different size of calottes.

Calotte's radius ρ [µm]	**35**	**40**	**45**	**50**	**55**
Resonance frequency [MHz]	16.5	9.1	6.9	5.6	2.5

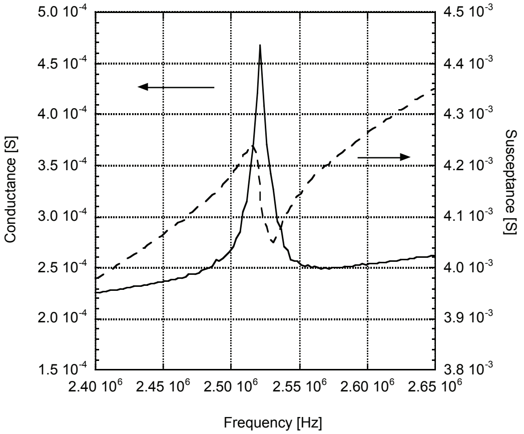

Figure 4.36: Admittance curve of a 110µm in diameter calotte.

The complex admittance is thus measured using the impedance analyzer HP 4194A. The fundamental resonance frequencies vary between 2.5 and 16.5MHz (Table 4.2). Figure 4.36 shows the real and imaginary part of the admittance curves of a calotte with 55µm of base radius ρ at the resonance frequency of 2.5MHz. An applied AC voltage of 0.1V and DC voltage of 10V are used. The resonance frequencies are found to be inversely proportional to the square of the base radius ρ (Figure 4.37) as:

$$f_r = \frac{0.08\ [\mathrm{Hz}\cdot\mathrm{m}^2]}{\pi\rho^2} \tag{4.19}$$

This is the same dependence on ρ as for a flat clamped disk, however, with a considerably higher prefactor (0.01 for a flat clamped disk made out of the PZT film and its electrodes).

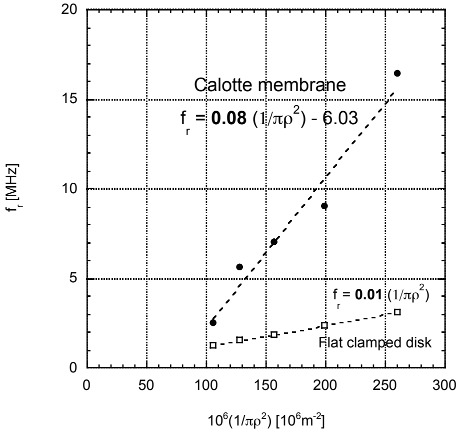

Figure 4.37: Resonance frequencies function of the inverse square of the radius of the calotte membrane and a flat clamped disk.

4.8.5 AMPLITUDE DEFLECTION

The low frequency amplitude is measured with an AFM. A long Si tip is used in order to have contact with the bottom of the 40µm deep calotte (Figure 4.38 a).

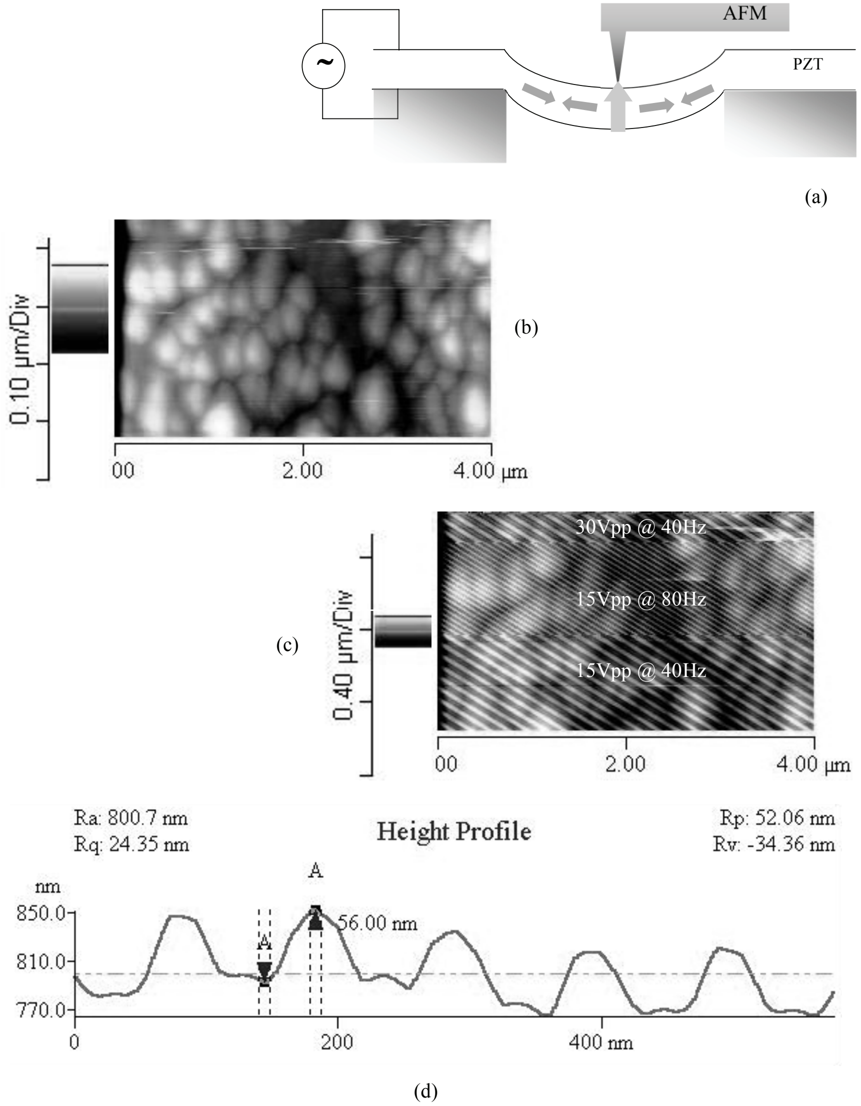

***Figure 4.38:** Measurement by AFM of the calotte deflection as a function of an applied AC voltage (a). Corresponding AFM picture without any applied AC voltage showing only roughness (b). the (c) picture is the same AFM picture with different applied AC voltages at different frequencies. The bottom curve, (c), is part of the profile of the (d) picture at 15 Vpp and 40 Hz.*

Figure 4.38 (b) shows an AFM picture of the bottom of the calotte (1Hz). First, no voltage is applied. Only the roughness of the sample can be detected, which is about 50nm. Once the AC voltage is applied, a direct response of the deflection of the calotte membrane can be observed (Figure 4.38 c). We clearly detect a difference in the period of the device when changing the input signal frequency as well as its amplitude.

With this method, a responsivity of 3.5nm/V is observed, which is an estimated factor 50 times higher than free d_{31} coefficient ($\approx$ -60pm/V) or clamped d_{33}. This shows that the PZT layer is active and that there are no open or short circuits along the top electrode and between top and bottom electrodes. It also shows that the shape of this calotte structure gives an excellent deflection response compare to the deformation of the PZT layer itself (d_{31}).

4.9 SUMMARY

As three-dimensional (3D) structure could be more useful for the performance of microsystem and could provide more flexibility on designing microsystems, feasibility of 3D microstructures have been demonstrated by means of a piezoelectric micro-electro-mechanical device in spherical calotte. These calotte membranes consisting of platinum bottom electrode, piezoelectric PZT and platinum top electrode were successfully developed and microfabricated. The HNA wet etching was chosen to structure the micromould in which the membrane was prepared. Deposition of bottom electrode, PZT and top electrode was done without any problems even on three-dimensional structures. Backside liberation was successful using Bosch process.

Structural analysis shows that the PZT has grown in the wanted orientation, i.e. {100} with a relative intensity of 98.4%. SEM micrograph showed a dense and homogeneous PZT layer without any discontinuities even on the edge of the calotte. The thermal surface diffusion is predominant and determines the observed microstructure on oblique surfaces. This means that the arriving atoms do not stick immediately after impinging, but migrate around before getting chemisorbed in a unit cell. SEM micrographs reveal that the PZT grains are perpendicular to the substrate even on surfaces parallel to the sputtered flux. The crystallographic planes, i.e. {100} are parallel to the local surface, as determined by TEM diffraction. The Pt electrode grows also in (111)-texture. This means that the complete texture sequence for {100}-texture, including electrode and seed layer, works on vertical walls as well as on horizontal planes. The PZT thin films exhibit a lead excess on horizontal surfaces, and no lead excess on vertical walls. One possible explanation that is compatible with earlier observations, would be the existence of Pb^{4+} ions on the B-site, due to bombardment by negative oxygen ions. Such a bombardment does not occur on vertical walls. Unfortunately, there is also another possible explanation, namely the lead loss into the substrate, which was only observed on vertical walls, and is due to the thinner Pt/TiO_2 stack on the vertical walls. In the final device, the vertical walls do not occur, since this part of the recession was removed by CMP.

The average dielectric constant of the complete device amounted to of 830 with a loss of 5% at 1kHz, corresponding quite closely to the values on flat surfaces. Ferroelectric loops indicated a remnant polarization of 16µC/cm^2 and a coercive field of 41kV/cm. The measured fundamental resonance frequencies varied between 2.5 and 16.5MHz. The vertical deflection amplitude in the Hz range (quasi-DC) amounted to 3.5nm/V. This values shows that the calotte structure amplified the ordinary d_{31} by a factor of 20 to 50. This large value cannot be explained in a simple way. The calculation at the beginning of this chapter would yield a result of a factor of 2 to 3. However, reality is much more complex than assumed in the simple model. The actual realized shape is quite different from the simple model.

4.10 REFERENCES

1. N. Ledermann, P. Muralt, J. Baborowski, M. Forster and J.-P. Pellaux, *Piezoelectric* $Pb(Zr_x, Ti_{1-x})O_3$ *thin film cantilever and bridge acoustic sensors for miniaturized photoacoustic gas detectors*, J. Micromech. Microeng., **14**, 1650-1658 (2004)
2. P. Lugienbuhl, S. D. Collins, G.-A. Racine, M.-A. Grétillat, N. F. D. Rooij, K. G. Brooks and N. Setter, *Microfabricated Lamb wave device based on PZT sol-gel thin film for mechanical transport of solid particles and liquids*, J. Micromech. Syst., **6**, 337–346 (1997)
3. K.R. Udayakumar, S.F. Bart, A.M. Flynn, J. Chen, L.S. Tavrow, L.E. Cross. R.A. Brooks and D.J. Ehrlich, *Ferroelectric thin film ultrasonnic micromotors*, Proc. of MEMS 1991, Nara, Japan, 109-113 (1991)
4. B. Belgacem, F. Calame, and P. Muralt, *Design, modeling and fabrication of piezoelectric micromachined ultrasonic transducers*, in 2005 IEEE International Ultrasonics Symposium, Rotterdam, 487-490 (2005)
5. R.E. Newnham, Q.C. Xu and S. Yoshikawa, *Transformed stress direction-acoustic transducer*, Us Patent No. 4 999 819 (March 12, 1992)
6. Q.C. Xu, S. Yoshikawa, J. Belsick and R.E. Newnham, *Piezoelectric composites with high sensitivity and high capacitance for use at high pressure*, IEEE Trans. Ultrasonics, Ferroelectr. Freq. Control, **38**, 634-639 (1991)
7. Y. Sugawara, K. Onitsuka, S. Yoshikawa, Q.C. Xu, R.E. Newnham and K. Uchino, *Metal-ceramic composite actuators*, J. Am. Ceram. Soc., **75**, 996-998 (1992)
8. A. Dogan, Q:C. Xu, K. Onitsuka, S. Yoshikawa, K. Uchino, and R.E. Newnham, *High displacement ceramic-metal composites actuators (moonie)*, Ferroelectrics, **156**, 1-6 (1994)
9. K. Onitsuka, A. Dogan, Q.C. Xu, J. Tressler, S. Yoshikawa, K. Uchino, and R.E. Newnham, *Design optimization for ceramic-metal composite actuators (moonie)*, Ferroelectric, **156**, 37-42 (1994)

10. A. Dogan, *Flextensional moonie and cymbal actuators*, Ph.D. Thesis, The Pennsylvania State University, University Park, PA (1994)

11. A. Dogan and R.E. Newnham, *Flextensional cymbal transducer*, US Patent, PSU Invention Discloser No. 94-1395 (1994)

12. G. Thallikar, H. Liao amd T. S. Cale, *Experimental and simulation studies of thermal flow of borophosphosilicate and phosphosilicate glasses*, J. Vac. Sci. Technol., **B 13**(4), 1875-1878 (1995)

13. P. J. French and R. F. Wolffenbuttel, *Low-temperature BPSG reflow compatible with surface micromachining, J. Micromech. Microeng*, **5**, 125-127 (1995)

14. U. Hashim, B. Y. Majlis and S. Shaari, *Thermal budget adjustment of borophosphosilicate glass reflow-anneal for silicide process requirement*, ICSE'98 Proc., Bangi, Malaysia (1998)

15. from Tyndall National Institute website : www.tyndall.ie/PDFs/plating.pdf

16. B. Schwartz, *Chemical etching of silicon IV. Etching technology*, J. Electrochem. Soc., **123**(12), 1903-1909 (1978)

17. M. Madou, *Fundamentals of microfabrication*, CRC Press, 1997, p.166

18. H. Robbins and B. Schwartz, *Chemical etching of silicon II. The system HF, HNO_3, H_2O and $HC_2C_3O_2$*, J. Electrochem. Soc., **107**, 108-111 (1960)

19. K.D. Wise. M.G. Robinson and W.J. Hillegas, *Solide state processes to produce hemispherical components for inertial fusion targets*, J. Vac. Sci. Technol., **18**, 1179-1182 (1981)

20. T. Meader, *Germination et croissance de films minces de PZT sur silicium passivé et substrats métalliques*, Thesis #1689, Ecole Polytechnique Fédérale de Lausanne (EPFL) (1997)

21. S. Trolier-McKinstry, C. Geist, A. Safari, R.E. Newnham and Q.C. Xu, *Etched piezoelectric structures*, International Symposium of Applied Ferroelectrics, ISAF, Bethlehem, PA (1986)

22. J.M. Nieuwenhuizen, H.B. Haanstra, *Microfractography of thin films*, Philips Technical Review, **27**(3-4), 87-91 (1966)

23. R.M. Smart and F.P. Glasser, *Compound Formation and Phase Equilibria in the System PbO-SiO_2*, J. Am. Ceram. Soc., **57**(9), 378-382 (1974)

24. R.W. Whatmore, Z. Huang and M.A. Todd, *Sputtered Lead Scandium Tantalate thin films: Pb^{4+} in the B-sites in the perovskite structure*, J. of Appl. Phys., **82**(11), 5686-5694 (1997)

25. P. Muralt, S. Hiboux, C. Mueller, T. Maeder, L. Sagalowicz, T. Egami and N. Setter, *Excess lead in the perovskite lattice of pzt thin films made by in-situ reactive sputtering*, Integrated ferroelectrics, **36**(1-4), 53 -62 (2001)

26. F. Lärmer and A. Schilp, *US6284148: Method for anisotropic etching of silicon*, USA (2001)

27. S. Hiboux, *Study of growth and properties of in-situ sputter deposited* $Pb(Zr_x,Ti_{1-x})O_3$ *thin films*, Thesis n° 2510, EPFL (2001)

5

PZT COATED ACTIVE AFM CANTILEVERS

5.1 INTRODUCTION

Atomic force microscope (AFM), or scanning force microscope (SFM) was invented in 1986 by Binnig, Quate and Gerber [1] following the invention of the scanning tunneling microscope (STM) by Binnig and Rohrer in 1982 [2]. Like all other scanning probe microscopes, the AFM utilizes a sharp probe moving over the surface of a sample in a raster scan. In the case of the AFM, the probe is a tip at the end of a cantilever that bends in response to the force between the tip and the sample.The first AFM used a scanning tunneling microscope probing the end of the cantilever to detect the bending of the lever, but now most AFMs employ an optical method to detect the bending of the cantilever.

This work is a joint collaboration with NanoWorld AG, a well-known AFM cantilever-tip supplier. The goal of this project was to add a piezoelectric thin film to cantilever in order to obtain active cantilevers useful for higher frequency tip vibration and fast AC signal capture. The special challenge in this project was to add a PZT thin film while keeping the same industrial tip fabrication process as before.

5.1.1 BASIC PRINCIPLE OF AFM

AFM operates by measuring attractive or repulsive forces between a tip and the sample [1]. In its repulsive "contact" mode, the instrument lightly touches a tip at the end of a leaf spring or "cantilever" to the sample. As a raster-scan drags the tip over the sample, a detection apparatus measures the vertical deflection of the cantilever, which indicates the local sample height. Thus, in contact mode the AFM measures hard-sphere repulsion forces between the tip and sample. In noncontact mode, the AFM derives topographic images from measurements of attractive forces; the tip does not touch the sample [3].

AFMs can generally measure the deflection of the probing cantilever with picometer resolution. This is achieved by optical detection [4, 5]. A laser beam is reflected off the cantilever. The deflection angle is evaluated by means of a pair of photodiodes. The difference between the two-photodiode signals indicates the position of the laser spot on the detector and thus the angular deflection of the cantilever. As the cantilever-to-detector distance generally amounts to many thousand times the deflection amplitude of the cantilever, a large amplification is obtained. For a ~2000-fold magnification, a theoretical noise level of 10^{-14}m/Hz$^{1/2}$ is calculated for this detection method [6].

5.1.2 AFM TIPS

Most users purchase AFM cantilevers with their attached tips from commercial vendors, who manufacture the tips with a variety of microlithographic techniques. A close enough inspection of any AFM tip reveals that it is rounded off. Therefore force microscopists generally evaluate tips by determining their "end radius." In combination with tip-sample interaction effects, this end radius limits the lateral resolution of AFM. Therefore, the development of sharper tips is currently of major concern.

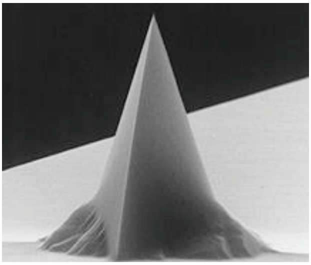

Figure 5.1: The tip is shaped like a polygon-based pyramid with a height of 10-15 µm and with typical tip radius of curvature of less than 10 nm (NanoWorld Pointprobe® NCH sensors).

One of the product of NanoWorld is the Pointprobe® NCH (**N**on-**c**ontact / Tapping™ mode - **H**igh resonance frequency) sensors that are designed for non-contact or tapping™ mode imaging (Figure 5.1). This sensor type combines high operation stability with outstanding sensitivity and fast scanning ability. All sensors of the Pointprobe® series are made from monolithic silicon which is highly doped to dissipate static charge. They are chemically inert and offer a high mechanical Q-factor for high sensitivity. The tip is shaped like a polygon based pyramid with a height of 10-15µm. Additionally this sensor offers typical tip radius of curvature of less than 10nm.

5.1.3 WHEN AFM MEETS PIEZOELECTRIC THIN FILMS

Cantilevers for atomic force microscope (AFM) or scanning force microscope (SFM) are very attractive for piezoelectric thin films. A lot of research has been performed in Japan by Suga since 1993. First, they used a piezoelectric film of ZnO to develop a force sensor to overcome the complexity of the force detector of the conventional non-contact atomic force microscope [7]. Then, they showed that PZT thin films allowed the production of self-excited microcantilevers for dynamic SFM with inherent sensing and actuating capabilities [8, 9]. All these sensors were only made out of a cantilever without any tips with a vertical resolution less than 2Å. Still in Japan, Nikon Corporation was the first to integer a tip and to demonstrate similar results with the use of PZT cantilever for noncontact AFM. The first demonstrator was a silicon cantilever with a PZT thin film as a piezoelectric displacement sensor with an electrochemically etched tungsten stylus that was glued on at the top of the cantilever. The radius was 100nm and the same vertical resolution of 2Å was achieved [10]. Afterwards, they added a silicon nitride pyramidal stylus. The radius of the apex of the pyramidal stylus was 10 nm and a vertical resolution of 0.3Å was measured [11, 12]. There was still a major problem that has to be solved; the PZT thin film is deposited either by sol-gel or sputtering and needed a flat substrate surface. The piezoelectric layer is thus deposited on the flat side of a wafer and the tip fabricated on the other side where a large cavity is performed to do so (Figure 5.2). The cantilever will not be parallel to the sample during measurements, because of the remaining silicon portion hindering access.

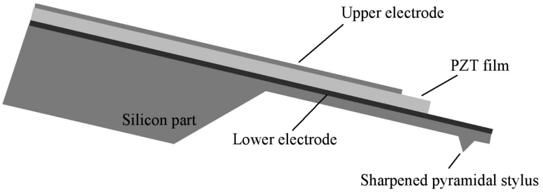

Figure 5.2: Schematic of the PZT-AFM cantilever with the piezoelectric layer deposited on the flat side of the substrate [12].

Another Japanese group resolved this problem by making a diamond base AFM probe integrated with PZT thin film. The PZT layer is directly sputtered on the diamond cantilever, which is fabricated using anodic bounding technique combine with microfabrication techniques employing CVD diamond film [13]. The tip radius was 50nm and a vertical resolution of 4Å was estimated. Such a process does not allow for sharp tips.

Table 5.1: Possible operating modes of a PZT cantilever for AFM.

	Deflection Sensing	Z feedback actuation	Lever oscillation	Ref	Year
1	Optical deflection	PZT Tube	PZT Cantilever	-	
2	Optical deflection	PZT Cantilever	External PZT	[11, 16]	1996
3	Optical deflection	PZT Cantilever	PZT Cantilever	-	
4	PZT Cantilever	PZT Tube	External PZT	[10, 11]	1996
5	PZT Cantilever	PZT Tube	PZT Cantilever	[12]	1999
6	PZT Cantilever	PZT Cantilever	External PZT	[14]	2002
7	PZT Cantilever	PZT Cantilever	PZT Cantilever		2007?

Considerable efforts have been made these last 10 years. The PZT cantilever has been exploited at every stage of the AFM but still not in the same time (Table 5.1). The complete setup could be built using the new PZT cantilever proposed here for each stage replacing the optical deflection, the PZT tube and the external PZT by means of the PZT thin layer response deposited on the cantilever and with a very fine tip radius (R<10nm).

Figure 5.3 shows schematic setup of a self-sensing and self-actuating atomic force microscope using an active PZT cantilever. By keeping the tapping amplitude constant, the response measurement and the height regulation can be achieved only by the PZT thin film.

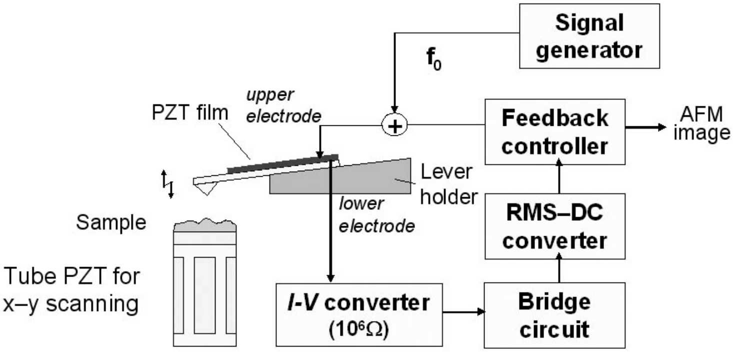

Figure 5.3: Self-sensing and self-actuating AFM with an active PZT cantilever [12].

5.1.4 OUR CONCEPT

It is sought to develop a new type of cantilevers coated with a piezoelectric thin film for atomic force microscopy (AFM). This work is done in collaboration with NanoWorld AG. The innovation consists in combining processes for ultrasharp tips (R<10nm) with coatings of strongly piezoelectric $Pb(Zr,Ti)O_3$ thin films. The latter is deposited by in-situ sputtering [15]. Advanced micromachining techniques have to be applied in order to achieve compatible processes for tip fabrication, PZT deposition and electrode patterning. The fabrication process for the tips is chosen to be as close as possible to the actual production processes for commercially sold tips. Such tips are obtained by an etch-back of the back of the wafer. The PZT is coated on the reversed side into the cavities obtained by anisotropic wet etching before tip fabrication (Figure 5.4). The necessary deposition and patterning steps have to be applied inside the deep cavity obtained by anisotropic wet etching of silicon. The essential process features to enable such structures are the spraying of the photoresist, resist exposure using an optic with a larger depth of focus, and in-situ deposition of PZT with a technique achieving a reasonable step coverage. All steps concerning the PZT side (back side of the tip) will be performed before tip fabrication in order to avoid tip degradation. Tip fabrication and cantilever liberation are performed by NanoWorld AG in the CSEM facilities based at Neuchâtel (CH) according to their proprietary tip fabrication recipes.

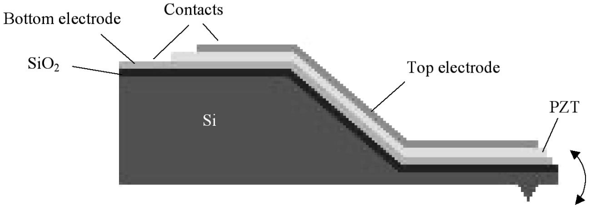

Figure 5.4: Schematic cross section of cantilever structure in cavity containing top electrode / PZT / bottom electrode / SiO_2 / Si. The Silicon tip is on the reverse side of the PZT.

The PZT coated AFM cantilevers allow an improvement of AFM operation in two directions;

1. The PZT can be used as actuator to accelerate the scanning speed. In the transducer mode, the PZT coating can be used to control the tip height in the non-contact (resonant) mode, or the tapping mode.
2. Equipped with sensor capacitor and actuator capacitor, a control *without* interferometric measurement can be built up [16]. This is advantageous in miniaturized devices as needed in UHV instruments [17], and for AFM arrays [18, 19, 20].

For the purpose of the microfabrication of this new type of cantilevers coated with a piezoelectric thin film for atomic force microscopy, new processes have to be investigated and developed. Deposition on oblique surface has already been studied in Chapter 4 when applied on free 3D calottes thin film membranes. Spray coated photoresist has also been studied and applied in Chapter 5. Study of photolithography into deep cavities (more than 300µm) using a normal mask aligner will be carried out to achieve right geometries of the cantilever.

5.2 FABRICATION STEPS

Figure 5.5 shows the generic process flow for the microfabrication PZT coated cantilevers. Starting with a double side polished wafer (380µm), 500nm of thermal wet oxide is grown (A). NanoWorld AG prepared the cavities for the post liberation of cantilever and fabrication of the final AFM silicon tip. Ti/TiO_2 adhesion and barrier layer followed by 100nm platinum is then sputtered at 300°C on the substrate (BAS 450, CMI) (B). This layer will be used as bottom electrode. The platinum layer is patterned to avoid any parasitic capacitance between top and bottom electrodes on non-active parts of the device. A 15 nm lead titanate film is sputtered at 530°C as a seed layer to give the PZT film the desired {100}-orientation. The 1µm 45/55 PZT film is directly sputtered on the nucleation layer at about 570°C. Sputtered platinum or evaporated Cr/Au are deposited on the PZT at room temperature as top electrode. This layer is patterned by a lift-off process. Subsequently, the PZT layer is patterned by wet etching using the same solution as in chapter 4. The platinum bottom electrode is not attacked by the latter. Next, the Pt electrode is removed by dry etching where it is not needed. 600nm of LPCVD silicon nitride is deposited to protect the electrodes and PZT layer from wet and dry etching process for cantilever liberation and tip fabrication. The Si_3N_4 is partially etched on the top and bottom electrode contact area (300nm of 600nm in thickness). The rest of the layer on these parts (last 300nm) will be etched to get access to the contact during cantilever liberation and tip fabrication.

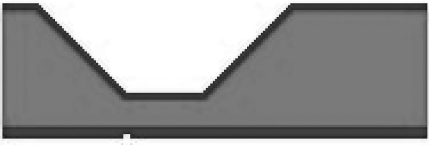

A. Double side polished wafer (380µm) with cavities (360µm) processed by NanoWorld AG and 500nm of SiO_2 wet oxide.

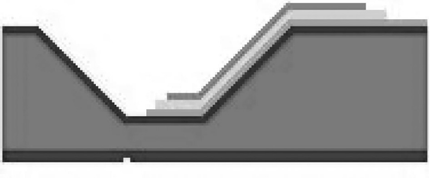

B. Further Ti, TiO_2 and Pt PVD bottom electrode, $PbTiO_3$ and PZT PVD piezoelectric layer and Pt top electrode has been deposited and patterned.

C. Silicon nitride has been deposited and structured to protect PZT and back side from cantilever liberation and AFM Si tip process fabrication.

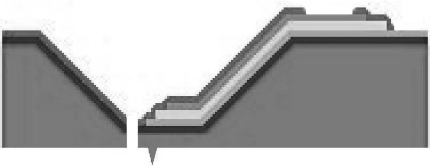

D. The final step consists of the AFM Si tip fabrication and cantilever liberation done by NanoWorld AG.

Figure 5.5: Generic process flow for the microfabrication of PZT coated active AFM cantilevers (cross section).

5.3 PHOTOLITHOGRAPHY INTO CAVITIES

As in chapter 4, spray coated photoresist is used to pattern the deposited films with an ordinary mask aligner (Karl Süss MA/BA6). Of course, regular spin coated photoresist is unusable with such deep cavities (more than 300µm). The resist coverage is critical on some specific sites. These sites are on top and bottom edges of the slope going down the cavity (Figure 5.6). The thickness of the photoresist has to be homogeneous on the whole substrate including on these places.

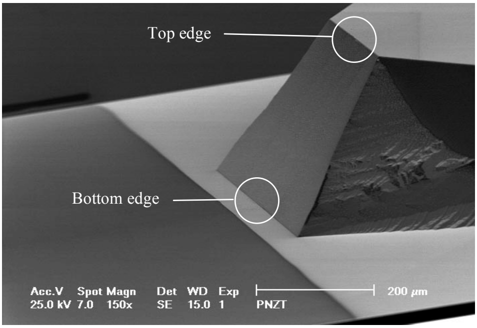

Figure 5.6: SEM micrograph showing crucial sites on top and bottom edges of the slope going down the cavity structured by NanoWorld AG.

By using an ordinary mask aligner, the major problem is the defocus of the optical image of the mask in the cavity (Figure 5.7). The exposed area in the cavity is wider than defined by the mask. Using positive resist serving as etching mask, the line width becomes smaller in the cavity. Applying lift-off with a positive mask, the resulting line width is larger than defined by the mask (Figure 5.8).

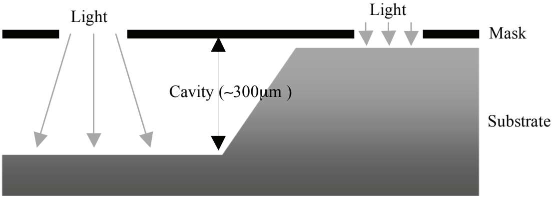

Figure 5.7: Effect of light scattering down the cavity due to the distance separating the mask from the substrate. No defocus of the optical image is present on top of the cavity as the mask is in contact with the substrate.

The mask can be corrected to get the wanted dimensions into the 300µm deep cavities taking light scattering into account (Figure 5.8). Dimensions of the image on the normal mask have to be scaled up (+ 4µm) and, on the lift-off mask, scaled down (– 6µm). The obtained precision is acceptable for our purpose.

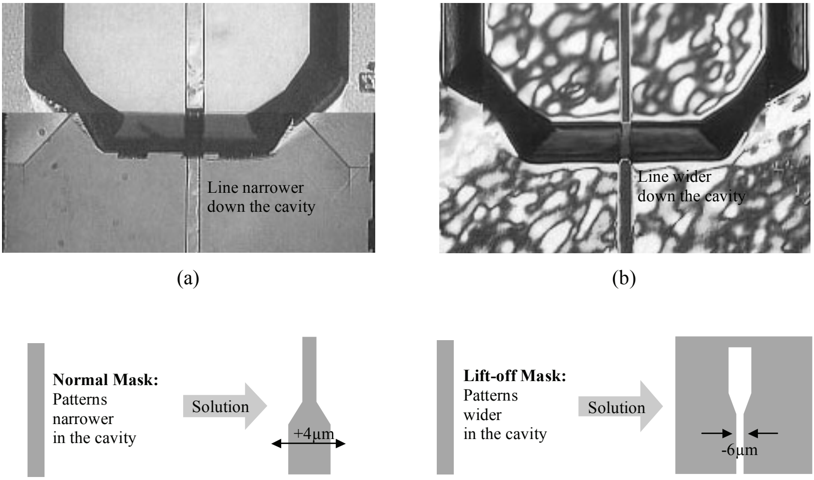

(a) (b)

(c) (d)

Figure 5.8: ***Effect of light scattering on the original optical image of the mask. Light scattering leads to tapered (a) and to broaden (b) width down the cavity. The solution is to adapt the mask geometry to get the right dimensions (c & d).***

5.4 PZT AND TOP ELECTRODE DEPOSITION

Same conditions as in chapter 4 are used for the PZT deposition. SEM inspection has been performed on wafer to see any cracks or discontinuities along the bottom electrode and PZT layer. Figure 5.9 shows 1µm 45/55 PZT film deposited into the cavities on 1µm SiO_2. The film is dense and has the same thickness at the top of the substrate and at the bottom of the cavity. No discontinuity can be observed along the platinum bottom electrode layer especially on the edge present at the top and the bottom of the slope (Figure 5.9). On the other hand, a crack is present in the PZT layer at the bottom edge of the slope. This crack is not important for the PZT layer as the active part will be only on the flat section, on the cantilever, down the cavity. But this crack can cause problems for the deposition of top electrode. No difficulty will be encounter as demonstrated later on. No cracks are present on the top edge of the slope.

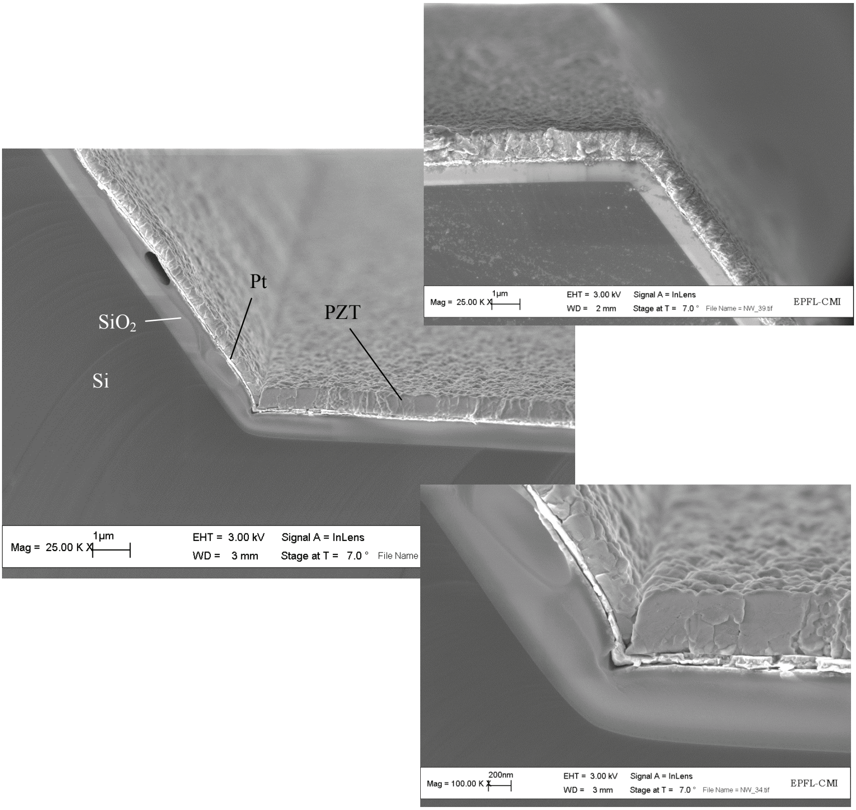

Figure 5.9: SEM images of the top and the bottom edges of the cavity. The silicon structure is covered with thermal oxide, Pt (100nm), and sputtered PZT (1µm).

As explained in Chapter 4, the PZT film has grown perpendicularly to the substrate on the slope down the cavity, although using the sputter process.

Once the bottom electrode and PZT layer are deposited, we can focus on top electrode deposition. After correction of the mask geometries and spray coated photoresist deposition, Cr/Au top electrode has firstly been evaporated on test wafers. These wafers had only 500nm SiO$_2$ and pre-structured cavities. Lift-off process gives excellent result regarding both top and bottom edges of the slope down the cavity (Figure 5.10). No discontinuity or open circuit is present (tested with a Ohm-meter).

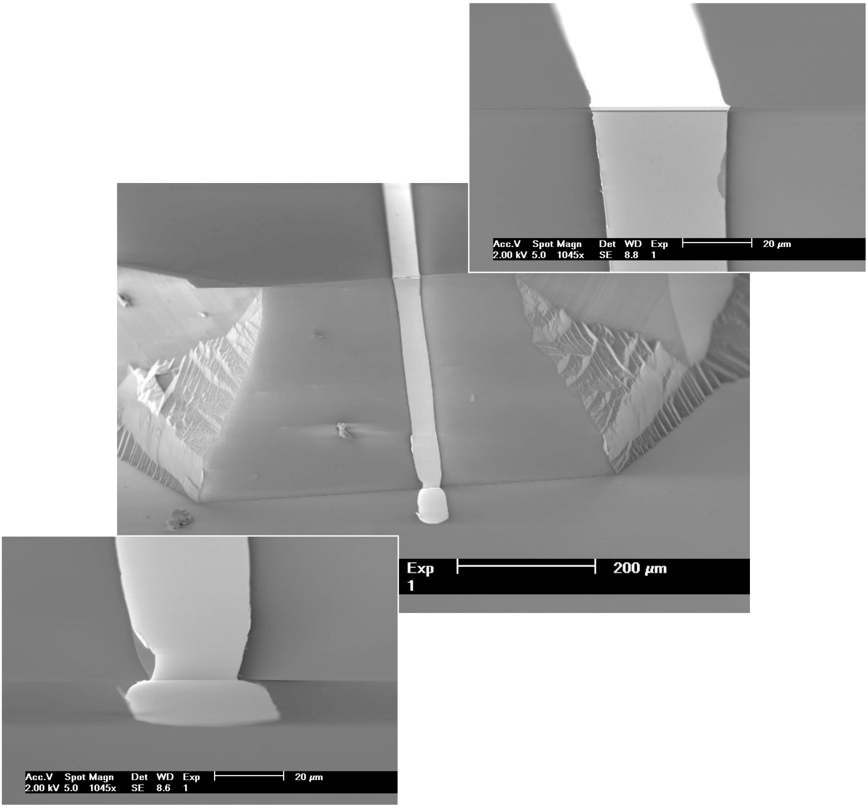

Figure 5.10: SEM images of a patterned metal line going over the high step (300 µm) of the etched cavity.

The same top electrode is then deposited on structured cavity with PZT layer. Even with the crack presents in the PZT film at the bottom edge of the slope, the conductor line has no discontinuity and no open circuit (Figure 5.11).

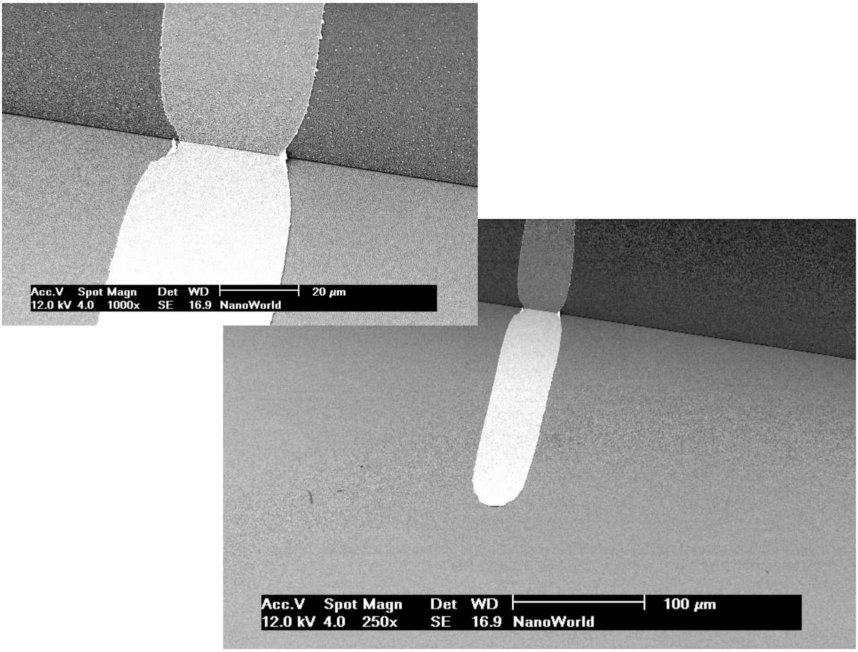

Figure 5.11: SEM micrograph of a patterned metal line deposited on a PZT layer at the bottom of the cavity around the edge site.

5.5 CHARACTERIZATION & RESPONSE

5.5.1 STRUCTURAL AND ELECTRICAL CHARACTERIZATIONS

As explained in previous chapters, {100}-oriented PZT is the best choice for an optimal transverse piezoelectric coefficient. The orientation of the film was verified by X-ray diffraction (Figure 5.12) at a flat part of a device wafer. The measurement shows a strong {100}-orientation. The {100}-texture index is calculated as 92.6%. The tetragonal splitting is well visible at the {n00} peaks. The relative intensities indicate that the c-domains are more than twice as frequent as the a-domains.

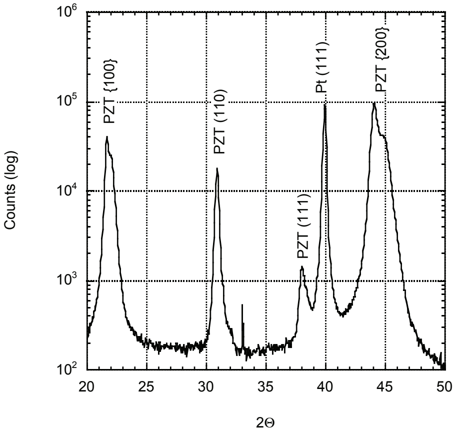

Figure 5.12: θ-2θ X-ray diffractogram of a 1 µm thick sputter deposited PZT layer on a device wafer.

A wafer with cantilevers without tips was fabricated in order to test their piezoelectric response. The planned process sequence was applied until patterning of the bottom electrode. The spray-coated photoresist for the latter process was used then as a mask for the cantilever liberation performed by dry etching from the PZT (cavity) side. The Bosch process was applied for silicon etching. The obtained beam consists of 18µm silicon, 500nm SiO_2, bottom electrode, a 1 µm PZT layer and a top electrode. A micrograph is shown in Figure 5.13.

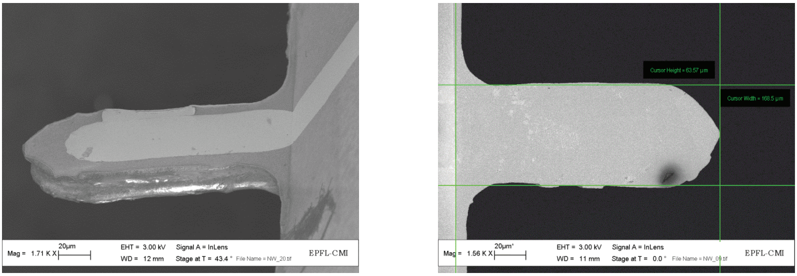

(a) (b)

Figure 5.13: Side (a) and top view (b) of a prototype AFM cantilever with structured PZT layer and top electrode (without Si tip).

The relative dielectric constant was measured as 860, dielectric loss factor tan δ as 5.1%. The ferroelectric loop is shown in Figure 5.14. A remnant polarization of 15µC/cm^2 and a coercive field of 42kV/cm are derived.

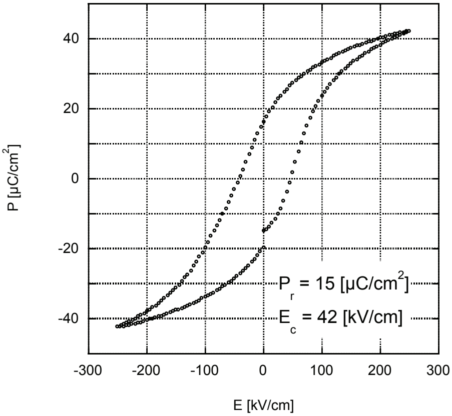

Figure 5.14: Ferroelectric loop of the PZT layer of the cantilever measured at a frequency of 250Hz..

5.5.2 ELECTRO-MECHANICAL RESPONSE OF PZT/SILICON CANTILEVER

5.5.2.1 Resonance frequency of bimorph PZT/Silicon

For the calculation of the resonance frequency, it is assumed that residual stresses are negligible (silicon thickness > 10µm). The resonance frequencies of a beam are given by [21]:

$$\omega_i^2 = \frac{\lambda_i^4}{L^4}\frac{\hat{E}I}{\rho A} \tag{5.1}$$

where I is the inertial moment of the beam defined by:

$$I = \frac{bh^3}{12} \tag{5.2}$$

and $\lambda_1 = 1.875$, $\lambda_2 = 4.694$, $\lambda_3 = 7.855$ and $\lambda_4 = 10.996$, h the thickness, L the length, Ê the effective Young modulus (Pa), ρ the density, A the section and b the width of the beam. By replacing (5.1) in (5.2) and as $A = h \cdot b$, ω_i^2 becomes:

$$\omega_i^2 = \frac{\lambda_i^4}{L^4}\frac{\hat{E}bh^3}{12\rho A} = \frac{\lambda_i^4}{L^4}\frac{\hat{E}h^2}{12\rho} \tag{5.3}$$

Thus, the resonance frequency can be written as:

$$f_{r,i} = \frac{\lambda_i^2}{4\pi}\frac{h}{L^2}\sqrt{\frac{\hat{E}}{3\rho}} \tag{5.4}$$

For a bimorph structure, the coefficient ÊI of equation (5.1) is given by:

$$\hat{E}I = b\frac{\sum\limits_{n=1,2}\left(\hat{E}_n^2h_n^4\right) + \hat{E}_1\hat{E}_2h_1h_2\left(4h_1^4 + 6h_1h_2 + 4h_2^2\right)}{12\sum\limits_{n=1,2}\hat{E}_nh_n} \tag{5.5}$$

where subscripts 1 and 2 refer to the silicon and PZT layer respectively.

Table 5.2: Materials properties of the cantilever.

	h [µm]	**Ê [GPa]**	**ρ [kg/m^3]**
Si	18	130	2330
PZT	1	725	7390

For an average 170 ± 2% µm long test structure cantilever (measured on 15 samples), a resonance frequency of 753kHz and 684kHz are calculated with single silicon layer model with (equation 5.4) and bimorph model (equation 5.5 in 5.1) respectively. The measured resonance frequency, performed on 15 different test structures, is 679 ± 3% kHz. This value is bigger than the one predicted for the final structure (~250kHz) as the silicon layer has to be etched down to 5µm to fabricate the Si tip. The complex admittance is measured using the impedance analyzer HP 4194A and is shown on Figure 5.15 for one prototype. An applied AC voltage of 1V and DC voltage of 10V are used.

Even with a difference in the shape (the assumed lever is a parallelepiped, but the real lever doesn't fit this shape) the measured value is in very good agreement with the calculated value using the bimorph model. The quality factor Q is 960 ± 9% and the coupling coefficient k is 5.7% with a standard deviation of 0.35 (6%). These values were calculated based on a $L_mC_mR_m$ Mason type equivalent circuit model taking the parasitic capacitance C_0 into account.

$$Q = \frac{1}{\omega R_m C_m} \tag{5.6}$$

$$k = \sqrt{\frac{C_m}{C_0}} \tag{5.7}$$

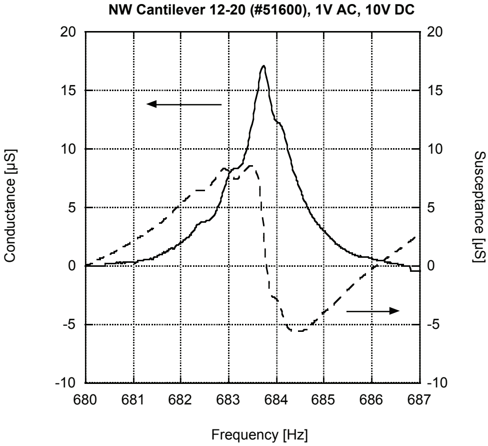

Figure 5.15: Admittance curve showing the resonance frequency of a PZT cantilever at 683.7kHz.

5.5.2.2 Response of PZT/Silicon cantilever as a function of applied voltage

The deflection of the prototype cantilever, schematically shown on Figure 5.16, is measured with an AFM. The Si tip is placed nearby the end of the beam and different AC voltages are applied at a frequency of 40Hz (Figure 5.17). This will be compared to the Gardeniers bending model (1998) [22] who introduces the lateral deformation (Poisson's effect) as well as the dimension of the top electrode. But it is restricted to thick substrate (i.e. $h_{Si} >> h_{PZT}$), as compared to Smits (1991) [23], which proposed a model with different loading conditions (uniform pressure, force or tip displacement). Effectively, the Smits model takes into account the ratio between the piezoelectric film thickness and the silicon substrate but not the effect of the lateral shrinkage due to the Poisson's effect and is mainly used to very large beams compared to their thickness.

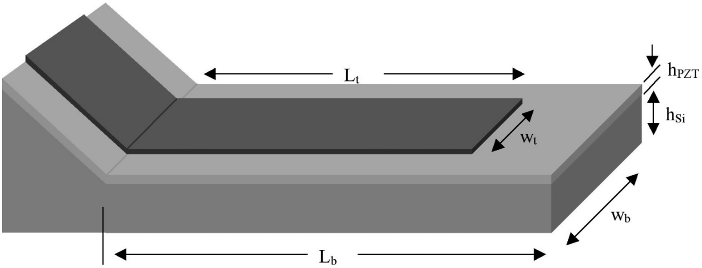

Figure 5.16: Schematic view of the cantilever with notations.

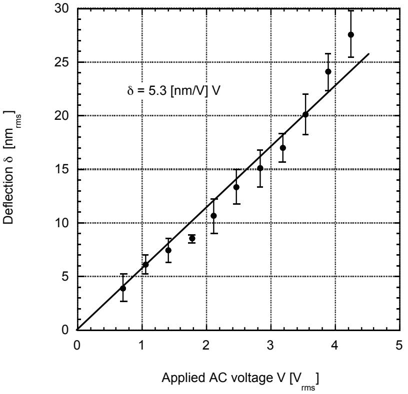

Figure 5.17: Measurement of the beam deflection as a function of applied AC voltage at 40Hz.

Gardeniers gives the transverse deflection δ(L) of a piezoelectric heteromorph cantilever as a function of the driving voltage V by:

$$\delta\left(L\right) = -6 \;\; e_{31,f} \;\; \frac{1}{\hat{E}_{Si}h_{Si}^2}\left(L_b L_t - \frac{L_t^2}{2}\right)\frac{w_t}{w_b}V \tag{5.8}$$

where $e_{31,f}$: effective transverse piezoelectric coefficient [C/m^2]

$\hat{E}_{Si}$: effective Young modulus of silicon [Pa]

h_{Si} : substrate thickness [m]

L_b, L_t : length of beam and top electrode [m]

w_b, w_t : width of beam and top electrode [m]

V : applied voltage [V]

Note that for an infinite beam ($L_b >> w_b$), the effective Young modulus Ê is equal to the E. For a wide beam ($L_b \approx w_b$),

$$\hat{E} = \frac{E}{\left(1-\nu^2\right)} \tag{5.9}$$

where E : Young modulus = $\frac{1}{s_{11}}$ [Pa]

$s_{11,Si}$: elastic compliance of silicon = $7.66 \cdot 10^{-12}$ [m^2/N]

ν : Poisson’s coefficient [-]

In the present case, where the width w_b is about the third of the beam length L_b,

$$\hat{E} = \frac{E}{\left(1-\nu\right)} \tag{5.10}$$

The transverse piezoelectric coefficient d_{31} is calculated as follow:

$$d_{31} = e_{31,f}\left(s_{11,PZT} + s_{12,PZT}\right) \tag{5.11}$$

where $s_{11,PZT}$: elastic compliance of PZT = $13.8 \cdot 10^{-12}$ [m^2/N] [24]

$s_{12,PZT}$: elastic compliance of PZT = $-4.07 \cdot 10^{-12}$ [m^2/N] [24]

Using equation (5.10) in (5.8) and taking the measured deflection of 5.3 nm/V from Figure 5.17, h_{Si} = 18μm, L_b = 170μm, L_t = 160μm, w_b = 56μm, w_t = 35μm, $s_{11,Si} = 7.66 \cdot 10^{-12} m^2/N$ and ν_{Si} = 0.278, an effective transverse piezoelectric coefficient $e_{31,f}$ of -6.54C/m^2 is calculated. With equation (5.11), the transverse piezoelectric coefficient d_{31} is obtained as -63.7pm/V.

Table 5.3 gives the calculated values of the model. As the design of the device does not have $e_{31,f}$ test structures, these calculated values can be compared to the one of previous chapter measured on flat wafer. As the same PZT deposition condition has been used, the PZT layer has the same thickness and the same composition.

Table 5.3: $e_{31,f}$ and d_{31} values of test structure cantilever using Gardeniers's models and experimental value.

Models	**$e_{31,f}$ [C/m^2]**	**d_{31} [pm/V]**
Gardeniers with structured top electrode [22]	-6.54	-63.7
Experimental value on flat wafer (chapter 4)	-6.50	-63.2

By using the Gardeniers model, the effective transverse piezoelectric coefficient $e_{31,f}$ is very well approximated for such a PZT sputtered film as compared with the experimental value.

5.5.2.3 Response of PZT/Silicon cantilever as a function of position

The deflection was measured as a function of the beam position at an applied AC voltage of 2.83V_{rms}, at 40Hz). The resultant curve is proportional to x^2, where x is the position on the beam (Figure 5.18).

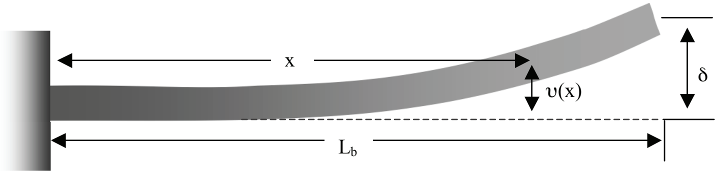

Figure 5.18: Schematic view of the cantilever.

The deflection response can be calculated using the Meng, Mehregany, Deng model (1993) [25]. The model supposes a bending deformation occurring without extensional strain in the mid plain. Then a curvature κ is defined as:

$$\kappa = \frac{d^2\upsilon}{dx^2} \tag{5.12}$$

where υ : vertical displacement of the mid-plane

If the laminate is fixed at one end as in a cantilever beam geometry, the deflection $\upsilon(x)$ can be obtained by solving equation (5.12). In the present case,

$$\upsilon(x) = \frac{\kappa}{2}x^2 \tag{5.13}$$

For a single PZT/Silicon cantilever, equation (5.13) becomes:

$$\upsilon(x) = \frac{3(\eta+1)}{\left(\xi\eta^3 + 4\eta^2 + 6\eta + 4\right)\xi\eta + 1} \cdot \frac{1}{\hat{E}_{Si} h_{Si}^2} \; e_{31,f} \;\; \Delta V \;\; x^2 \tag{5.14}$$

where

$$\xi = \frac{\hat{E}_{PZT}}{\hat{E}_{Si}} \tag{5.15}$$

and

$$\eta = \frac{h_{PZT}}{h_{Si}} \tag{5.16}$$

h_{Si} and h_{PZT} are the substrate and PZT thicknesses respectively and ΔV the applied voltage. Taking the same maximum deflection of 5.3nm/V at the end of the top electrode (measured value at x = 160µm), and equation (5.10) for the effective Young modulus, an effective transverse piezoelectric coefficient $e_{31,f}$ of -4.35C/m^2 is calculated. With equation (5.11), the transverse piezoelectric coefficient d_{31} equal -42.4pm/V. Figure 5.19 shows the experimental and calculated data of the deflection of the beam as a function of the position. The Meng, Mehregany, Deng model gives a lower value than the one of the Gardeniers model. But this model does not take the top electrode size into account. By adding this ratio of w_t/w_b of equation (5.8) into equation (5.14), an $e_{31,f}$ coefficient of -6.97C/m^2 is calculated. This value is in very good agreement with Gardenier’s model

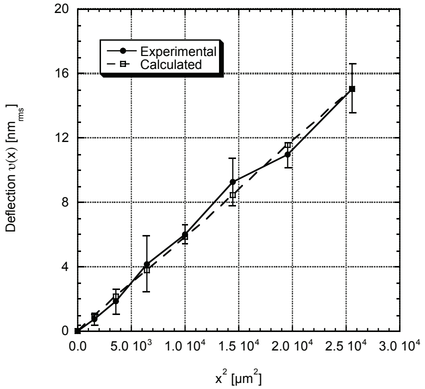

Figure 5.19: Experimental and calculated data of the beam deflection as a function of the position.

The experimental $e_{31,f}$ value of -6.50C/m^2 corresponds to the one calculated by the Gardeniers and the corrected Meng, Mehregany, Deng models. Table 5.4 summarizes the different values of $e_{31,f}$ and d_{31} from experimental and calculated results.

Table 5.4: Calculated and experimental values of $e_{31,f}$ and d_{31}.

		$e_{31,f}$ [C/m^2]	**d_{31} [pm/V]**
Gardeniers model	end point deflection	-6.54	-63.7
Corrected Meng, Mehregany, Deng model	fit to f(x^2) deflection	-6.97	-67.8
Experimental value (chapter 4)	on flat wafer	-6.50	-63.2

If comparing the two models (Gradeniers and Meng, Mehregany, Deng), it turns out that they are practically the same. The $\left(L_b L_t - \frac{L_t^2}{2}\right)$ term of equation (5.8) can be replaced by $\frac{x^2}{2}$ if $L_b = L_t$. By making this transformation, equation (5.8) becomes:

$$\delta(L) = -3\ e_{31,f}\ \frac{1}{\hat{E}_{Si} h_{Si}^2} \left(x^2\right) \frac{w_t}{w_b} V \tag{5.17}$$

With adding the w_t/w_b terms of equation (5.8) into equation (5.14), it becomes:

$$\upsilon(x) = \frac{3(\eta+1)}{(\xi\eta^3+4\eta^2+6\eta+4)\xi\eta+1} \cdot e_{31,f} \frac{1}{\hat{E}_{Si} h_{Si}^2} (x^2) \frac{w_t}{w_b} \Delta V \qquad (5.18)$$

By replacing η and ξ by the real values, the first term of equation (5.18) is equal to 2.78, which is nearly the same that the first term of equation (5.17).

These two models give the effective transverse coefficient $e_{31,f}$ of the PZT layer of the cantilever into the cavity and show that this coefficient is the same as the one measured by the cantilever bending method on PZT situated on top of the wafer (Figure 5.20).

Figure 5.20: Position of measured and calculated $e_{31,f}$ coefficient on top and bottom of the cavity of the AFM test structure cantilever respectively.

5.6 SUMMARY & OUTLOOKS

A test beam for an active AFM cantilever was successfully fabricated. The PZT layer was deposited on the reversed side onto the recessed part of the cantilever in order to avoid tip degradation during piezoelectric film preparation. All the different layers are deposited into deep cavities already prepared by NanoWorld AG. This required special measures with regard to photolithography. Firstly, the photoresist had to be spray coated. Secondly, the enlarged distance between mask and bottom of the cavity (>300µm) lead to aberration errors in the projection. The masks were corrected accordingly in order to obtain the desired dimensions in the developed resist. The PZT sputter deposition and the Cr/Au top electrode evaporation are achievable without any cracks, discontinuities, short or open circuits from top to bottom of the 300µm cavity.

A dielectric constant of 860 with a loss factor tan δ of 5.1% is measured on fully ferroelectric {100}-oriented PZT layer (texture index 92.7%). The resonance frequency of the test beam is measured at 679 ± 3% kHz. A value of 696 kHz is calculated using a bimorph model of the cantilever. The quality factor Q is 960 ± 9% and the coupling coefficient k is 5.7% with a standard deviation of 0.35 (6%).

An average 5.3nm/V deflection of the beam is measured by AFM techniques. This value is used to calculate the effective transverse piezoelectric coefficient $e_{31,f}$ and the transverse piezoelectric coefficient d_{31} with different models. Gardeniers model gives a good approximation of the $e_{31,f}$ coefficient ($-6.54C/m^2$). Corrected Meng, Mehregany, Deng model, explaining the effect of the beam position on the deflection, estimates the $e_{31,f}$ transverse coefficient at $-6.97C/m^2$. These two calculated values fit very well with the experimental value of the effective transverse piezoelectric coefficient measured by the cantilever bending method ($e_{31,f\,\mathrm{experimental}} = -6.50C/m^2$).

Unfortunately, no active AFM cantilever including tip fabrication could be realized. Although the PZT side was covered by a silicon nitride film, the wet etching for the tip fabrication removed the PZT film completely, questioning the protection strength of the nitride layer. In the following, the PZT sputter tool was inoperable, and there was no time to try a second time with improved nitride barrier and one side etching bath. The process was nevertheless developed to a promising level, and the prospects are good to complete the tip fabrication.

5.7 REFERENCES

1. G. Binnig, C.F. Quate and C. Gerber, *Atomic force microscope*, Phys. Rev. Lett., **56**(9), 930-933 (1986)

2. G. Binnig, H. Rohrer, C. Gerber and E. Weibel, *Surface studies by scanning tunneling microscopy*. Phys Rev Lett., **49**, 57-61 (1982)

3. T.R. Albrecht, P. Grütter, D. Horne and D. Rugar, *Frequency modulation detection using high-Q cantilevers for enhanced force microscope sensitivity*, J. Appl. Phys., **69**(2), 668-673 (1991)

4. G. Meyer and N.M. Amer, *Novel optical approach to atomic force microscopy,* Appl. Phys. Lett., **53**(12), 1045-1047 (1988)

5. S. Alexander, L. Hellemans, O. Marti, J. Schneir, V. Elings, P.K. Hansma, M. Longmiro and J. Gurley, *An atomic-resolution atomic-force microscope implemented using an optical lever*, J. Appl. Phys., **65**(1), 164-167 (1989)

6. C.A.J. Putman, B.G. De Grooth, N.F. Van Hulst and J. Greve, *A detailed analysis of the optical beam deflection technique for use in atomic force microscopy*, J. App. Phys., **72**(1), 6-12 (1992)

7. T. Itoh and T. Suga, *Development of a force sensor for atomic microscopy using piezoelectric thin films*, Nanotechnology, **4**, 218-224 (1993)

8. C. Lee, T. Itoh, R. Maeda and T. Suga, *Characterization of micromachined piezoelectric PZT force sensors for dynamic scanning force microscopy*, Rev. Sci. Instrum., **68**(5), 2091-2100 (1997)

9. C. Lee, T. Itoh and T Suga, *Self-excited piezoelectric PZT microcantilevers for dynamic SFM – with inherent sensing and actuating capabilities*, Sensors and Actuators, **A 72**, 179-188 (1999)

10. T. Fujii, S. Watanabe, M. Suzuki and T. Fujiu, *Application of lead zirconate titanate thin film displacement sensors for the atomic force microscope*, J. Vac. Technol., **B 13**(3), 1119-1122 (1995)

11. S. Watanabe and T Fujii, *Micro-fabricated piezoelectric cantilever for atomic force microscopy*, Rev. Sci. Instrum., **67**(11), 3898-3903 (1996)

12. Y. Miyahara, T. Fujii, S. Watanabe, A. Tonoli, S. Carabelli, H. Yamada and H. Bleuler, *Lead zirconate titanate cantilever for noncontact atomic force microscopy*, Appl. Surf. Sci., **140**, 428-431 (1999)

13. T. Shibata, K. Unno, E. Makino and S. Shimada, *Fabrication and characterization of diamond AFM probe integrated with PZT thin film sensor and actuator*, Sensors and Actuators A-Physical, **114**(2-3), 398-405 (2004)

14. Y. Miyahara, M. Deschler, T. Fujii, S. Watanabe and H. Bleuler, *Non-contact atomic force microscope a PZT cantilever used for detection sensing, direct oscillation and feedback actuation*, Appl. Surf. Sc., **188**(3-4), 450-455 (2002)

15. S. Hiboux, P. Muralt, and T. Maeder, *Domain and lattice contributions of dielectric and piezoelectric properties of thin films as a function of composition*, J. Mat. Res., **14**, 4307-4318 (1999)

16. T. Fujii and S. Watanabe, *Feedback positioning cantilever using lead zirconate titanate thin film for microscopy observation of micropattern*, Appl. Phys. Lett., **68**(4), 467-468 (1996)

17. N. Suehira, Y. Tomiyoshi, K. Sugiyama, S. Watanabe, T. Fujii, Y. Sugawara and S. Morita, *Development of low temperature ultrahigh vacuum noncontact atomic force microscope with PZT cantilever*, Applied Surface Science, **157**, 343-348 (2000)

18. S.C. Minne, S.R. Manalis and C.F. Quate, *Parallel atomic force microscopy using cantilevers with integrated piezoresistive sensors and integrated piezoelectric actuators*, Appl. Phys. Lett, **67**(26), 3918-3920 (1995)

19. P.-F. Indermühle, G. Schürmann G.-A. Racine and N.F. de Rooij, *Fabrication and characterization of cantilevers with integrated sharp tips and piezoelectric elements for actuation and detection for parallel AFM applications*, Sensors and Actuators, **A 60**, 186-190 (1997)

20. T. Itoh, C. Lee, J. Chu and T. Suga, *Piezoelectric force sensing* $Pb(Zr,Ti)O_3$ *microcantilever array for multiprobe scanning force microscopy*, Mat. Res. Soc. Symp. Proc., **444**, 59-67 (1997)

21. J.-A. Schweitz, *Mechanical characterization of thin films by micromechanical techniques*, MRS Bulletin, **17**(7) 34-45 (1992)

22. J.G.E. Gardeniers, A.G.B.J. Verholen, N.R. Tas and M. Elwenspoek, *Direct measurement of piezoelectric properties of sol-gel PZT films*, J. of the Korean Phys. Soc., **32**, S1573-1577 (1998)

23. J.G. Smits, W. Choi, *The constituent equation of piezoelectric heterogeneous bimorphs*, IEEE transactions on Ultrasonics, Ferroelectrics and frequency Controle., **38**(3), 256-270 (1991)

24. B. Jaffe, W.R. Cook and H. Jaffe, *Piezoelectric Ceramics*, London: Academic Press (1971)

25. Q. Meng, M. Mehregany and K. Deng, *Modeling of the electromechanical performance of piezoelectric laminated microactuators*, J. Micromech. Microeng., **3**, 18-23 (1993)

6

CONCLUSION & OUTLOOKS

The performance of piezoelectric MEMS is the result of the performance of the piezoelectric thin film material on the one hand, and the result of micromachining capabilities to realize optimal structures on the other hand. This work was devoted to the advancement in both fields. The studied piezoelectric material was Lead Zirconate Titanate $Pb(Zr_x, Ti_{1-x})O_3$. It was shown that by removing the compositional B-site gradient in sol-gel prepared films, the transverse piezoelectric coefficient increased by roughly 50%, reaching unprecedented high values. Moreover, the thickness limit for dense films could be pushed to 4 micrometers. In the field of micromachining, the new device structures with three-dimensional features were introduced. The key points are the use of the silicon wafer to fabricate molds or deep structures, and the use of in-situ sputtering allowing for acceptable thin film coverages on inclined surfaces. Backside coated cantilever beams and calotte-shaped free-standing membranes were demonstrate as electro-mechanical devices.

Sol-gel technique offers excellent control and reproducibility of process chemistry. Optimization of sol-gel PZT texturing was carried out by means of lead titanate ($PbTiO_3$) seed layer. The latter was prepared and deposited by CSD (Chemical Solution Deposition) technique on (111)-textured platinum bottom electrode and on full 100mm wafers. X-ray diffraction pattern showed the crystallization of $PbTiO_3$ occurring between 520 and 550°C. A significant increase in the PZT {100}-texture index of 15% was obtained by using as sol-gel deposited lead titanate seed layer prepared by an optimized annealing procedure. The use of a CSD seed layer gave full homogeneity of {100}-oriented PZT and simplified considerably the deposition procedure, as compared to the previously applied sputtered seed layer.

Study on the anneal conditions of PZT have been carried out in order to understand the changes involved during crystallization on the phase present and film texturing. By varying the crystallization temperature of 250nm PZT, it has been demonstrated that the PZT layer changes from amorphous film to pyrochlore and finally to highly {100}-oriented single-phase perovskite.

New PZT thin films of homogeneous composition were then synthesized by means of sol-gel route and deposited on sol-gel lead titanate seed layers. Compositional variations in sol-gel process films could be reduced from 40-70% Zr concentration to 50-55% Zr concentration. With standard solutions, different contrasts could be seen on TEM micrograph between 2 different annealed layers due to a change of the crystal symmetry, from tertagonal (Ti rich part) to rhombohedra (Zr rich part). In the gradient free film there was no such contrast change observed. The crystalline phase was much more homogeneous. As a consequence, lateral grain diameters were increasing by 50%. Thus, significant improvements of the properties were evaluated. The relative dielectric constant $\varepsilon_{33,f}$ was measured as 1620 and the remnant effective transverse piezoelectric coefficient $e_{31,f}$ was measured as $-17.7 C/m^2$. These improvements in properties are considered to be a direct consequence of a more homogeneous composition, hitting in a much larger volume fraction the optimal composition for the peaking properties at the morphotropic phase boundary. In addition, grain diameters increased, which should help to increase domain wall contributions to dielectric and piezoelectric properties. The $e_{31,f}$ value is excellent compared to previously published thin films values and comes close to the best available theoretical values of PZT 50/50. However, this result is still lower than optimized modern bulk PZT ceramics. Fatigue test and stress measurement should be made on these gradient free thin films. Further improvements would be the inclusion of dopants such as La^{3+} or Nb^{5+}. There is justified hope that in homogeneous films doping should become more effective than past experiences have shown in gradient films.

Reactive Multi-metallic targets sputtered PZT have been deposited on oblique surface to further three-dimensional piezoelectric MEMS structures fabrication. This deposition on non-flat surfaces has illustrated the diffusional growth mechanism of in-situ PZT sputtering at elevated temperature, i.e. at 570°C. At these conditions, the thermal surface diffusion mechanisms are predominant as compared to atom kinetics of impinging atoms and ion bombardment. Growth directions have been determined by

X-ray and TEM diffraction pattern and provided the same astonishing result. The grains have grown perpendicular to the substrate, even on surfaces parallel to the average sputtered flux, the crystallographic major planes staying parallel to the local surfaces. On vertical walls, a decrease in the zirconium content is measured, probably due to a higher Ti flux by backscattering.

The micromachining of materials is considered to be a key technology in MEMS fabrication. So far the surface micromachining technology by lithography has been successfully used for the fabrication of 2D microelectronic devices. 3D structure could be more useful for the performance of microsystem and could provide more flexibility on designing microsystems. Feasibility of 3D microstructures have been demonstrated by means of two piezoelectric micro-electro-mechanical devices.

First, a calotte shape piezoelectric membrane device consisting of platinum bottom electrode, PZT and platinum top electrode have been successfully developed and fabricated as demonstrator of novel three-dimensional micro-transducer. Calotte profile holes, prepared by wet etching performed into a silicon substrate, were used as micromould for the PZT membrane. Further film depositions (Pt bottom electrode, PZT and Pt top electrode) were achieved on the mold, and backside liberation of the membrane completed using deep anisotropic silicon etching by Bosch process. SEM micrograph showed a dense and homogeneous PZT layer without any crack or discontinuities. As different diameters of calotte were fabricated, the fundamental resonance frequencies varied between 2.5 and 16.5MHz and were found to be inversely proportional to the square of the base radius (same dependence as for flat clamp plates). The low frequency amplitude was measured by means of AFM and showed that the PZT layer is active with a responsivity of 3.5nm/V. Further improvement would require an optimization of the border region of the calotte. The use for medical imaging could be envisaged after obtaining higher coupling factors and solving packaging issues. This device could be interesting as ultrasonic transducer in micro-optic range to obtained focused pressure waves.

Secondly, a test structure piezoelectric PZT coated active AFM cantilever has been successfully fabricated. The PZT layer was deposited on patterned (111) platinum bottom electrode into deep cavities (>300µm) prepared by anisotropic wet etching. The photolithography was made possible by using a spray coating technique and taking into account for imaging aberration in the mask design. The study of the basic properties of such a structure has shown promising results as maximum deflection at the end of the beam up to 5.3nm/V. The major interest in the fabrication of such a structure was the use in top-performing AFM tips combining high resolution (curvature less than 10nm) and self-transduction for high-speed imaging, and tapping mode operation. Unfortunately the full fabrication of the tip could not be completed within the timeframe of this thesis. However, it is believed that all process problems are solved by now.

7

PUBLICATIONS & SYMPOSIA

1. F. Calame, J. Baborowski, N. Ledermann, P. Muralt, S. Gentil, and N. Setter, *Local growth of sol-gel films by means of micro-hotplates*, Integrated Ferroelectrics, **54**, 549-556 (2003)

2. F. Calame, P. Muralt, and S. Lutter, *PZT coated active AFM cantilever*, in Journée Couches Ferroélectriques, Besançon (2004)

3. F. Calame and P. Muralt, *Calotte PZT thin film structures for micromechanics*, in 2005 IEEE International Ultrasonics Symposium, Rotterdam, 1087-1090 (2005)

4. B. Belgacem, F. Calame, and P. Muralt, *Design, modeling and fabrication of piezoelectric micromachined ultrasonic transducers*, in 2005 IEEE International Ultrasonics Symposium, Rotterdam, 487-490 (2005)

5. B. Belgacem, F. Calame, and P. Muralt, *Thick PZT films for improvement of pMUT transducers performances*, in 5th Workshop on Micromachined Ultrasound Transducers, Munich (2006)

6. B. Belgacem, F. Calame, and P. Muralt, *Integration of PZT on SOI wafers: Increasing piezoelectric film thickness for providing a wide range of ultrasonic MEMS applications*, in MRS Fall Meeting, Boston (2006)

7. P. Muralt, B. Belgacem, and F. Calame, *Recent progress in piezoelectric Micro-machined Ultrasonic Transducers based on PZT films*, in 5th Workshop on Micromachined Ultrasound Transducers, Munich (2006)

8. N.P. Østbø, W.E. Booij, H. Reader, F. Tyholdt, E. Poppe, F. Calame, and P. Muralt, *MEMS-pie: the integration of piezo-electric thin films in a SOI-MEMS process*, mstnews, **4**(06), 40-42 (2006)

9. J.A.J. Steen, J. Hayakawa, T. Harada, K. Lee, F. Calame, G. Boero, A.J. Kulik, and J. Brugger, *Electrically conducting probes with full tungsten cantilever and tip for scanning probe applications*, Nanotechnology, **17**, 1464-1469 (2006)

10. B. Belgacem, F. Calame, and P. Muralt, *Thick sol-gel PZT film integrated in SOI-based, Micromachined Ultrasonic Transducers*, in IEEE SENSORS, Daegu, Korea (2006), *proceedings to be published*

11. B. Belgacem, F. Calame, and P. Muralt, *Thick PZT sol-gel films for pMUT transducers performances improvement*, in 2006 IEEE International Ultrasonic Symposium, Vancouver, 922-925 (2006)

12. K. Prume, P. Muralt, F. Calame, T. Schmitz-Kempen, and S. Tiedke, *Piezoelectric thin films: evaluation of electrical and electromechanical characteristics for MEMS devices*, IEEE Trans. UFFC, **54**(1), 8-14 (2007)

13. F. Calame and P. Muralt, *Growth and properties of gradient free sol-gel lead zirconate titanate thin films*, Appl. Phys. Lett., **90**, 062907 (2007)

14. B. Belgacem, F. Calame, and P. Muralt, *Piezoelectric micromachined ultrasonic transducers with thick PZT sol-gel films*, J. Electroceram., online (2007)

15. F. Calame and P. Muralt, *Novel 3D PZT thin film structures for micromechanics*, J. Electroceram., online (2007)

16. K. Prume, P. Muralt, F. Calame, T. Schmitz-Kempen, and S. Tiedke, *Extensive electromechanical characterization of PZT thin films for MEMS applications by electrical and mechanical excitation signals*, J. Electroceram., online (2007)

17. H. Raeder, F. Tyholdt, W. Booij, F. Calame, N.P. Østbø, R. Bredesen, G. Rijnders, and P. Muralt, *Taking piezoelectric microsystems from the laboratory to production*, J. Electroceram., online (2007)

18. F. Tyholdt, F. Calame, K. Prume, W. Booij, H. Ræder, and P. Muralt, *Chemically derived seeding layer for {100}-textured PZT thin films*, J. Electroceram., online (2007)

19. B. Belgacem, F. Calame, and P. Muralt, *Piezoelectric micromachined ultrasonic transducers based on PZT films*, in 15th IEEE ISAF 2006, Sunset Beach (2007 to be published)

20. K. Prume, P. Muralt, F. Calame, T. Schmitz-Kempen, and S. Tiedke, *Measurment of the transverse effective piezoelectric coefficient ($e_{31,f}$) of PZT thin films by applying homogeneous uniaxial stress*, in 15th IEEE ISAF 2006, Sunset Beach (2007 to be published)

CURRICULUM VITAE

Florian Calame
Born August 28th 1976
Swiss citizen
EPFL Engineer in Materials Science and Technology

2007	Research assistant at the Ceramics Laboratory of the Material Institute in The Ecole Polytechnique Fédérale de Lausanne (EPFL), Switzerland. PhD thesis on PZT thin film growth and chemical composition control on flat and novel three-dimensional micromachined structures for MEMS devices.
2002	Studies in material science in the EPFL, diploma thesis on local growth of sol-gel films by means of microhotplates. 3rd year (1999 – 2000) done in University of Manchester, Institute of Science and Technology (UMIST) in the Material Science Centre, Manchester, UK.
1996	High school at the Gymnase de la Cité in Lausanne, scientific section.